STRATEGIES FOR IMPROVING LUMINESCENCE PROPERTIES OF GLYCOTHERMALLY SYNTHESIZED CE:YAG NANOPHOSPHORS

STRATEGIES FOR IMPROVING LUMINESCENCE PROPERTIES OF GLYCOTHERMALLY SYNTHESIZED CE:YAG NANOPHOSPHORS

By

SAMUEL PETER, B.Sc.

A Thesis Submitted to the School of Graduate Studies in Partial Fulfillment of the Requirements for the Degree Doctor of Philosophy

McMaster University DOCTOR OF PHILOSOPHY (2021)

Hamilton, Ontario (Department of Engineering Physics)

TITLE: Strategies For Improving Luminescence Properties of Glycothermally Synthesized Ce:YAG Nanophosphors

AUTHOR: Samuel Peter, B.Sc. (McMaster University)

SUPERVISOR: Professor Adrian Kitai

NUMBER OF PAGES: x, 164

i. Abstract

Ce:YAG phosphors used in white LED backlit LCD displays suffer from two major issues: the phosphor powder is too large for next generation microLED display technology, and there is a lack of red in its emission spectrum. To address this, Ce:YAG based nanophosphors were synthesized using the glycothermal method. They were found to contain ~10x higher concentrations of octahedrally coordinated Al atoms compared to bulk Ce:YAG, confirmed by NMR spectroscopy. Photoluminescence and photostability were found to be enhanced with the growth of an intrinsic shell layer, made using a two-step growth process. Shell thickness was controlled by the addition of intrinsic precursor material as a ratio of the initial precursor concentration, denoted as the shell-to-seed ratio (SSR). The absorption spectra of Ce:YAG could be tuned up to 40 nm with the addition of Mg-Si pairs. An enhancement of Ce:YAG nanophosphor luminescence was seen when the reaction temperature was slightly elevated, attributed to increased precursor reactivity due to the higher kinetics of precursor ligand cleavage. The introduction of Mn^{2+} as a co-dopant was found to provide a red component to the Ce:YAG emission spectrum. XRD structural analysis indicated that Mn^{2+} should preferentially occupy the Y site, though the 594 nm emission characteristic of $^4T_1(^4G) \rightarrow {}^6A_1(^6S)$ transitions in octahedral co-ordination was observed. Mn^{2+} atoms which occupy Al octahedral sites are well supported for luminescence due to the high density of octahedral sites present after gycothermal synthesis. Mn^{2+} emission was enhanced using Si^{4+} as a charge compensator, and further enhanced with the addition of an intrinsic shell layer. Non-radiative energy transfer of Ce to Mn^{2+} was observed, indicating that the parity allowed $5d \rightarrow 4f$ transition of Ce acts as

an effective sensitizer for Mn^2 luminescence. Glycothermal synthesis was found to preserve the luminescent trivalent and divalent oxidation states of Ce and Mn, respectively.

ii. Acknowledgements

"If you wish to build a ship, do not divide the men into teams and send them to the forest to cut wood. Instead, teach them to long for the vast and endless sea."

- Antoine de Saint-Exupéry

There are many incredible people who I've had the immense privilege of sharing this journey with. Kindly bear with me while I attempt to thank them all! First, I would not be on this path of lifelong learning if not for the example set by my father Leonard, and would not have gotten nearly this far without my mother Vasanta and sister Jacinta showing me that it's always a better choice to be kind.

I am grateful to the Natural Sciences and Engineering Research Council of Canada (NSERC) for the funding to make this research possible. I'd also like to thank the talented and hardworking team at McMaster who were always willing to lend a helping hand. In particular, Victoria Jarvis and Jim Britten of the McMaster Analytical X-ray Diffraction (MAX) facility; Carmen Andrei and Chris Butcher of the Canadian Center for Electron Microscopy (CCEM); Elna Luckham, Marta Princz, and Zeynel Bayindir of the McMaster Biointerfaces Institute (BI); Bob Berno of the McMaster Nuclear Magnetic Resonance (NMR) facility; And my gal Doris Stevanovic of the Center for Emerging Device Technologies (CEDT) for keeping us all safe.

I feel particularly lucky to have been supported by my supervisory committee members Jonathan Bradley and Igor Zhitomirsky. Not only are they extremely

knowledgeable, but they were always generous with sharing that knowledge. I'd also like to thank my current and former group members for bearing with my ramblings in the group meetings, including Siwei Ma, Weiwei Zhao, Andrea Beauchamp, Salman Bawa, Liam Dow, Tingwei Zhang, and Dan Kuang.

I could not have made it here without the friends I made along the way. Your willingness to celebrate the little things always gave me something to look forward to. To all the past and present members of the Caffeineds, the Diamond Lattice softball team, and the Engineering Graduate Society, thank you. I'd also like to take a moment to thank my wonderful partner Paige Wilson, the even to my odd, with whom there is no parity.

And last, but by no means least, I'd like to give thanks for my supervisor Dr. Adrian Kitai, for showing me how to build a ship.

iii. Table of Contents

iv. Table of Figures

v. Table of Tables

vi. List of Abbreviations

ATR	Attenuated total reflectance
CP	Cross polarized
EDS	Energy dispersive spectroscopy
EELS	Electron energy loss spectroscopy
FTIR	Fourier transform infrared spectroscopy
MAS	Magic angle spinning
NMR	Nuclear magnetic resonance
PL	Photoluminescence
PLE	Photoluminescence excitation
PLQY	Photoluminescence quantum yield
SPE	Single pulse excitation
SSR	Shell-to-seed ratio
TEM	Transmission electron microscopy
TGA	Thermogravimetric analysis
XPS	X-ray photoelectron spectroscopy
XRD	X-ray diffraction

Chapter 1: Introduction

1.1. Overview of Ce:YAG

As a fully synthetic material, yttrium aluminum garnet ($Y_3Al_5O_{12}$), better known as YAG, exists as quiet evidence of humankind's triumph over a small facet of the natural order. The body-centered cubic YAG crystal structure takes the Ia3d space group, and is made up of a network of Y atoms in dodecahedral (8-fold) coordination and Al atoms in either tetrahedral (4-fold) or octahedral (6-fold) coordination, with a $^{IV}Al/^{VI}Al$ ratio of 3/2 in single crystal YAG, shown in Figure 1.1.[1-5] As a robust refractory ceramic, YAG is highly stable chemically, thermally, and mechanically. However, the usefulness of YAG comes from its functionality as a host for luminescent ions, namely rare earths and transition metals. The large Y site can accommodate luminescent rare earth ions, such as Nd, used most commonly in Nd:YAG lasers at 1064 nm or frequency doubled 532 nm green lasers.[6-9] Yb is also a common dopant, with Yb:YAG lasers capable of operating at 1030 nm and lasing at high power.[10,11] Not to be outdone, the octahedral Al site can also accommodate luminescent transition metal ions, such as Cr^{3+}, Cr^{4+}, Mn^{2+}, Mn^{3+}, and Mn^{4+}.[12-16] However, the main focus of this research involves the rare earth Ce as the dopant of interest in the Y site.

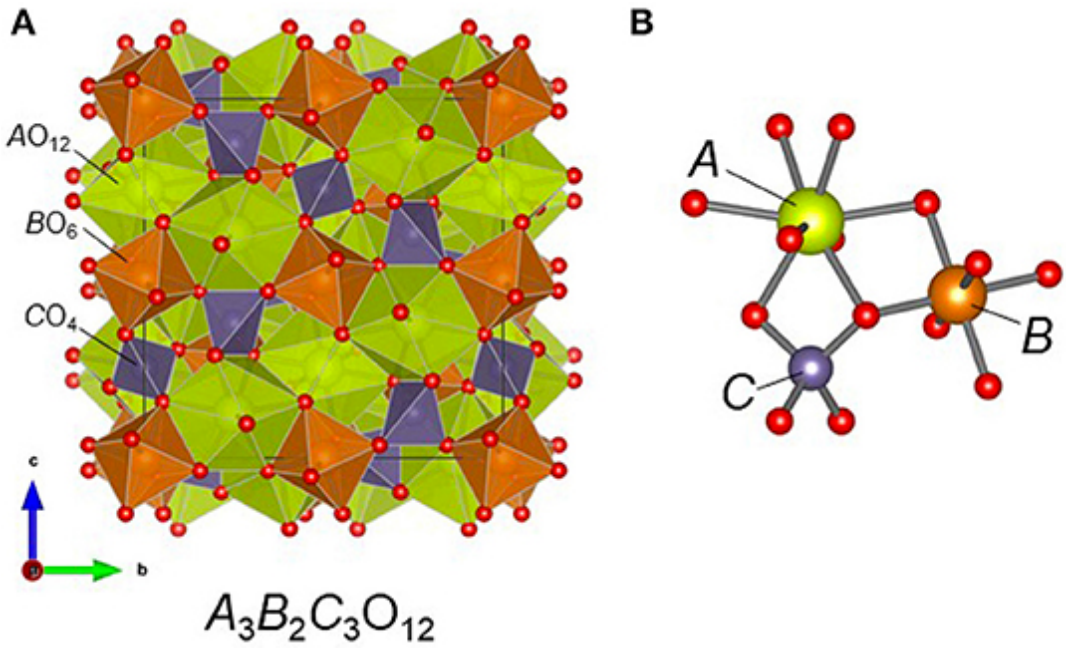

Figure 1.1: The garnet crystal structure.
In Ce:YAG, Ce and Y occupy the A site, and Al occupies both the B and C sites. Figure taken from [1] without changes and licensed under Creative Commons BY 4.0.

It's hard to overstate the impact that Ce:YAG has had on the modern world. Ce:YAG has been called on time after time to provide white lighting solutions through several generations of lighting technologies. When excited by blue light or high energy electrons, Ce:YAG emits a broad yellow-green. As such, it was used in lighting and display technologies such as cathode ray televisions, mercury vapor fluorescent lighting, and most recently, paired with blue light emitting diodes (LEDs) to produce white LEDs.[17-24] It was this last innovation that significantly changed the lighting industry. The combination of a blue LED with Ce:YAG made it possible to produce smaller, brighter, and more temperature insensitive white lighting sources operating on only a few volts. This allowed

for display technologies, such as liquid crystal displays (LCDs), to grow in size at a lower cost, higher brightness, and with higher energy efficiency. However, in recent years, newer display technologies have begun to see an emergence in consumer electronics such as organic LEDs (OLEDs) and microLEDs, in which independent red, green, and blue LEDs are used as subpixels to produce the desired image. These technologies produce outstanding contrast ratios and good image quality, although OLEDs still suffer from degradation issues such as image burn in, and the use of three LEDs per pixel in the case of microLEDs triples the cost and complexity of assembly.[25-27] So far, Ce:YAG has been unable to fill the need of current display solutions due to two main drawbacks: the current method for producing the phosphor yields powders ~10 μm in size, too large for next generation fine pitch display technologies; and the resulting emission spectrum has a notable lack of red in its emission, which is perceived as a 'cold' white light.

The first of these challenges can be addressed by reducing the size of the phosphor. Commercially available Ce:YAG is produced using the solid state method, in which raw oxides are mechanically ground and fired at temperatures in excess of 1400 ºC.[28.29] These conditions are required to produce a phase pure YAG, although at these temperatures, sintering and grain growth is unavoidable. It is therefore required to fundamentally alter the reaction conditions in order to demonstrate control over size and morphology of Ce:YAG phosphor powders. Several techniques have been developed in recent years to produce Ce:YAG that is nanosized, such as the hydrothermal and solvothermal method.[30-35]

Since wet chemical methods take place in solution, it is possible to exert much more control over particle size and morphology.[34-38] These techniques involve reacting precursor materials in a sealed vessel at temperatures much lower than the solid state method and at relatively high pressure to crystallize YAG directly from solution, producing phase-pure, monodispersed YAG 50-100 nm in size. One such wet chemical method is the glycothermal method, which specifically uses glycol solvents, and has been developed in recent years. The glycothermal method has been shown to produce high quality nanophosphors at lower temperatures and pressures than the hydrothermal method.[39-41] The nanophosphors used in this body of research were synthesized using the glycothermal method. It is also important to note that YAG synthesized using the gylcothermal method has been shown to exhibit $^{IV}Al/^{VI}Al$ ratios of ~0.15, roughly 10x lower than that of bulk YAG at 3/2.[42]

The second issue holding Ce:YAG back from once again being regarded as the material of choice for next generation lighting solutions is the notable lack of a red component in the emission spectrum. The optical properties of Ce are highly dependent on the strength of the electric field imposed by the host crystal, which is known as the crystal or ligand field. The details of this will be discussed in Chapter 2. This presents an opportunity to modify the optical properties of Ce:YAG, such as the absorption and emission spectra, by modifying the strength of the local crystal field.

1.2. Thesis Objectives

There is currently a gap in the display technology market for a robust nanophosphor material which can be manufactured at a size small enough to keep pace with technological and industry advancements. It is the aim of this thesis to present an evidence-based case that Ce:YAG nanophosphors synthesized using the glycothermal method can fill this need. This body of work aims to demonstrate experimental conditions which can produce nanosized Ce:YAG, as well as improve its overall luminescence output and colour quality using engineering physics and materials science knowledge. As a relatively new method for the synthesis of nanoscale mixed oxides, key findings of the glycothermal method and precursor reaction kinetics will be discussed as well.

The main focus of this research has been the local crystal field of Ce in the nanocrystal. The crystal field is the primary driver of visible luminescence from Ce, and as such, it is imperative that care is taken to ensure that it is optimized. This becomes especially important on the nanoscale, where the surface area, and therefore potential for surface defects, is much higher than in bulk YAG. In this thesis, the proposed method for improving the crystal field of nanosized Ce:YAG involves using a doped/intrinsic core/shell approach, in which an intrinsic YAG layer is grown on previously synthesized Ce:YAG nanoparticles in a two-step, seed-mediated growth technique. Moreover, as the dominant factor of the optical properties of Ce, the crystal field can be modified to tailor the luminescence characteristics of Ce:YAG nanophosphors.[43-46] This thesis aims to make use of the octahedral Al sites, which are in abundance using the glycothermal method, to tune the optical properties of Ce:YAG nanophosphors. Finally, both of these strategies are

combined in order to provide a red component to the emission spectrum by means of non-radiative energy transfer from Ce to a secondary luminescent ion, Mn^{2+}, which occupies octahedral coordination and whose luminescence can also be enhanced by improving the local crystal field.

A variety of structural, optical, and microscopy experiments were undertaken in order to verify these claims. These included XRD, NMR, TEM, EELS, EDS, XPS, FTIR, TGA, PL/PLE, and fluorescence lifetime tests. A brief summary of these techniques is provided in Chapter 5 to outline why they were useful for characterization of the nanophosphors, but also in the hopes that the reader can make use of them for their own research purposes.

This thesis presents a collection of proposed experimental techniques and results for the synthesis of a set of nanophosphors and extensive characterization of these materials. This work is guided by reported literature as well as well as ideas grounded in theory to produce nanoscale Ce:YAG phosphors with improved optical properties as a candidate material for next-generation display and lighting solutions. However, this thesis stops short of device fabrication. The steps required in order to take the dried powders formed after synthesis and prepare a device, including forming stable colloidal suspensions in a solvent compatible with the surface chemistry of the substrate, finding an appropriate deposition method which can control the phosphor layer thickness without resulting in particle agglomeration after drying, as well as characterization of the device, is enough to warrant a separate graduate thesis. The decision was therefore made to limit the scope of

this research to the preparation and characterization of Ce:YAG nanophosphors, as well as to focus on finding experimental conditions to optimize their performance.

1.3. Contributions to the Field

The field of research involving the glycothermal method is fairly narrow, with those using it to synthesize Ce:YAG nanophosphors slimmer still. However, there is renewed interest, as it is able to provide a high degree of control over important factors such as particle size, morphology, and dispersion. The contributions of this research are of value to the community, as they address factors such as the ability to engineer an improved crystal field at the particle surface by using a doped/intrinsic core/shell approach. In addition, the study of precursor reaction kinetics provides valuable insight into the glycothermal method, as it was found that the precursors were more likely to participate in the reaction more uniformly at a slightly higher temperature than the current standard synthesis route. A study was also conducted in which the surface of the as-prepared nanophosphors was stripped of residual organics, with new molecules grafted on post-synthesis, with the intention of providing a blueprint for the research community to be able to modify the YAG surface for applications in other solvents, epoxies, binders, etc. Finally, the work involving the co-dopant Mn^{2+} should be of keen interest to the nanophosphor community. It was found that while there is an abundance of octahedral Al sites when using the glycothermal method, which is the preferred coordination of Mn^{2+} in other synthesis methods, the Mn^{2+} precursor preferentially occupies the larger Y site.[15] However, Mn^{2+} which does occupy

octahedral Al sites is well supported for luminescence due to the abundance of these defects, and Mn^{2+} luminescence was observed.

The period of study produced four first author publications, the last of which is currently in press. In addition, two non-first author publications were also credited due to contribution involving microscopy and XRD characterizations. The publications are as follows:

- **Peter, S.**, Kuyanov, P., Goktas, N. I., LaPierre, R., & Kitai, A. (2018). Microstructure development and photoluminescence of annealed nanosized Ce: YAG/Al_2O_3 and Ce: YAG/Cr: Al_2O_3 powder composites. *Materials Research Express*, *5*(3), 036207. DOI: https://doi.org/10.1088/2053-1591/aab3fc
- **Peter, S.**, Patel, A., & Kitai, A. (2019). Photoluminescence enhancement of Ce: YAG nanophosphors via doped/intrinsic core/shell structures. *Journal of Luminescence*, *211*, 82-87. DOI: https://doi.org/10.1016/j.jlumin.2019.03.024
- Ma, S., **Peter, S.**, & Kitai, A. H. (2020). CuO Nanowire-Enhanced Alternating Current-Driven Powder Electroluminescent Device with High Performance. *ACS Applied Electronic Materials*, *2*(7), 1855-1860. DOI: https://doi.org/10.1021/acsaelm.0c00343
- Bawa, S., Zhang, T., Dow, L., **Peter, S.**, & Kitai, A. H. (2021). Porous SiC electroluminescence from p–i–n junction and a lateral carrier diffusion model. *Journal of Applied Physics*, *129*(4), 044501. DOI: https://doi.org/10.1063/5.0033243

- **Peter, S.**, Fitzpatrick, M., & Kitai, A. (2021). Glycothermal synthesis and photoluminescence of Mg–Si modified Ce: YAG nanophosphors. *Nanoscale Advances*, *3*(10), 2911-2917. DOI: 10.1039/D1NA00060H
- **Peter, S.**, Richards, M., Fang, Q., & Kitai, A. (2021). Enhanced red emission of glycothermally synthesized Ce:YAG nanophosphors via Mn^{2+} addition. *Materials Chemistry and Physics*. Advance online publication. DOI: https://doi.org/10.1016/j.matchemphys.2021.125497

Chapter 2: Luminescence of Rare Earth and Transition Metals in the YAG Host

2.1. Overview of Absorption and Emission of Light By Impurity Atoms

As mentioned previously, the luminescence of Ce is derived from the electric field imposed by the surrounding environment. It is therefore helpful to present a general overview of how the generation of light is achieved by impurity atoms in crystalline solids, such that an understanding about how and why the research avenues were pursued can be reached. This chapter covers the absorption and emission of light by impurity atoms, as well as luminescence centers of transition metals and rare earths. For a more detailed overview of luminescence outside of this scope, for example that of electroluminescence, cathodoluminescence, or luminescence of organic molecules, the reader is referred elsewhere.[46]

There are three processes involved in the production of light: absorption, spontaneous emission, and stimulated emission, as outlined in Figure 2.1.[47] Absorption involves the interaction of a photon with sufficient energy and an electron, promoting the electron to a higher energy level E_2. Such a photon is described as:

$$E_{photon} = E_2 - E_1 = \hbar\omega_{12} \tag{2.1}$$

where $\hbar$ is the reduced Plank's constant and ω_{12} is the angular frequency of the photon ($\omega_{12} = 2\pi\nu_{12}$). Spontaneous emission is this process in the reverse, involving the relaxation of an electron at a higher energy state to the ground state E_1 resulting in the

emission of a photon with energy E_{photon}. Stimulated emission requires an electron at a higher energy state and a photon with energy E_{photon}. This photon then induces the relaxation of the electron, resulting in a second photon with energy E_{photon}.

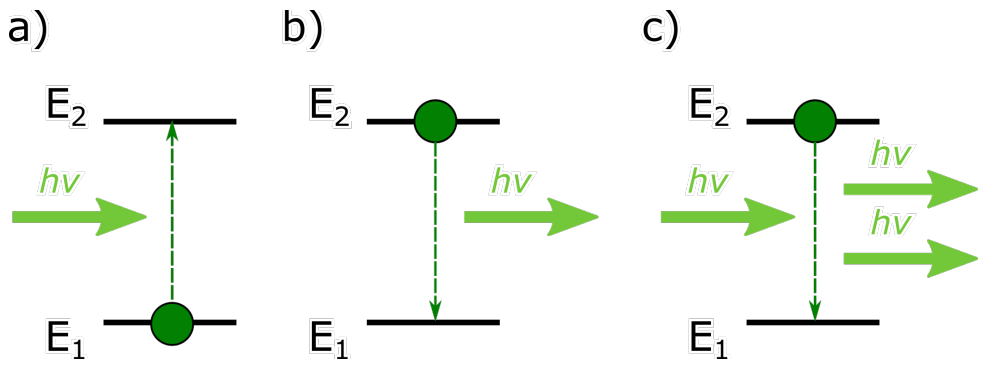

Figure 2.1: Optical absorption and emission processes.

a) Photon absorption. b) Spontaneous emission. c) Stimulated emission.

The process of absorption and emission of light by an atom can be thought of as a harmonic dipole oscillator, with a bound electron oscillating about a fixed positive point charge at z=0 with frequency ω_0. In this case, the dipole moment can be expressed as:

$$M = ez = M_0 \exp(i\omega_0 t) \tag{2.2}$$

However, the two states E_1 and E_2 are discrete, and as such, the transition between them must be treated quantum mechanically. As such, this dipole moment can be described as:

$$M_{12} = \int \psi_2^*(er)\psi_1 d^3r \tag{2.3}$$

where M_{12} is the electric dipole moment, ψ_1 and ψ_2 are the wavefunctions of the ground and excited state, respectively, and r is the position of the electron. In order for an absorption event to occur, it follows that there must be an electron present in the ground state, a state available at the higher energy level, and a photon of energy E_{photon}. The opposite is true for the case of stimulated emission, and in the case of spontaneous emission, only an electron at the higher energy level and an available state at the ground state are required. Together, these conditions represent the probability of a transition to occur, and can be described by the Einstein coefficients of absorption and emission. The following equations represent the transition probabilities of absorption, stimulated emission, and spontaneous emission, respectively:

$$\left(\frac{dn_1}{dt}\right) = -B_{12} n_1 \rho(\nu) \tag{2.4}$$

$$\left(\frac{dn_1}{dt}\right) = B_{21} n_2 \rho(\nu) \tag{2.5}$$

$$\left(\frac{dn_1}{dt}\right) = A_{21} n_2 \tag{2.6}$$

where n_1 and n_2 is the number of atoms in the ground and excited state, respectively, B_{12} is the transition probability or Einstein coefficient for absorption, B_{21} is the transition probability for stimulated emission, A_{21} is the transition probability for spontaneous emission, and $\rho(\nu)$ is the energy density of the radiation field at frequency ν. At

thermodynamic equilibrium, there is no net change in the number of electrons in an excited state, and these processes are balanced, represented in Equation 2.7:

$$A_{21}n_2 + B_{21}n_2\rho(\nu) - B_{12}n_1\rho(\nu) = 0$$

(2.7)

While the previous equations describe the transitions required to produce a photon, not all transitions are radiative. The strength of oscillation of the optical center can be described as:

$$f_{12} = \frac{2m_e\omega_{12}}{3\hbar e^2}|M_{12}|^2$$

(2.8)

where f_{12} is the oscillator strength, expressed as a dimensionless quantity, m_e is the mass of an electron, and e is the charge of an electron. One can see that the strength of oscillation depends on the dipole moment of the oscillator, expressed in Equation 2.3. However, if the dipole oscillator integrates to zero, no oscillation is possible, and the transition is considered to be forbidden. The position operator r is said to have odd parity, in that its value becomes negative when undergoing a spatial inversion. The integral of an odd function is zero, and as such, the parity of ψ_1 and ψ_2 must be of opposite parity to produce a non-zero dipole moment and therefore an allowed transition.

In order for the wavefunctions of the ground and excited states to have opposite parity, it is worth looking at how these energy levels are described. Electronic energy states are described using their set of quantum numbers, with S, L, and J denoting their spin, orbital, and total angular momentum quantum numbers, respectively, with ΔS representing

the difference in S between the ground and excited state, for example. The selection rules for allowed transitions are described as:

$$\Delta S = 0$$

$$\Delta L = 0 \; or \; \pm 1$$

$$\Delta J = 0 \; or \pm 1, \qquad (J = 0 \nleftrightarrow 0 \; not \; allowed)$$

Some transitions are considered forbidden when the atom is isolated in a vacuum, however when placed into a crystalline host, the imposed interaction with the electrons in the system can shift the electronic configuration enough for the selection rules to be satisfied, allowing for radiative transitions to occur. These are referred to as partially forbidden transitions, and will be discussed later in this chapter.

2.2. Transition Metal Luminescence in YAG

Transition metals are classified as having partially filled *d* orbitals, and each element can often take on several different valence states. The transition metals which exhibit luminescence typically make use of the 3*d* energy level, with either 3, 4, or 5 electrons occupying the outermost 3*d* orbital of the ion. Luminescence of transition metals involve intra-orbital transitions – that is, they occur from one 3*d* energy state to another 3*d* energy state. As discussed above, this transition involves no change in parity of the initial and final wavefunctions, and are therefore considered to be forbidden. This is the case if the transition metal exists as a free ion in gaseous form, where there is negligible interaction with neighbouring atoms. However, when these ions are incorporated into a liquid or solid

medium, the interaction of neighbouring electrons can alter the local electronic configuration enough to make these transitions possible.

2.2.1. Crystal Field Theory

The simplest case of the described phenomenon occurs in the $3d^1$ configuration, in which only one electron occupies the *d* orbital, which is the case for Ti^{3+}. As a free ion, all five 3*d* sub-orbitals have the same energy, and are said to be degenerate. However, when placed in the electric field of a crystalline solid, contributions from neighbouring atoms will affect the energies of the 3*d* sub-orbitals due to their spatial distributions. The most common case for transition metals involves the central cation surrounded by six anions at a distance R in coordinates of x, y, and z, arranged in an octahedral configuration as shown in Figure 2.2. The electrostatic potential V experienced by the central 3*d* electron at position r can be taken as:

$$V = \sum_{\mathrm{i}}^{\mathrm{i=6}} \frac{Ze^2}{|R_i - r|}$$

(2.9)

Where Z is the valency of the surrounding anion, e is the charge of an electron, R_i is the position of the i^{th} anion, and r is the position of the central 3*d* electron.

When $R_i >> r$, this potential function can be expressed by expansion on r to the fourth order:

$$V = \frac{6Ze^2}{R} + \frac{35Ze^2}{4R^5}(x^4 + y^4 + z^4 - \frac{3}{5}r^4)$$

(2.10)

The resulting effect of the potential V on the energy of the 3d orbitals is then:

$$\int \psi(3d) V \psi(3d) d^3r = \langle 3d|V|3d\rangle$$

(2.11)

The first term in the expression for the potential V is independent of r, and therefore affects the energy of each sub-orbital equally. This is generally not useful for spectroscopic applications where differences between energy states are of interest, and as such, the first term is generally neglected. The five sub-orbitals are sometimes given the labels $\zeta, \eta, \varsigma, u$, and v. Using the second term of Equation 2.10, the sub-orbital energies are found to be:

$$\langle \zeta|V|\zeta\rangle = \langle \eta|V|\eta\rangle = \langle \varsigma|V|\varsigma\rangle = -4Dq$$

(2.12)

$$\langle u|V|u\rangle = \langle v|V|v\rangle = 6Dq$$

(2.13)

Where:

$$D = \frac{35Ze}{4R^5}$$

And:

$$q = \frac{2e}{105}\int |R_{3d}(r)|^2 r^4 dr$$

This is all to say that when the sub-orbitals in the 3d shell are placed in an octahedral anion configuration, the probability density of the u and v electron orbitals, together referred to as the *e* orbitals, are highest along the bonding direction to neighbouring anions. The induced electrostatic repulsion puts the *e* orbitals at a higher energy level compared to a free 3d ion. Similarly, the probability density of ζ, η, and ς sub-orbitals, referred to as the

t_2 orbitals, are highest between the surrounding anions, resulting in a smaller electrostatic repulsion and therefore a lower energy level. The difference between the t_2 and e energy levels is then $10Dq$, the crystal field strength, sometimes referred to as Δ, and the electric potential imposed by the surrounding anions is said to have split the degeneracy of the five $3d$ orbitals. It is this splitting of the energy levels that can be observed spectroscopically.

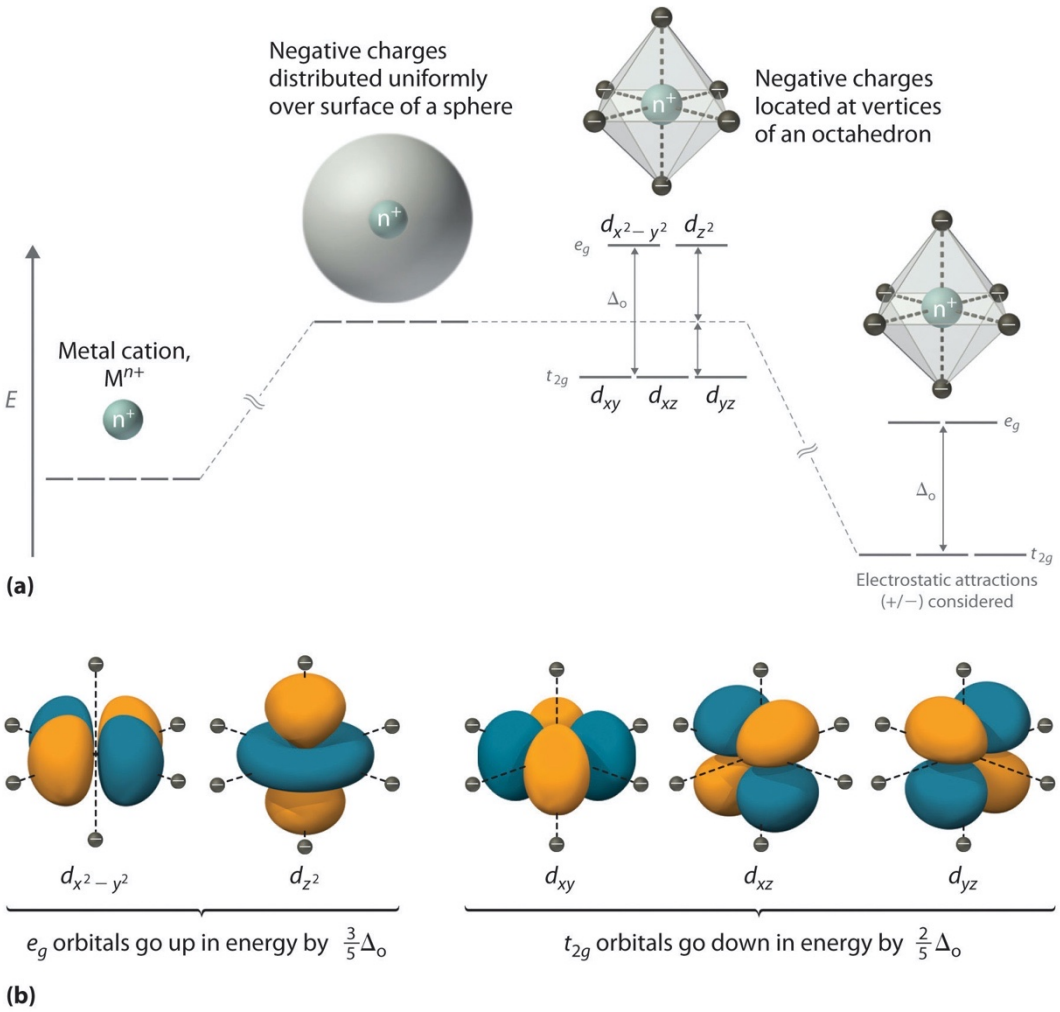

Figure 2.2: Schematic of crystal field splitting in transition metals.

a) Splitting of d orbitals by an octahedrally oriented anion field imposed on the central ion. b) Spatial distribution of transition metal d orbitals. Figure taken from [48] without changes and licensed under Creative Commons BY-NC-SA 3.0 US.

In cases when there is more than one electron occupying the 3*d* orbital, each electron is affected electrostatically by a potential of:

$$\sum_{i,j} e^2/r_{ij}$$

where r_{ij} is the distance between the i[th] and j[th] electron. The contributions of the additional electrons can be thought of as a small perturbation on the system, and as such, there is a further splitting of energy the t_2 and e sub-orbital energies. This is consistent with the Pauli exclusion principle, which states that no two electrons can share a quantum state. The notation of these mixed energy levels represent the possible symmetries of various anion point groups. As an example, in the case of two electrons occupying the 3d orbital (d^2) as is the case with V^{3+}, the following energy levels are possible:

$$t_2^2 \rightarrow {}^3T_1,\ {}^1A_1,\ {}^1E,\ {}^1T_2$$

$$t_2 e \rightarrow {}^3T_1,\ {}^3T_2,\ {}^1T_1,\ {}^1T_2$$

$$e^2 \rightarrow {}^3A_2,\ {}^1A_1,\ {}^1E$$

2.2.2. Tenabe-Sugano Diagrams

In 1954, Yukito Tanabe and Satoru Sugano published their paper 'On the absorption spectra of complex ions', depicting the electronic configurations of multiple electron systems of 3d transition metals from 2 to 8 electrons (d^2 *to* d^8) in an octahedral crystal field as a function of crystal field strength.[49] These visual representations became known as Tenabe-Sugano diagrams, and are extremely useful for determining spectroscopic trends of luminescent transition metal ions subjected to various crystal fields of host materials. The energy, given in cm^{-1}, and crystal field strength Dq are scaled by the electron repulsion present in the 3d atom, known as B or the Racah parameter. Electronic transitions of 3d transition metals are summarized in Figure 2.3. As an example, the energy of the ${}^2E \rightarrow {}^4A_2$ transition of d^3 ions such as Cr^{3+} and Mn^{4+} do not change appreciably over a wide range of crystal field strengths, and as such, they exhibit similar optical properties

in a variety of hosts. On the other hand, the slope of the $^4T_1 \rightarrow {}^6A_1$ transition of d^5 transition metal ions such as Mn^{2+} indicates a stronger dependence of the optical properties on the local crystal field.

a) d^2

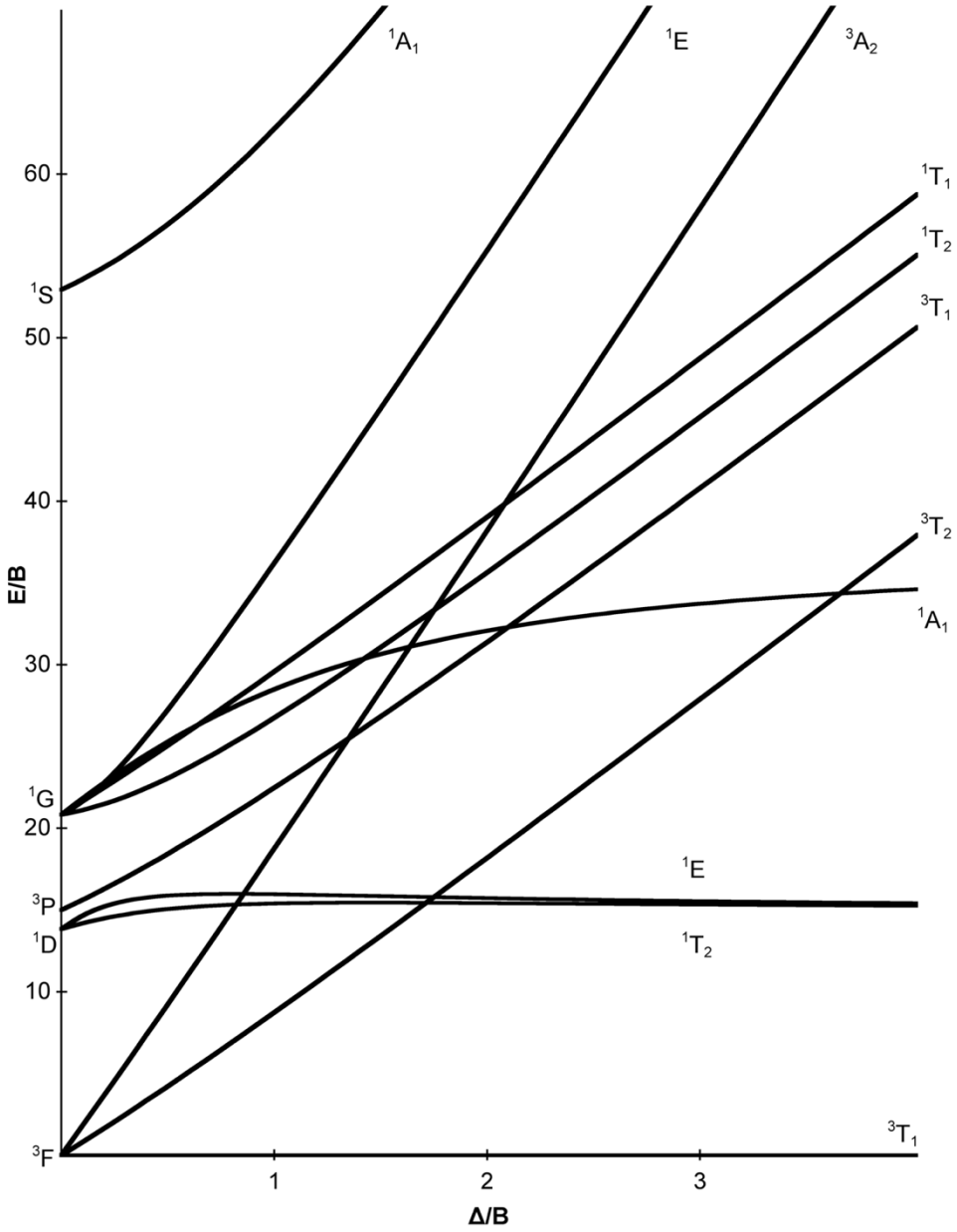

b) d^3

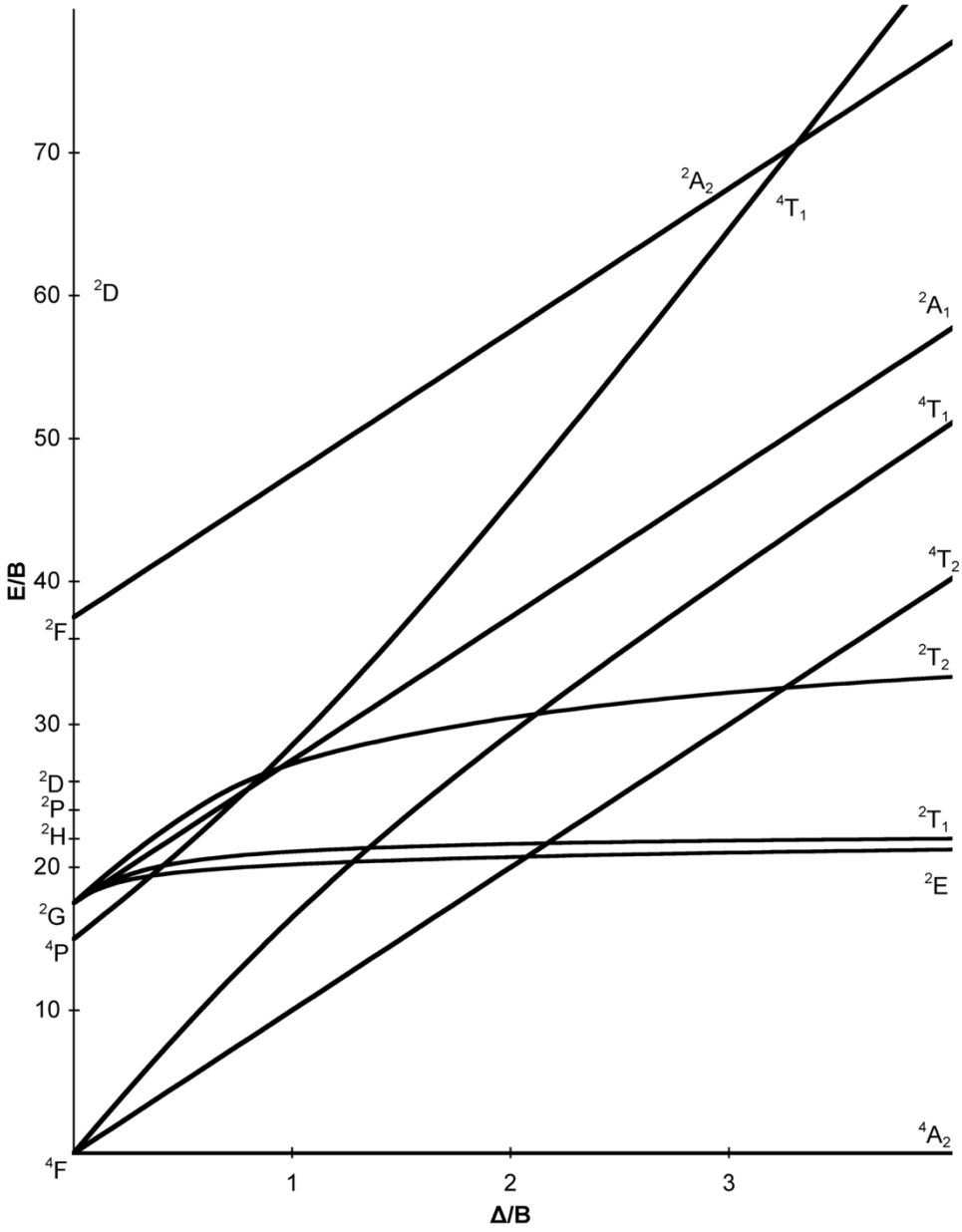
70
60
50
40
30
20
10
E/B
^{2}D
^{2}F
^{2}D
^{2}P
^{2}H
^{2}G
^{4}P
^{4}F
1
2
3
Δ/B
^{2}A$_2$
^{4}T$_1$
^{2}A$_1$
^{4}T$_1$
^{4}T$_2$
^{2}T$_2$
^{2}T$_1$
^{2}E
^{4}A$_2$

c) d^4

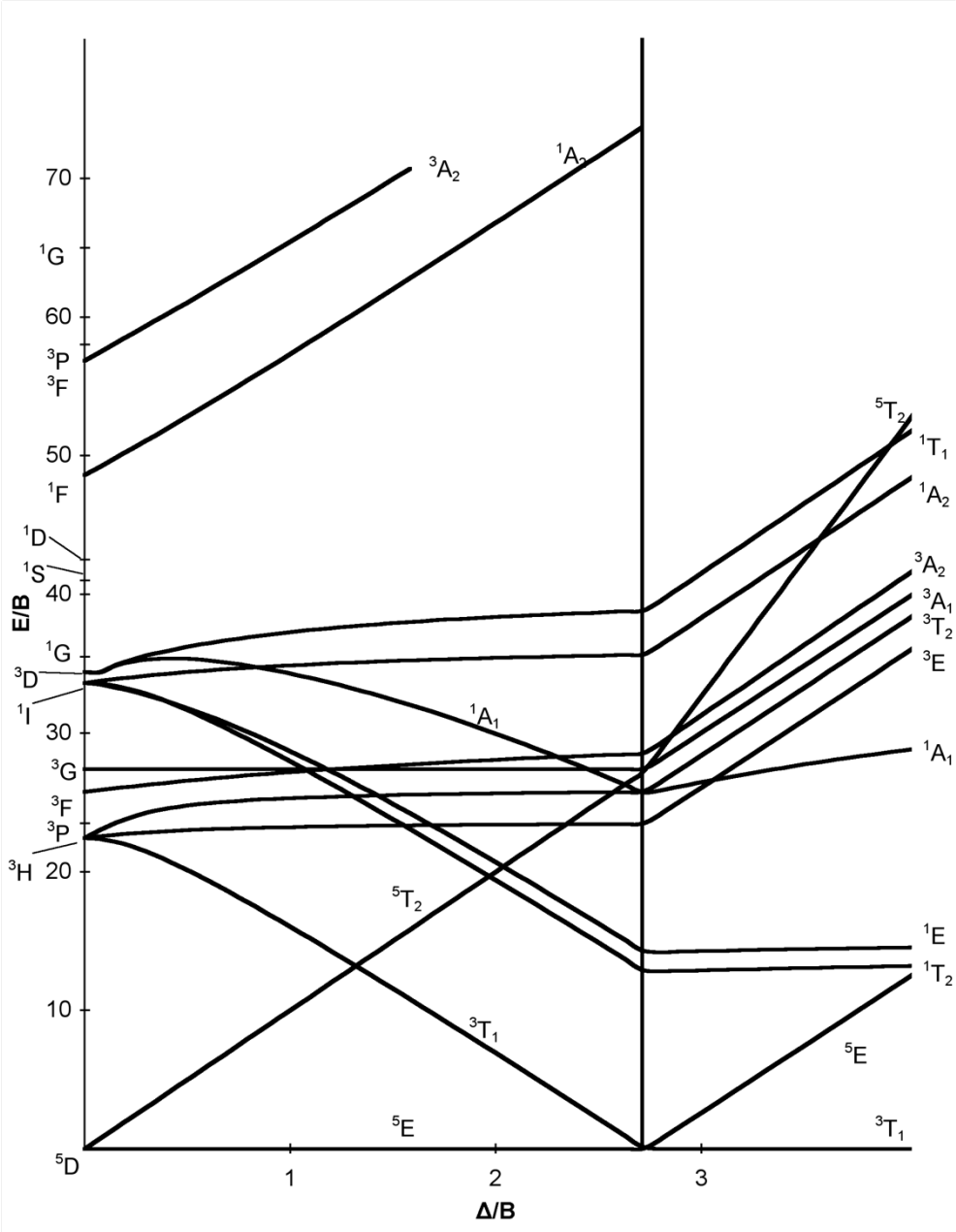
E/B
Δ/B
70
60
50
40
30
20
10
1
2
3
^1G
^3P
^3F
^1F
^1D
^1S
^3D
^1I
^3G
^3H
^5D
$^3A_2$
$^1A_2$
$^5T_2$
$^1T_1$
$^3A_1$
$^3T_2$
^3E
$^1A_1$
^1E
$^3T_1$
^5E

d) d^5

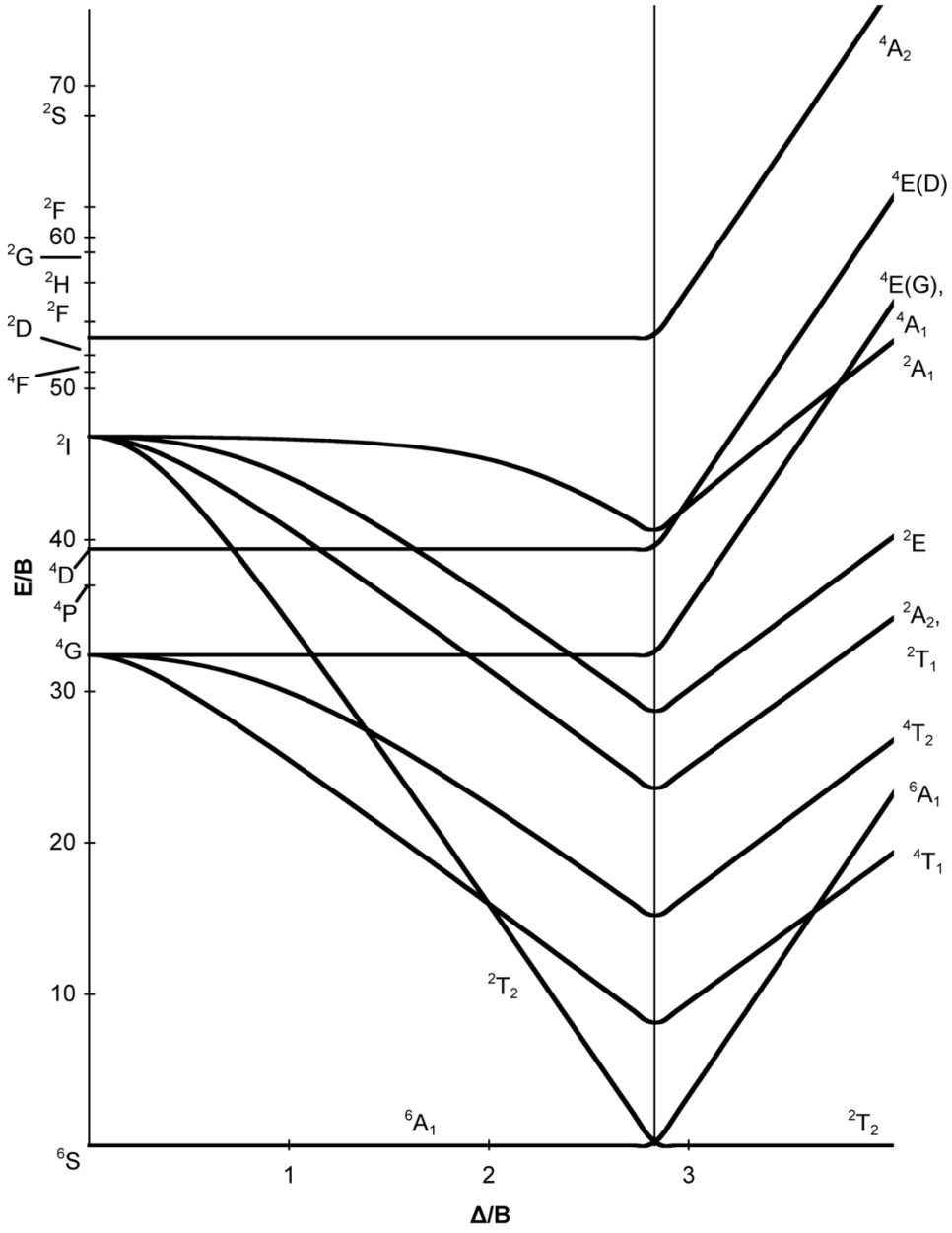
70
2S
2F
60
2G
2H
2F
2D
4F
50
2I
40
4D
4P
4G
30
20
10
6S
E/B
1
2
3
Δ/B
4A2
4E(D)
4E(G),
4A1
2A1
2E
2A2,
2T1
4T2
6A1
4T1
2T2
6A1
2T2

e) d^6

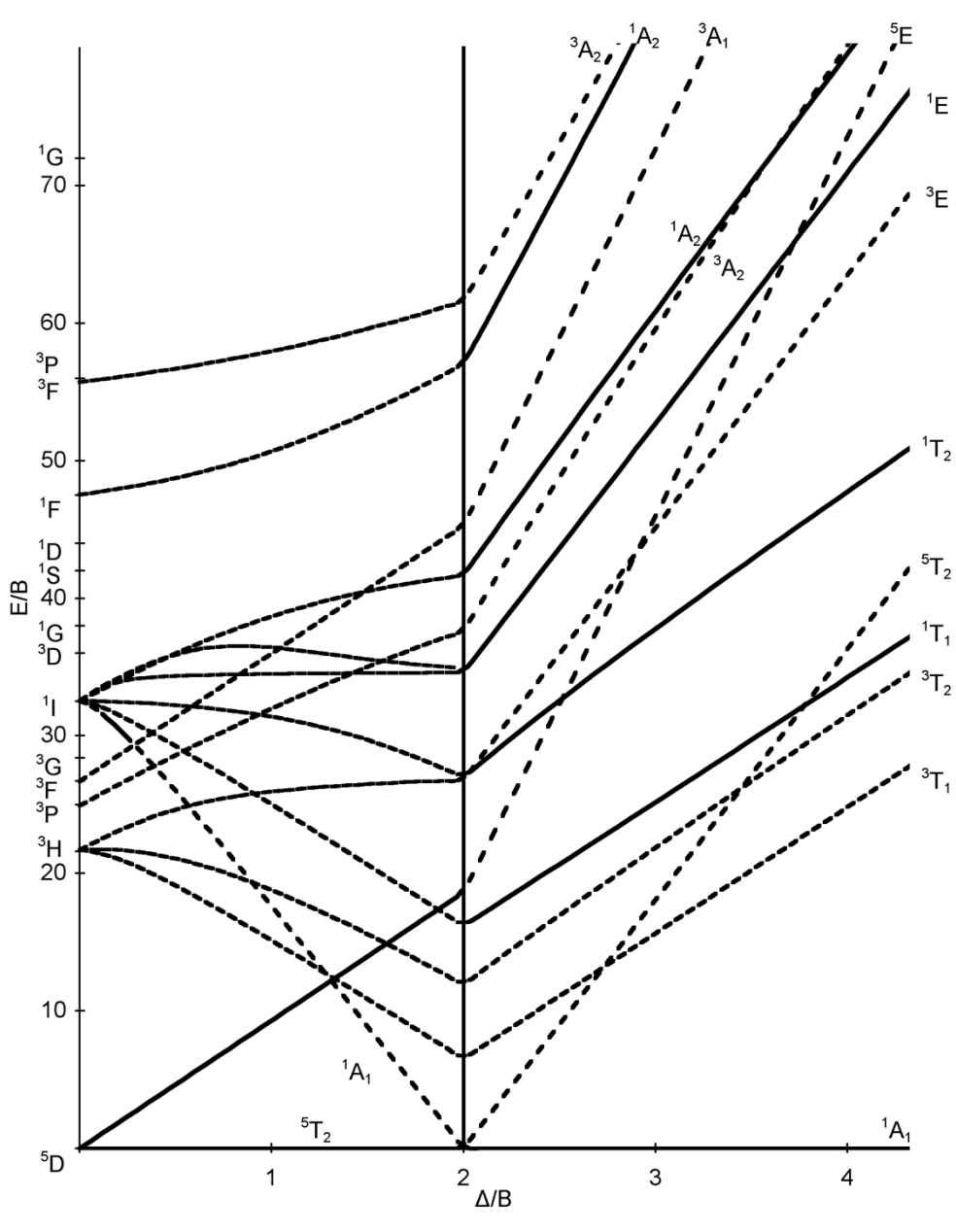
E/B
Δ/B
^{1}G
70
60
^{3}P
^{3}F
50
^{1}F
^{1}D
^{1}S
40
^{1}G
^{3}D
^{1}I
30
^{3}G
^{3}F
^{3}P
^{3}H
20
10
^{5}D
1
2
3
4
^{3}A$_2$
^{1}A$_2$
^{3}A$_1$
^{5}E
^{1}E
^{3}E
^{1}A$_2$
^{3}A$_2$
^{1}T$_2$
^{5}T$_2$
^{1}T$_1$
^{3}T$_2$
^{3}T$_1$
^{1}A$_1$
^{5}T$_2$
^{1}A$_1$

f) d^7

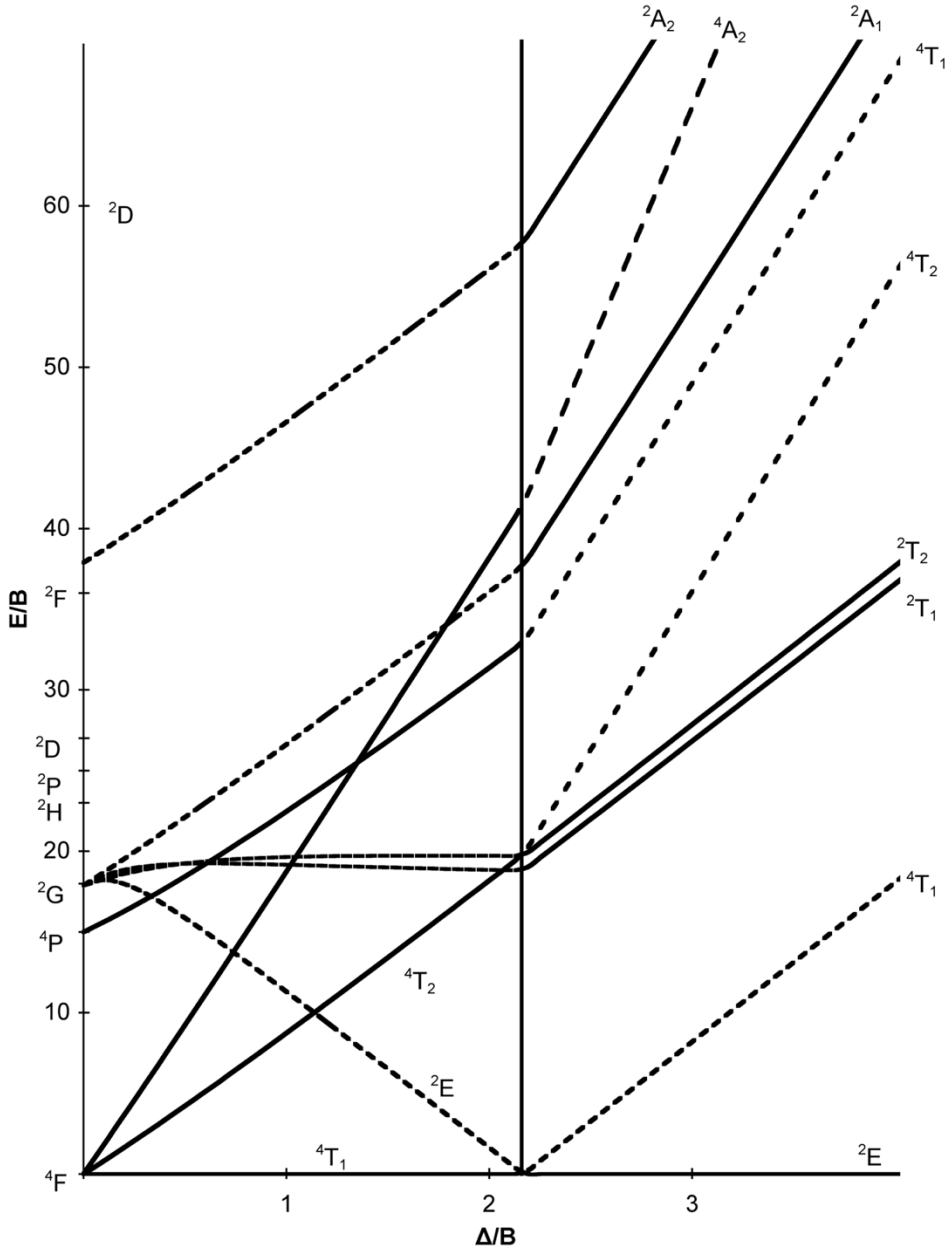
$^2A_2$
$^4A_2$
$^2A_1$
$^4T_1$
$^4T_2$
$^2T_2$
$^2T_1$
$^4T_1$
$^4T_2$
^2E
$^4T_1$
^2E
^2D
^2F
^2D
^2P
^2H
^2G
^4P
^4F
60
50
40
30
20
10
1
2
3
E/B
Δ/B

g) d^8

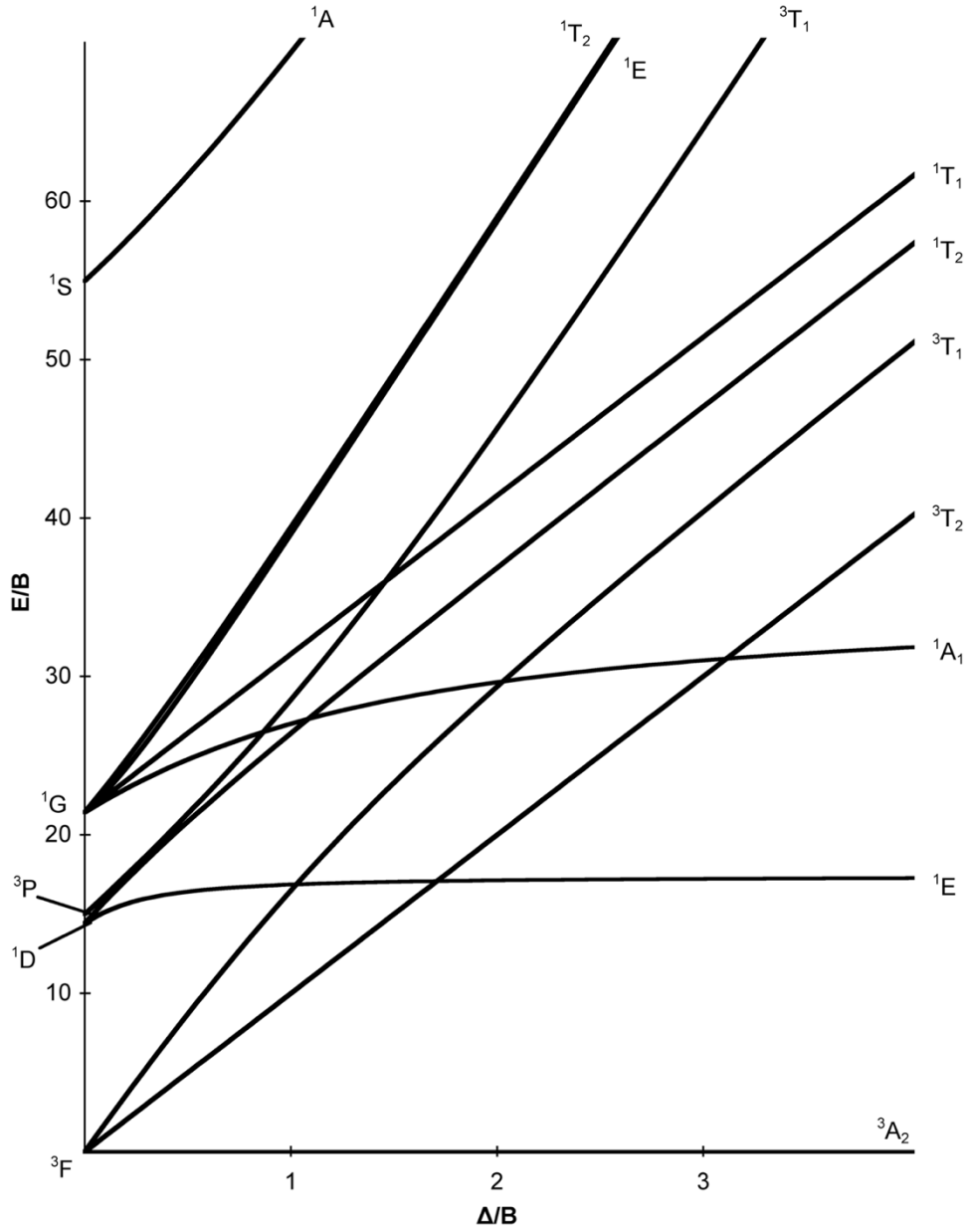
^1A
$^1T_2$
^1E
$^3T_1$
$^1T_1$
$^1T_2$
$^3T_1$
$^3T_2$
$^1A_1$
^1E
^1S
^1G
^3P
^1D
^3F
$^3A_2$
60
50
40
30
20
10
E/B
1
2
3
Δ/B

Figure 2.3: Tenabe-Sugano diagrams depicting energy levels of transition metals with respect to crystal field strength.

Multiple electron systems are shown as a) d^2, b) d^3, c) d^4, d) d^5, e) d^6, f) d^7 and g) d^8. Figure taken from [50] *without changes and licensed under Creative Commons BY-NC-SA 3.0 US.*

The vertical lines and change in slope of the excited state energy present at particular *Dq/B* values presented in some of the Tenabe-Sugano diagrams are of interest. This represents the crossover point of the two lowest lying energy states, in which a new ground state is established at that particular crystal field strength *Dq*.

The surrounding anions also play an important role in determining the local crystal field of the central 3*d* ion. This is governed by the nature of the bonding between the atoms. In general, the trend for crystal field strengths of various anions, referred to as the spectrochemical series, is found to be:

$$I < Br < Cl < S < F < O < N < C$$

2.2.3. Mn^{2+} Emission in YAG

Manganese can take on several valence states, from +2 to +7.[47] As such, the scope of this research was limited to one valence state of interest, Mn^{2+}. Mn^{2+} is an interesting phosphor activator, since as a d^5 material, exactly half of the 3*d* orbital is filled, leading to remarkable chemical stability. Moreover, as can be seen from Figure 2.3 d), the transitions of Mn^{2+} are linear, and are therefore highly dependent on the strength of the local crystal field.

Mn^{2+} in YAG has been shown to exhibit $^4T_1 \rightarrow {}^6A_1$ luminescence, which corresponds to an orange appearing emission of ~590 nm and a *Dq/B* value of ~2.[15,47,51,52] However, due to the size of the Mn^{2+} ion (ionic radii of 0.67 Å and 0.96 Å for octahedral and dodecahedral coordination, respectively), it is still unclear whether it populates the octahedral Al site (r = 0.535 Å), or the dodecahedral Y site (r = 1.019 Å).[15,52,53]

As discussed above, this transition is partially forbidden, and as such, the oscillator strength and by extension luminescence intensity is fairly weak in YAG. Moreover, as a 2+ ion occupying a Y^{3+} or Al^{3+} site, charge compensation via the addition of a 4+ ion, such as Si^{4+} or Ge^{4+}, is often required to maintain charge neutrality.[52]

2.3. Rare Earth Luminescence in YAG

The rare earth elements consist of the lanthanide series in the periodic table (La-Lu), as well as the elements Sc and Y. Luminescence of rare earth ions is very similar to that of transition metals, in that the electronic transitions of rare earth elements occur in the 4*f* shell rather than 3*d.* This brings about a significant difference, however: whereas 3*d* orbitals of transition metals are directly involved in bonding, the 4*f* shell of rare earths is shielded from outermost bonding orbitals. With very little influence from the surrounding atoms, the transitions involved in rare earth luminescence have extremely narrow linewidths. This shielding effect makes rare earth dopants largely insensitive to their surrounding crystal field, and so they can be used in a wide array of host materials.[47] Rare earth materials sometimes act as the luminescent center for laser applications, such as the

well known Nd:YAG laser. In YAG, these larger rare earth ions typically occupy the large dodecahedral Y site.

In 1963, Dieke and Crosswhite set about trying to characterize the electronic states available for 4*f* transitions of the rare earth ions, producing the often referenced Dieke Diagram (Figure 2.4).[54] This diagram allows for determining available 4*f*-4*f* spectroscopic transitions of triply ionized rare earth ions at a glance. Electronic states are indicated by the notation $^{2S+1}L_J$, where S is the spin angular momentum, L is the orbital angular momentum (S, P, D, F, G, H, I, K, L, M, etc.), and J is the total angular momentum. Transitions which produce emissions in the visible range occur at ~20x10^3 cm^{-1}.

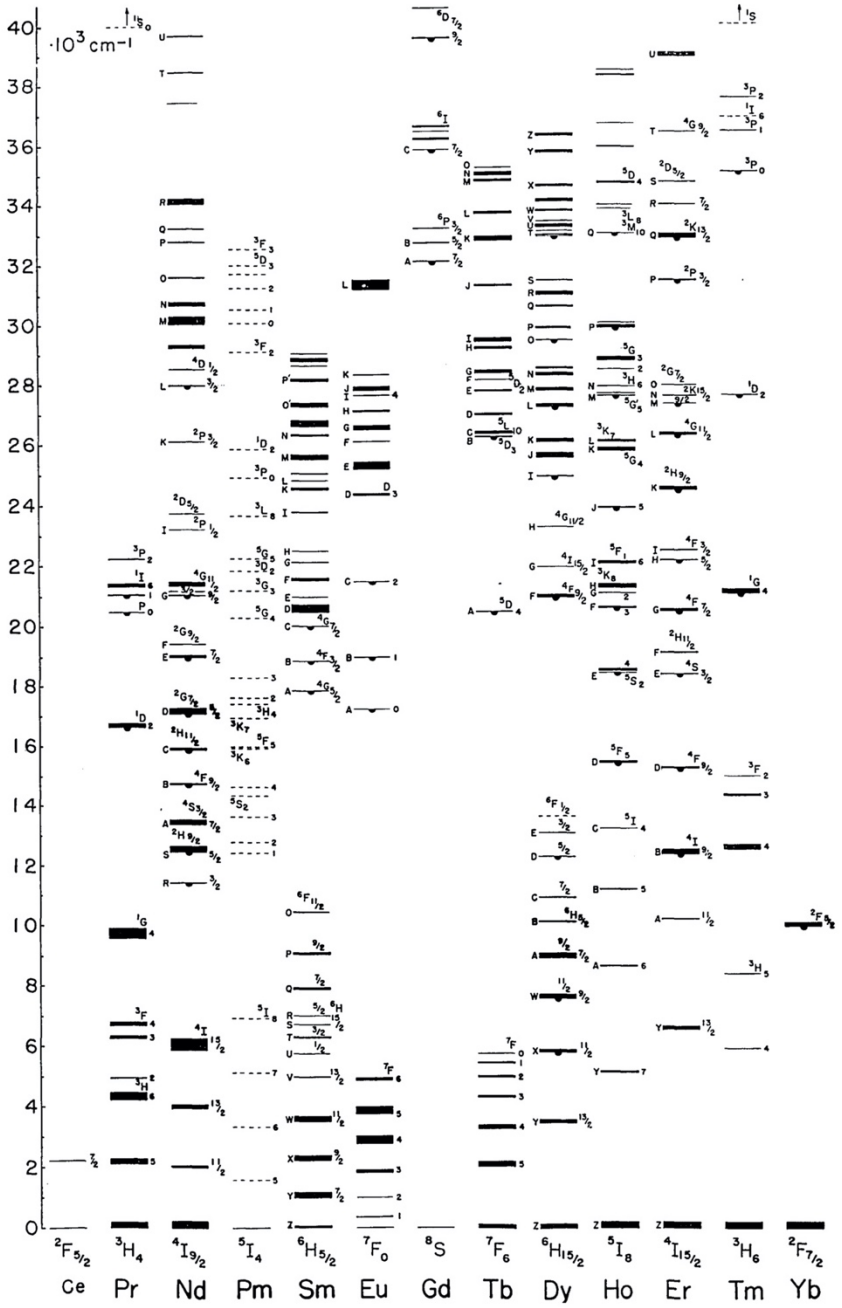

Figure 2.4: The Dieke diagram depicting 4f-4f electronic transitions available to trivalent rare earth ions.

Reprinted with permission from [54] © The Optical Society.

2.3.1. Ce Emission in YAG

Ce is a rather interesting rare earth ion, in that it differs greatly from the other rare earths. As can be seen from the Dieke Diagram in Figure 2.4, only one 4*f*-4*f* transition is possible for Ce, due to the Ce^{3+} ion having only one electron occupying the 4*f* orbital. However, among the rare earths, Ce has the lowest lying 5*d* orbitals available to make transitions from the 4*f* ground state. These outer lying 5*d* orbitals are not shielded, and thus their energy depends almost entirely on the crystal field splitting provided by the host. This, in turn, greatly influences the energy of the transitions available to Ce, which then directly affects its optical characteristics. Moreover, the 5*d* → 4*f* transition is parity allowed, and so the absorption and emission intensities of Ce-based phosphors are relatively strong.[47]

The 5*d* orbitals of Ce experience a significant degree of crystal field splitting in the YAG host, with the lowest lying energy state ~$18x10^3$ cm^{-1} above the 4*f* ground states. The most prominent absorption peak in Ce:YAG occurs around 450 nm, with a second peak present at 390 nm. The two terminating energy states, $^2F_{5/2}$ and $^2F_{7/2}$, contribute to a broad emission profile centered around 530 nm. As mentioned previously, this provides absorption in blue and emission in yellow-green, with a notable lack of red in the emission profile. The phosphor itself is a yellow colour under room lighting conditions.

Since the absorption and emission characteristics are so highly dependent on the strength of the local crystal field, techniques have been explored to adjust the luminescent properties of Ce in YAG with the addition of atoms of different sizes to alter the interatomic spacing of Ce with its neighbouring atoms. This most often involves the addition of Gd in the Y site, although modifications via the Al sites have been demonstrated with the addition

of Ga and Mg.[43-45] This effect may be explained by the configurational coordinate model, discussed later in this chapter.

The parity allowed $4f \rightarrow 5d$ transitions produce high oscillator strengths, and as such, they have been shown to influence the oscillations of nearby non-parity allowed transitions through non-radiative energy transfer via dipole-dipole coupling.[55-58] This includes energy transfer to other rare earth ions, such as sensitizing Nd, Pr, and Yb, but also transition metal luminescent centers, such as Mn^{2+}.[55-58]

2.4. The Configurational Coordinate Model

The configurational coordinate model can be used to describe optical properties of a localized luminescent center. The model uses the potential energy of the ground and excited states as a function of its configurational coordinate, which is, in its most basic form, a measure of the interatomic distance between the central luminescent ion and its nearest neighbour. While mostly a qualitative model, the configurational coordinate model helps to explain observed optical phenomena, such as:

- Stokes' law, which states that the energy of absorption event is usually larger than the energy of an emitted photon, with the difference in energy referred to as the Stokes' shift.
- The width of absorption and emission bands, and their temperature dependence.
- The energy required for thermal quenching of luminescence.

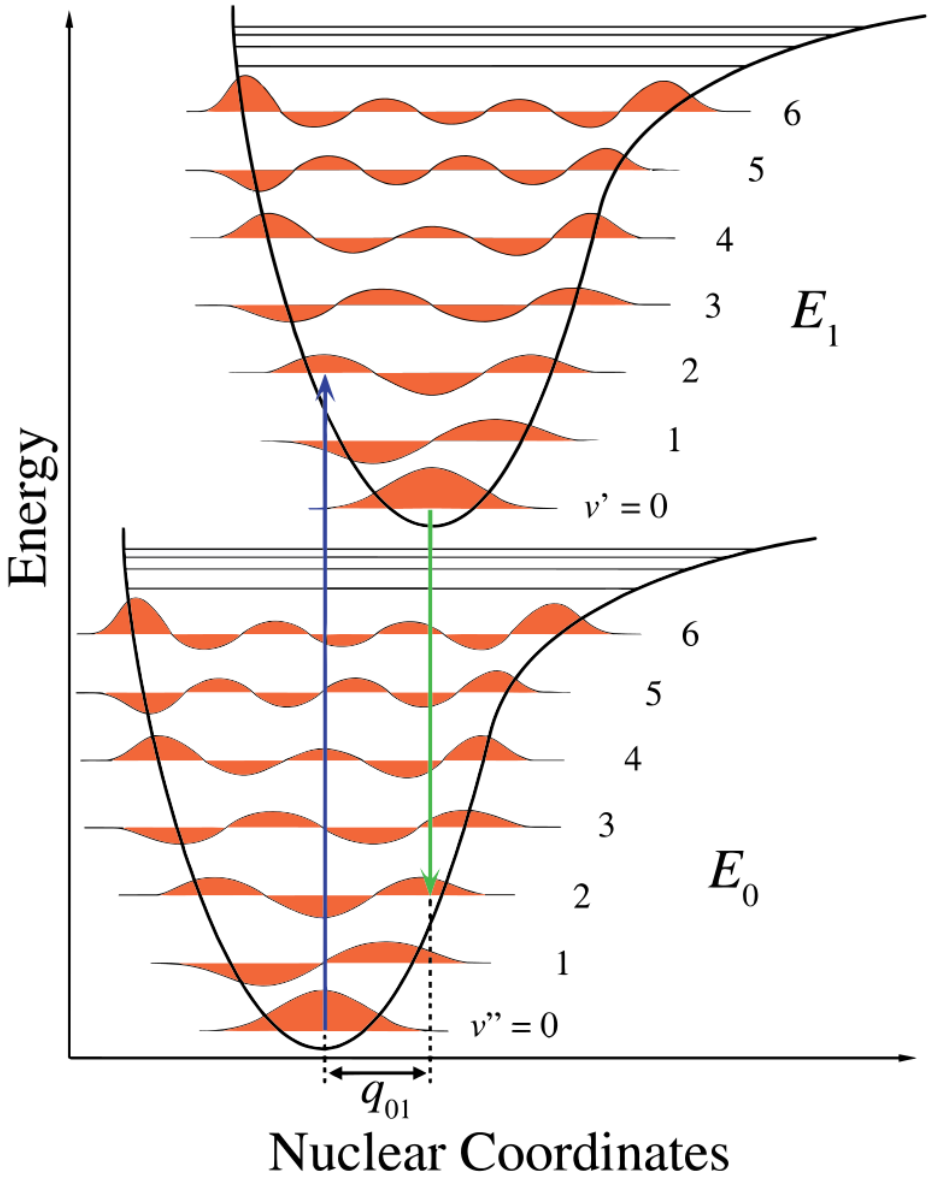

Figure 2.5: Configurational coordinates diagram of localized emission centers. Transitions between ground state E_0 and excited state E_1 at spatial offset q_{01} occur to energy levels where there is significant overlap of the wavefunctions. Figure taken from [59] without changes and licensed under Creative Commons BY-NC-SA 3.0 US.

Figure 2.5 depicts a series of processes that describe the absorption and emission events found in localized luminescent centers. Transitions occur where there is a high degree of spatial overlap in vibrational modes of the ground state and spatially offset excited state wavefunctions, and once in the excited state, the electron relaxes to the excited state minimum before relaxing radiatively to the ground state.

The potential energy in the bond between the luminescent ion and its neighbour can be represented by Hooke's law, with the displacement from an equilibrium position of the central ion denoted as Q. The total energy of the ground and excited states can therefore be expressed as:

$$U_g = \frac{K_g Q^2}{2} \tag{2.14}$$

$$U_e = \frac{K_e (Q - Q_0)^2}{2} + U_0 \tag{2.15}$$

Where U_g and U_e are the total energy of the ground and excited state, respectively, K_g and K_e are the force constants associated with the chemical bond, Q_0 is the interatomic distance between the ground and excited state at equilibrium, and U_0 is the total energy at $Q = Q_0$.

As discussed in Chapter 2.1, the wavefunctions of the ground and excited states must have different spatial distributions for a transition to occur. In addition, the spatial distribution of the excited state wavefunction may be influenced by neighbouring ions, further adding to the spatial offset of the ground and excited states in configurational

coordinate space. Both of these factors contribute to the Stokes' shift. It should also be mentioned that this model also encapsulates the Franck-Condon principle, which states that the recoil of the nucleus is negligible during absorption and emission events, i.e. the nucleus remains in the same position during all processes described.

Thermal fluctuations will cause the energy in each state to oscillate around the equilibrium position by an amount up to kT, where k is the Boltzmann constant, and T is the temperature in Kelvin. It is these oscillations in the energy curves that contribute to the broadening of the absorption and emission bandwidths.

Figure 2.5 also depicts an intersection point of the ground and excited state energy curves. This intersection demonstrates that at high enough temperatures, there exists a non-radiative relaxation pathway.

Chapter 3: Bottom Up Synthesis of Nanoparticles

Synthesis of nanomaterials has become an extremely active topic of research, as many desirable applications become accessible when a material is confined spatially. For example, size reduction of transistors allows for faster computing and reduced power consumption, and quantum dots allow for semiconductor based displays using the same material at different particle sizes to produce colour that is particle size-dependent.

Nanofabrication can be separated into two broad categories: bottom up or top down. The top down approach involves removal of material from a stock source, similar to chiseling marble to make a statue. This approach to nanofabrication is often seen in applications which start with a thin film, and form the nanoscale features by means of etching or lithography. While this process has several advantages, such as being compatible with current semiconductor processing methodology, it requires high resolution electron beam lithography, masks and alignment of those masks, and anisotropic etch solutions. Conversely, the bottom up approach involves building up the nanostructures atom by atom. This approach can be used in the vapour phase, such as in the cases of molecular beam epitaxy (MBE) and chemical vapour deposition (CVD), however it is also often seen in solution based processing. The latter approach presents several advantages, such as ease of scale up, the possibility of roll-to-roll processing, and a high degree of control over particle size and morphology. Control of particle size and morphology can be accomplished by tuning experimental parameters such as reaction time, temperature, and with the use of surface stabilizers such as surfactants.[60] Another significant advantage of solution-based processing is that the particle surface area, which is significantly higher at the nanoscale

compared to the same material in bulk, can be highly functionalized with the use of surface modifying agents either *in situ* or in post processing, shown schematically in Figure 3.1. This chapter aims to explore these concepts in detail, and examine the kinetics of bottom up synthesis of nanoparticles in solution.

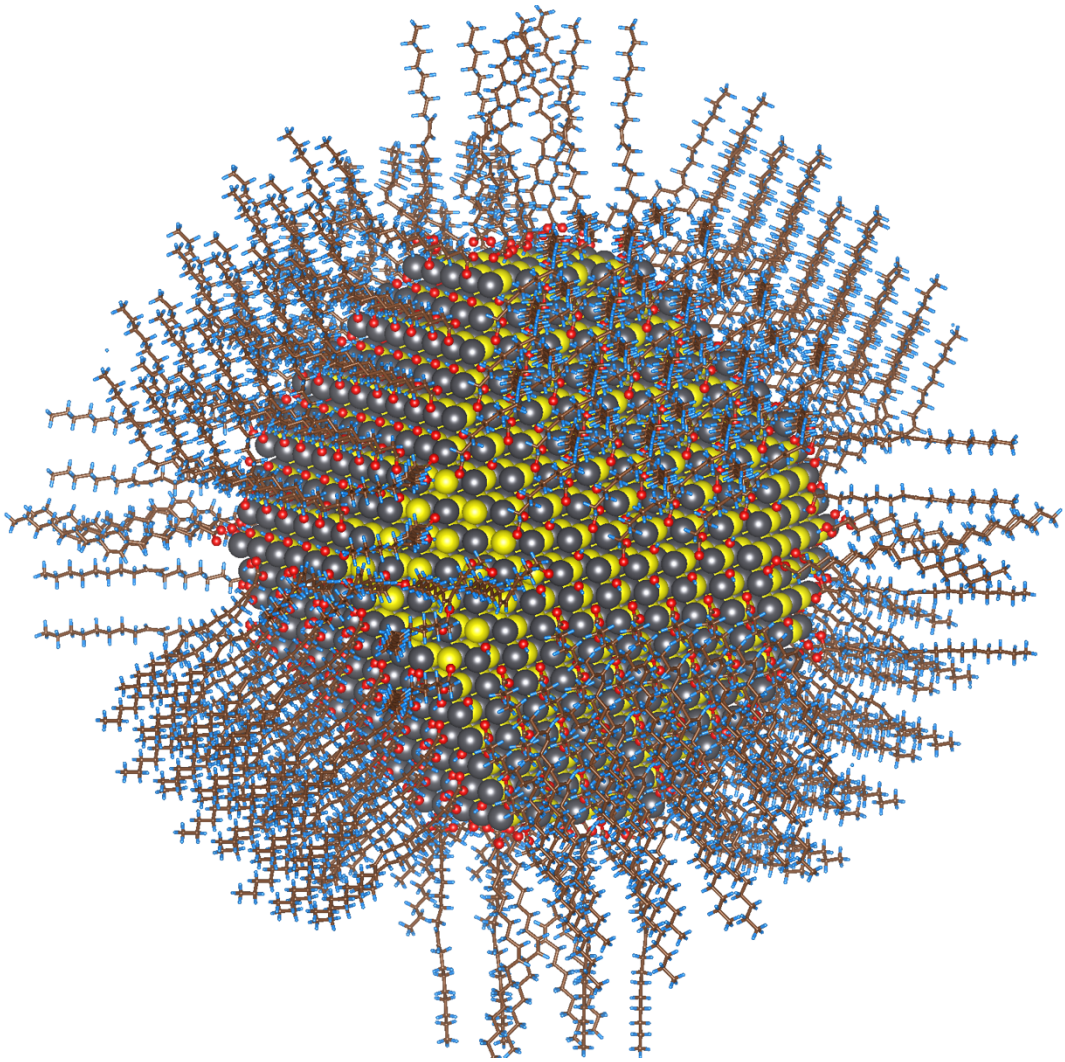

Figure 3.1: Schematic of a bottom up synthesized nanoparticle with surface passivation. Figure taken from [61] without changes and licensed under Creative Commons BY 4.0.

3.1. Kinetics of Nanoparticle Synthesis

The kinetics of reaction in this section is limited in scope to the bottom up synthesis of nanoparticles fully contained in a liquid medium. Some factors to keep in mind are that in a liquid solvent, the atomic species must be introduced as a precursor, and that precursor must be soluble in that solvent. The precursors can be either a salt or molecule, and they must be able to fully decompose to form reactive monomers. Surfactants can be added to tie up bonds on the monomer to limit uncontrolled growth, however, care must be taken in their selection so that they can also de-sorb to facilitate controlled growth. As such, surfactants can be thought of as dynamically adsorbed molecules. Generally, these surfactants contain a head group which can share an electron, such as carboxylic acids, halides, phosphates, etc. such that they can bind to the particle surface, and also contain functional groups which are soluble in the reaction solvent to promote monomer solubility. Surfactants play an important role in nanoparticle synthesis, as not only do they promote monomer solubility, but they also provide electrostatic repulsion and/or steric hinderance between growing particles to limit particle size.[60] They remain on the particle surface after the reaction is complete, but can also be removed and replaced with other surfactant molecules to extend the nanomaterial's functionality. For example, if the reaction solvent is a nonpolar organic solvent, but the intended application is for biological use, the surfactant may be exchanged for one which is water soluble.

Control of nanoparticle size distribution made using bottom up synthesis methods is maintained by separating the reaction kinetics into two stages: particle nucleation and particle growth.[60] The details of these processes will be outlined in the next section.

3.1.1. Nucleation of Precursors

Consider the reaction medium as a fully liquid phase matrix. In this case, all of the bonds of the precursor atoms are saturated with no dangling bonds, and as such, this medium is in a relatively low energy state. However, as these precursors come into contact under the right thermodynamic conditions, they can form the beginnings of a nanoparticle through a process known as nucleation. There are three categories of nucleation: homogeneous nucleation, heterogeneous nucleation, and secondary nucleation.[60]

Homogenous nucleation can be thought of as two phases of the same material, essentially just a thermodynamic phase change. For example, if the system fully consists of liquid water that is then cooled to 0 ºC, some molecules will condense and begin to nucleate into a solid. In this case, the material nucleates in the presence of only itself.

Heterogeneous nucleation is where things get more interesting. Heterogeneous nucleation occurs in systems where solute precursors are dissolved in a solvent, i.e. a multi-material, one phase system. Nucleation occurs when precursor atoms are precipitated out of the solution, forming a solid phase in the liquid matrix. Precipitation into the solid phase is possible when the concentration of precursor ions exceeds the solubility limit of the solvent, i.e. when the solvent becomes supersaturated.[60] Heterogeneous nucleation can also be initiated by the presence of a pre-existing surface, such as impurities, the reaction vessel wall, or a substrate.

Secondary nucleation is similar to heterogeneous nucleation, in that it occurs in the presence of pre-existing structures. Secondary nucleation can be thought of as nucleation

seeds. The seed material can be the same as the final product, or a secondary material, resulting in deposition of the precursors onto the seed surface in a core/shell architecture. Secondary nucleation provides several advantages, namely by reducing the nucleation energy barrier by providing a surface to deposit on, as well as opening up new design spaces such as those seen in core-shell quantum dots.[60]

Nucleation is a fairly high energy process. The system is going from a low energy state with all bonds saturated to forming a new surface, with all the energies associated with that. There is a significant energy barrier required to form a new surface from the low energy solvated precursor, combined with the fact that the surface area-to-volume ratio is high at the nanoscale.

The energy required for nucleation can be described as:

$$\Delta G_{tot} = \Delta G_{bulk} + \Delta G_{surface} \tag{3.1}$$

where ΔG_{tot} is the Gibbs free energy required to form one nanoparticle, ΔG_{bulk} is the Gibbs free energy of the interior volume, i.e. bulk, and $\Delta G_{surface}$ is the Gibbs free energy of the surface. Assuming spherical nanoparticles:

$$\Delta G_{tot} = \left(\frac{\frac{4}{3}\pi r^3}{n_v}\right)\Delta\mu + 4\pi r^2\gamma \tag{3.2}$$

where r is the radius of the nanoparticle, n_v is the number of atoms per atomic volume, $\Delta\mu$ is the change in chemical potential per atom to change phase, and γ is the surface energy.

It is helpful to further put the bulk and surface terms in terms of the number of atoms associated with each. The number of atoms which comprise the bulk can be expressed as:

$$N\Delta\mu = N(\mu_f - \mu_i) = -N\, k_b T ln S \tag{3.3}$$

where S is the supersaturation parameter, which can further be expressed as:

$$S = \frac{C}{C_e} \tag{3.4}$$

where C is the concentration of the precursors in the system, and C_e is the equilibrium concentration at temperature T. Conceptually, this represents the number of atoms involved in the phase change times the phase change potential per atom. If the atmosphere is supersaturated, it becomes energetically favourable to make the phase change. Moreover, the system is now defined in terms of temperature and pressure, which can be experimentally controlled.

The same treatment can be applied to the surface term. The surface energy is also related to the number of atoms in the system, which can be found from the volumetric relationship:

$$V = \frac{4\pi r^3}{3} = a_v N \tag{3.5}$$

where a_v is the atomic volume. Solving for r and substituting into the equation for the surface area of a sphere gives the relationship between the surface area and volume with respect to the number of atoms in the system:

$$4\pi r^2 = 4\pi \left(\frac{3a_v}{4\pi}\right)^{2/3} N^{2/3}$$

(3.6)

Finally, solving for r gives the radius of the sphere in terms of N:

$$r = \left(\frac{3a_v}{4\pi}\right)^{1/3} N^{1/3}$$

(3.7)

This can now be used in Equation 3.2 for the total free energy required to undergo a change of phase, solely with regards to the number of atoms N:

$$\Delta G_{tot} = -Nk_bTlnS + 4\pi\gamma \left(\frac{3a_v}{4\pi}\right)^{2/3} N^{2/3}$$

(3.8)

Once nucleation has occurred, the nanoparticle will reduce its energy in one of two ways: the atoms can dissolve back into the solvent, or more atoms can be added on the surface to reduce the surface area-to-volume ratio. That is to say, there is some critical size of a budding particle, made up of a critical number of atoms, required to sustain nucleation. Moreover, there is a critical concentration of precursors required to ensure enough monomers are available to deposit onto the particle surface, such as when the system is in supersaturation. This critical concentration of precursors, where the particle is neither growing nor shrinking, can be found at $\frac{d\Delta G_{tot}}{\mathrm{dN}} = 0$, shown schematically in Figure 3.2.

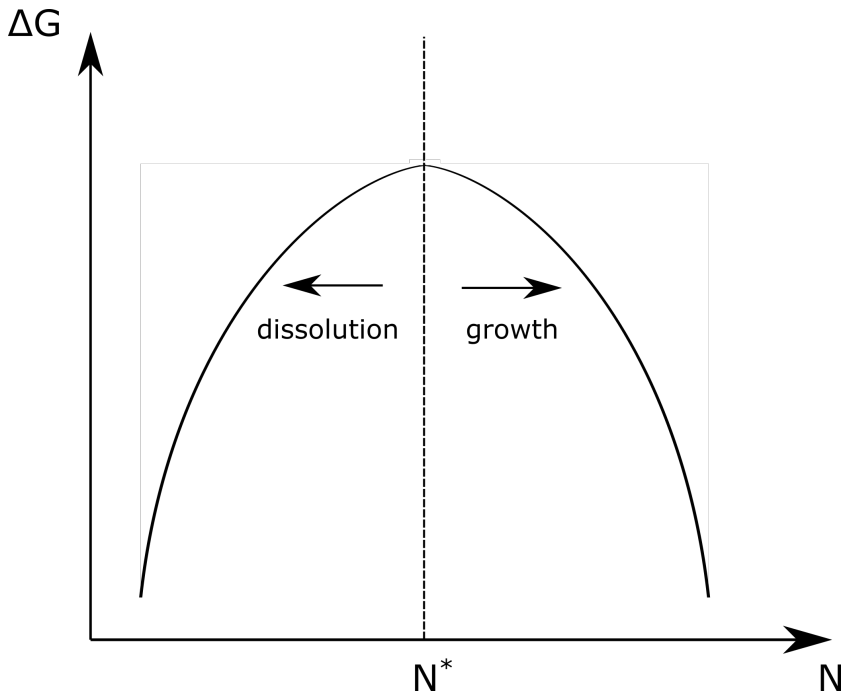

Figure 3.2: Schematic depicting Gibbs free energy as a function of number of atoms comprising a nucleated nanoparticle.

At the critical number of precursor atoms N^*, the system will reduce its energy by dissolving back into solution or growing further.

Taking the derivative of Equation 3.8 and setting it to zero gives:

$$\frac{d\Delta G_{tot}}{\mathrm{dN}} = -k_b T ln S + \frac{8\pi\gamma}{3}\left(\frac{3a_v}{4\pi}\right)^{2/3} N^{1/3} = 0$$

(3.9)

The critical number of atoms N^* can be found by solving for N:

$$N^* = \frac{32\pi\gamma^3 a_v^2}{3(k_b T ln S)^3}$$

(3.10)

Similarly, using equation 3.7, the critical size can be found to be:

$$r^* = \frac{2\gamma a_v}{3(k_b T ln S)^3} \quad (3.11)$$

Note the inversely proportional relationship between both the temperature and supersaturation parameter on N^* and r^*. An increase in temperature or concentration of precursor yields smaller critical concentrations and sizes, resulting in smaller nucleation clusters.

3.1.2. Growth of the Nanoparticle

Once nucleation has been achieved, other factors must be considered for the growth step. For example, over time, as precursors are consumed during nucleation, the average size of the growing particles will start to converge. This effect is called focusing, as the particle size distribution begins to narrow as precursors become less available. In order to keep the kinetics in favour of maintaining a small standard deviation in particle size, r^* should remain less than r_{avg}, the average size of the particles.

There are two modes of growth kinetics: diffusion limited growth, and reaction limited growth.[60] Diffusion limited growth is the case when the rate of reaction, and therefore particle growth, is limited by the rate of transport of precursors through the solvent to the particle surface. In the case of reaction limited growth, the growth rate is limited by the rate of reaction of the precursors at the particle surface, for example if the precursors must first adsorb, if there's steric hinderance, etc. Before diving into the details

of these growth modes, a schematic is presented with which to describe growth kinetics in general, depicted in Figure 3.3.

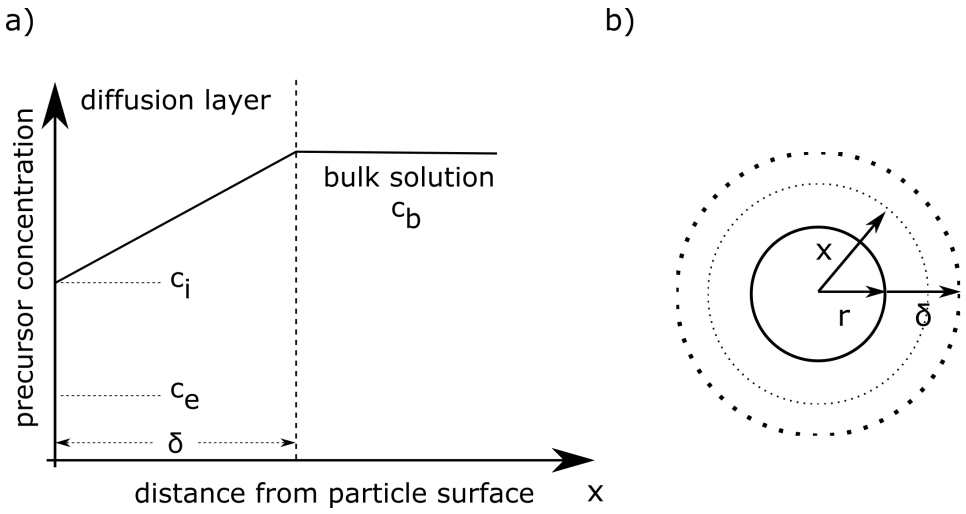

Figure 3.3: Growth model of particle growth kinetics.
a) Precursor behaviour in the diffusion layer at the particle surface. b) Diagram of a growing nanoparticle with radius r.

where c_b is the concentration of precursors in the solvent (i.e. the bulk concentration of precursors), c_i is the precursor concentration at the solvent-particle interface, c_e solubility of the particle (i.e. the equilibrium precursor concentration if the particle was at the critical size r^*), δ is the length of the diffusion layer, and x is the distance from the particle surface.

Assuming the diffusion of the precursors dissolved in the bulk solvent to the particle surface is first order (i.e. linear), the concentration gradient is linear. The diffusion of precursors to the particle surface is then:

$$J = -4\pi r^2 D \frac{dc}{dx} \tag{3.12}$$

where J is the precursor flux to the particle surface, D is the diffusion constant, and $\frac{dc}{dx}$ is the concentration gradient. To find the number of monomers diffusing to the surface,

$$\frac{J}{4\pi D}\int_{r+\delta}^{r}\frac{1}{r^2}dr \;=\; \int_{c_b}^{c_i}dc$$

(3.13)

After working through the integration, the diffusion of precursors to the particle surface J_D is then:

$$J_D = \frac{4\pi D r(r+\delta)}{\delta}(c_i - c_b)$$

(3.14)

Similarly, the reaction kinetics at the surface of the particle can be modelled by:

$$J_S = 4\pi r^2 k(c_e - c_i)$$

(3.15)

where J_S is the precursor flux to the particle surface, and k is the rate constant of the surface reaction in question. However, since only precursors at the surface are available for reaction, the flux to the surface has to come from the diffusion from the bulk solvent. That is to say, $J_S = J_D$. Or, expressed fully:

$$\frac{c_i - c_e}{c_b - c_i} = \frac{D}{kr}(1 + \frac{r}{\delta})$$

(3.16)

The significance of this equation is that it relates the rate of precursors transported to the surface with the rate of reaction at the surface.

Now that precursor transport and reaction kinetics have been related to each other, the limiting factors for diffusion and reaction limited growth of the nanoparticle can be discussed.

Diffusion limited growth assumes that $c_i = c_e$, that is, all of the precursors are consumed as soon as they reach the particle surface. Equation 3.14 becomes:

$$J_D = -\frac{4\pi D r(r-\delta)}{\delta}(c_b - c_e)$$

(3.17)

In this case, the reaction rate of the precursors on the surface is neglected, and so the rate of growth is only related to the precursor flux to the surface. That is to say, the precursor flux to the surface equals the rate of volumetric increase:

$$J_D = \frac{4\pi r^2}{V_m}\frac{dr}{dt}$$

(3.18)

where V_m is the molar volume, and $\frac{dr}{dt}$ is the rate of growth. Equating Equations 3.17 and 3.18, the rate of growth in the diffusion limited case is shown to be:

$$\frac{dr}{dt} = DV_m(\frac{1}{r} + \frac{1}{\delta})(c_b - c_e)$$

(3.19)

As long as the concentration of precursors in the solvent c_b exceeds the solubility limit of the solvent at equilibrium c_e, the particle will continue to grow. One key insight from Equation 3.19 is that if the diffusion layer thickness δ is constant, and $(c_b - c_e)$ is independent of the particle size r, then as the particle size r increases, the growth rate $\frac{dr}{dt}$ decreases. This makes intuitive sense, as when the particle size increases, more precursor

is needed to increase the overall size by an amount dr. This indicates that larger particles do not grow as fast as smaller particles, and over time, the size distribution begins to narrow in a process called focusing.[60]

The second mode by which the nucleated nanoparticle can grow is by reaction limited growth, whereby the growth rate is limited by the chemical kinetics of the precursors reacting on the particle surface. In this case, it is assumed that the particle is getting a sufficient precursor concentration such that $c_i = c_b$. The growth rate of the nanoparticle can then be described as:

$$\frac{dr}{dt} = kV_m(c_i - c_e) = kV_m(c_b - c_e)$$

(3.20)

As mentioned previously, the concentration of precursors is dependent on the rate of diffusion to the particle surface. With this in mind, the assumption that $(c_b - c_e)$ is independent of r must be relaxed, such that it is now dependent on r. The full derivation of the final expression for the growth rate is quite involved and can be found elsewhere[62] however the final expression can be stated in terms of the rate of change of the particle size distribution and the average size:

$$\frac{d\Delta r}{dt} = \frac{k\Delta r}{r_{avg}}\left(\frac{2}{r_{avg}} - \frac{1}{r^*}\right)$$

(3.21)

Where r_{avg} is the average particle radius, Δr is the standard deviation of the radii, and $r^*$is the critical radius, i.e. the size in equilibrium. From this expression, it can be seen that

growth, in this case when $\frac{d\Delta r}{dt} > 0$, occurs when $\frac{r_{avg}}{r^*} < 2$. More generally, the size distribution broadens and narrows based on the concentration of available precursor.

In practice, growth of the nanoparticle is a combination of both diffusion and reaction limited growth modes, however the underlying strategy of separating these growth steps from precursor nucleation is critical to achieving a monodispersed, uniform size distribution.

3.2. The Glycothermal Method

One popular method for producing nanoparticles in solution is the solvothermal method, in which precursors are dissolved in a solvent, placed in a sealed reaction vessel, and allowed to react under autogenous pressure at temperatures above the solvent boiling point. It is derived from the hydrothermal method, in which the solvent is water. There are several advantages to using an organic solvent in place of water, namely that the presence of water can accelerate the growth of the nanoparticles, and often require the addition of surfactants to physically separate the growing particles. In addition, the relatively low boiling point of water compared to other less volatile organic solvents requires reaction vessels capable of withstanding the additional autogenous pressure. The glycothermal method, first proposed by Inoue et al. seems to address these shortcomings.[63] The glycothermal method is a subset of the solvothermal method, requiring the solvent to be a glycol. Glycols are organic hydrocarbons with alcohol functional groups on both ends, for example ethylene glycol. Glycol molecules have boiling points significantly higher than water, and as such, reactions can take place at much lower temperatures. In addition, these

glycol molecules participate in the growth reaction, eliminating the need for surfactant addition and improving the overall purity of the product.

Precursors required for the glycothermal method of YAG take the form of metal alkoxides, which have the form of the central metal atom bound to the conjugate bases of acids or alcohols, such as the yttrium acetate and aluminum isopropoxide used in this research. The glycothermal reaction takes place in three steps, outlined in Figure 3.4. First, the glycol solvent reacts with the alkoxide to form a glycolated moiety. From there, the hydrocarbon chain undergoes an internal cyclization triggered by heat to form an aluminate ion and protonated tetrahydrofuran. Finally, the aluminate ion is able to attack another alkoxide molecule precursor or surface of a growing particle, forming a M-O-M bridge. This process then repeats until the reaction is completed.

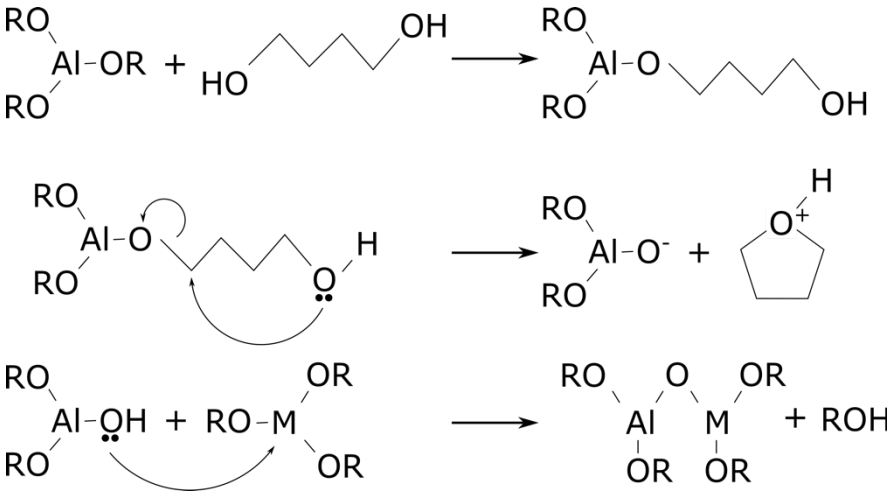

Figure 3.4: The glycothermal reaction mechanism.

The use of alkoxides as a precursor offers several advantages. For example, the relatively inert acetic acid and isopropanol by-products formed do not participate further in the growth reaction, and once the reaction has concluded, the particles are self-capped with the alkoxide.

In terms of choice of which glycol to use as a solvent, it was determined experimentally from Inoue et al. that longer hydrocarbon chain length produced a better crystallized product, peaking at a chain length of 4, corresponding to 1,4 butanediol.[63] It was hypothesized that shorter chain lengths, such as ethylene glycol, could not undergo the cyclization step, and resulted with amorphous or partially crystallized YAG. 1,4 butanediol has been shown to produce phase pure YAG without the need for annealing at temperatures as low as 300 ºC.

Chapter 4: Sample Fabrication

4.1. The Reaction Chamber

This chapter outlines the procedures undertaken to synthesize Ce:YAG-based nanophosphors. The procedures mentioned here are meant to be a general overview, with full experimental details outlined in Chapters 6, 7, and 8. The reaction vessel was a lab-made autoclave, consisting of a 6 inch long, 1 inch outer diameter 316 stainless steel tube with 0.83 inch wall thickness, shown in the inset o. Ferrules swaged onto the ends of the pipe form a compression seal with threaded caps, which had a maximum working pressure of 2635 psig or 179 atm at 315 ºC. The vessel was considered sealed with a quarter rotation of the caps with a wrench after finger tightening. A Teflon liner was manufactured to prevent contact of the reactants with the autoclave wall, but was later switched to a glass test tube.

Figure 4.1: Experimental setup for the glycothermal reaction.
Inset: The glycothermal reaction chamber.

4.2. Synthesis of Ce:YAG Nanophosphors

Ce:YAG nanophosphors were synthesized by first crushing stoichiometric amounts of Ce acetate hydrate, Y acetate hydrate, and Al isopropoxide precursor powders in an agate mortar. The precursors were used as received without further purification or drying.

The crushed powders were added to the 1,4 butanediol (1,4 BD) solvent and allowed to homogenize for 15 minutes with magnetic stirring. The homogenized mixture was transferred to the lined autoclave. In cases where a glass test tube was used as the autoclave liner, 8 mL of 1,4 BD was poured between the glass liner and autoclave wall. The reaction chamber was purged with N_2 and sealed. The reaction chamber was then placed in the lab made oven, consisting of heating tape wrapped around a steel pipe and PID temperature controller shown in Figure 4.1, and brought up to the reaction temperature, either 300 ºC or 315 ºC, over 90 minutes. Once at the reaction temperature, the mixture was allowed to react for 3 hours before cooling to room temperature. Stirring at 300 rpm was achieved by placing the oven on a magnetic stirring plate.

4.3. Doped/intrinsic Core/shell Nanostructures

In cases where an intrinsic YAG shell layer was explored, the same procedure outlined above was followed to produce the initial seeds. Once Ce:YAG nanoparticles were synthesized, the process was repeated with additional Y acetate and Al isopropoxide precursors added to the mixture. Once homogenized by 15 minutes of stirring, the mixture was placed back into the autoclave, and the reaction was repeated. The amount of precursor added to the mixture to produce the shell was taken to be a ratio of the initial precursor concentration, designated as the shell-to-seed ratio.

4.4. Post Processing

Once synthesized, the Ce:YAG nanoparticles are suspended in a mixture with reaction by-products and unreacted precursor, and require a cleaning step. The nanoparticles were washed via centrifugation, in which the as-synthesized mixture was divided into 1.5 mL test tubes and centrifuged at 15, 000 rpm for 10 minutes to separate the solid product from the liquid waste. The liquid waste was decanted, and ethanol was added to the test tube. The solid product was mixed into the ethanol with a stir bar, and this process was repeated 3 times.

Chapter 5: Methods of Sample Characterization

In order to validate the findings of the research in this study, various methods of characterizations were performed on the synthesized samples. This section aims to provide some context of the characterization techniques used and why they might be useful. It is not intended to serve as a comprehensive source for the techniques used, but rather an overview of the physics which make these useful characterization methods. While many methods of sample characterization were used in this body of research, only the most impactful will be discussed in this chapter. These characterization techniques were used to characterize both structural and optical properties of the Ce:YAG nanophosphors synthesized in this study.

5.1. X-Ray Diffraction

X-ray diffraction has become an invaluable structural characterization technique due to its speed, sensitivity, and flexibility. The technique is used to identify structural information of solids. When a crystalline sample is exposed to a beam of monochromatic x-rays, a diffraction pattern is produced, since the wavelength of the x-rays are on the same order of magnitude of the crystal lattice spacing (~1-10 Å).

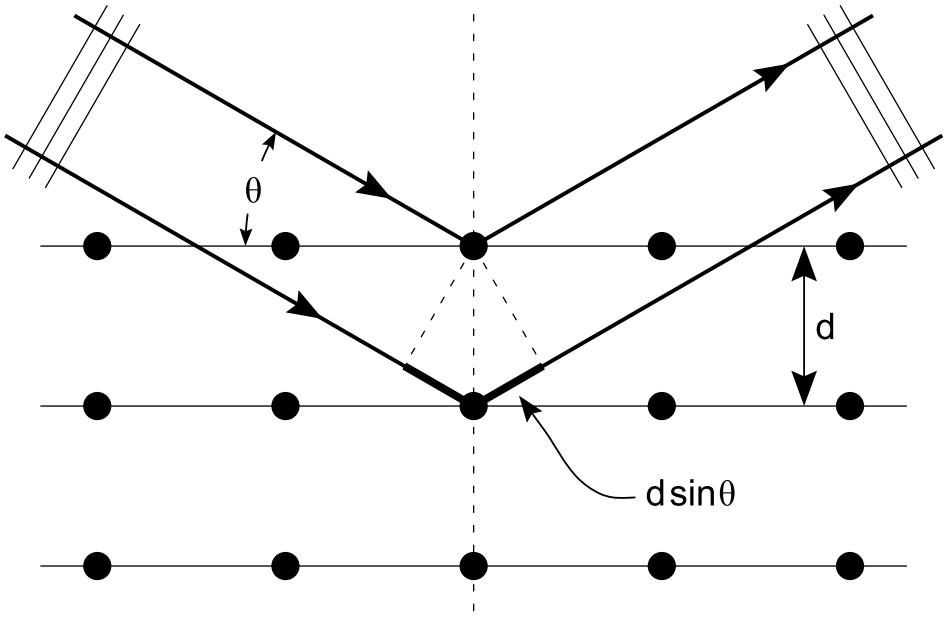

Figure 5.1: Bragg diffraction model of plane wave x-rays interacting with a crystal lattice. Constructive interference of the reflected waves is produced when the condition $2dsin\theta = n\lambda$ *is satisfied. Figure taken from [64] without changes and liscenced under Creative Commons Attribution Share Alike 3.0 Unported license.*

This diffraction pattern is due to the interaction of the x-rays with the crystal planes, with constructive interference occurring at angles given by Bragg's law:

$$2dsin\theta = n\lambda \tag{5.1}$$

where d is the lattice spacing, θ is the incident angle of the beam, n is an integer, and λ is the wavelength of the x-ray beam. Constructive interference occurs when the path length difference of two waves differs by an integer multiple of the incident wavelength. By controlling the incident beam angle, the lattice spacing of the crystal can be extracted from the bright spots of the diffraction pattern.

The case of powders differs slightly, namely that it is assumed that each powder grain is randomly oriented, and as such, the atomic planes of each crystal orientation is able to diffract the incident x-ray beam. Instead of bright spots which result from the x-rays diffracting through a single crystal, bright rings are formed as the beam diffracts through the randomly oriented powder. These two-dimensional diffraction patterns are unique to materials and phases, and can be used to characterize unknown samples. Moreover, analysis of the peak widths and positions can be used to extract microstructure information such as subtle changes in the lattice parameter and crystallite size. For example, the width of the peak is directly proportional to the number of crystal planes the x-ray beam interacts with. More crystalline planes will produce a narrower peak width, which can then be used to estimate the crystallite size.

In addition, unknown samples can be compared against a compiled database of materials maintained by the International Centre for Diffraction Data (ICDD). Comparing to known materials can be extremely useful for quantifying changes in the lattice due to effects such as doping, stress or strain at an interface, etc.

5.2. Nuclear Magnetic Resonance

5.2.1. Single Pulse Excitation

Atomic nuclei exhibit spin, and as such, experience a magnetic moment. Nuclear magnetic resonance (NMR) is a technique used to characterize materials based on the magnetic moment unique to various atomic nuclei. NMR relies on the use of a very strong

magnetic field, often several tens of Tesla, to align the nuclear spins with the magnetic field. Once aligned, a radio frequency (RF) pulse at a frequency resonant with the nuclei under observation is applied. This RF pulse perturbs the magnetic moment of the nuclei such that it is out of alignment with the main magnetic field, and the time to re-align with the field can be measured. This technique, which probes the entire sample, is referred to as single pulse excitation (SPE).

The realignment of the magnetic moment induces a time-varying voltage in a sensing coil, and frequency-domain data can be extracted with the use of a Fourier transform to give NMR spectroscopic data. Spectroscopic data is given in terms of the shift in frequency measured with respect to the RF signal frequency, known as the chemical shift. The measured frequency shift often only differs from the reference MHz signal by ~10-100 Hz, and as such is reported as parts per million, or ppm. This extremely high sensitivity of NMR enables identification of characteristic functional groups and spatial configurations, as the signal for C=O will have a slightly different chemical shift from C(=O)OH, for example, even though the same probe signal is used.

Often, the probe signal used corresponds to the resonance of ^{1}H in the magnetic field of the instrument, as this is the most abundant atom and therefore contributes the strongest signal. However, it is possible to probe other elements, provided they have a net non-zero magnetic moment. On a similar note, if the sample needs to be dissolved in a solvent, care must be taken to ensure that the solvent does not provide an appreciable signal in the measurement. Typically, solvents used are deuterated, using deuterium (^{2}H), in place of hydrogen. Solids may also be measured, although interactions between nuclei in the

crystal can broaden the measured signal. The z-component of the local magnetic field B_{uz} produced by a magnetic dipole μ at a distance r can be described as:

$$B_{uz} \propto \frac{\mu}{r^3}(3\cos^2\theta - 1) \quad (5.2)$$

The z-component of the magnetic field can be reduced to zero by spinning the sample at $\theta = \arccos\frac{1}{\sqrt{3}}$, or ~54.7°. This minimizes interactions between nearby nuclei, and improves spectral resolution.

a)

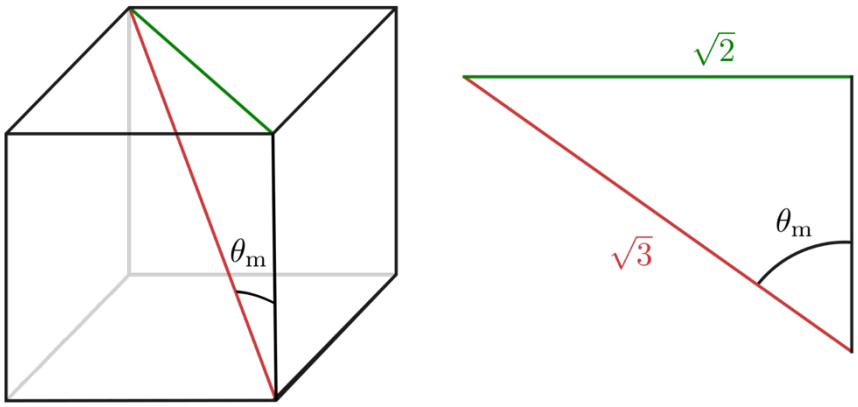

b)

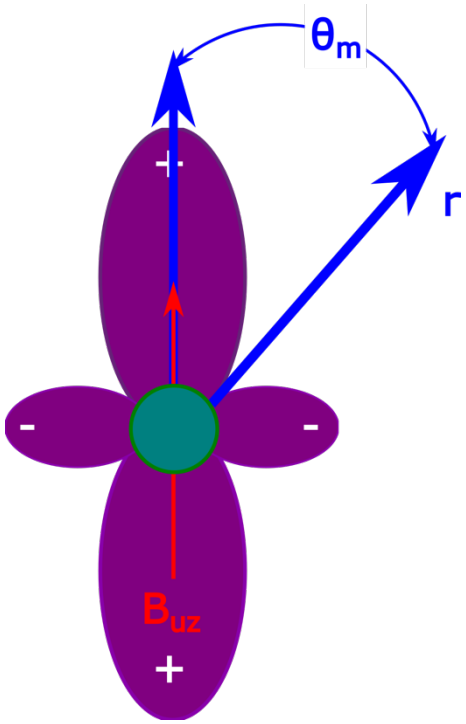

Figure 5.2: Magic angle used in NMR spectroscopy.

a) Geometric representation of the magic angle $\theta_m \approx 54.7º$. Figure taken from [65] without changes and licensed under Creative Commons BY 4.0. b) Schematic showing a minimization of contributions from the magnetic dipole moment of a nuclei when the sample is tilted at the magic angle.

5.2.2. $^{1}H \rightarrow {}^{27}Al$ Cross Polarization

While SPE NMR spectroscopy provides high resolution structural information about the sample as a whole, there is often interesting features exclusive to the surface. In this case, it would be beneficial to target nuclei which are only present on the surface, while measuring a secondary nuclei of interest. This is exactly the case for cross polarized (CP)

NMR. An RF pulse which is resonant to one of the nuclei is applied to the sample, and the energy of the dipole interaction is transferred to a secondary nuclei of interest within close proximity. The relaxation of this second nuclei can be observed, and structural information local to the primary nuclei can be obtained.

In the samples used in this study, ^{27}Al nuclei occupy two different configurations in the nanocrystal, octahedral symmetry and tetrahedral symmetry. These two configurations exhibit slightly different magnetic moments which can be resolved with NMR spectroscopy. Hydrocarbon species stabilize the surface of the nanocrystals, and so the only presence of ^{1}H are near the particle surface. In this way, ^{1}H → ^{27}Al CP NMR allows for determining the ^{27}Al co-ordination specifically on the particle surface.

5.3. Transmission Electron Microscopy

Microscopy is an essential sample characterization technique for nanomaterials, as it allows for direct visualization of important factors such as particle size, size distribution, and morphology. However, traditional means of microscopy, such as optical microscopy, are unable to resolve fine features at the nanoscale. This is because the resolving power of a microscope is limited by the wavelength of the source. The maximum resolution an imaging setup can achieve is:

$$d = \frac{\lambda}{2NA} = \frac{\lambda}{2n\,sin\alpha} \qquad (5.3)$$

where d is the resolution, i.e. the minimum distance between two objects which can be distinguished as two objects, and NA is the numerical aperture, which defines the range of

angles which the lens can accept, with n being the refractive index of the environment the lens is in, and α as the half-angle measured from the lens center.

Using traditional optical microscopy, the resolution is limited by the lower limit of visible light, around 400 nm. However, by exploiting the wave properties of electrons as an imaging source, it is possible to far exceed the limits of optical microscopy. The wavelength of electrons is given by the de Broglie principle:

$$\lambda = \frac{h}{p} = \frac{h}{m_e v} \tag{5.4}$$

where h is Planck's constant, and p is the electron's momentum, i.e. its mass m_e times its velocity v. Using this relationship, the wavelength of the electron is then limited by its momentum. It then becomes possible to achieve extremely high resolution for imaging by increasing the voltage of the electron beam, with modern microscopes operating at 100-300 keV and sub-Angstrom resolution.

The electron beam is generated either thermionically by heating a metal filament or by field emission, in which electrons are stripped from a sharpened filament at several keV. The optics used to adjust the beam characteristics are composed of electromagnets, which act as lenses, to focus and align the beam. Samples must be thin enough for the electron beam to pass through, typically less than several hundreds of nanometers, and an image is then formed on a detector behind the sample. Contrast is achieved by the reduction in beam intensity as the electrons interact with the matter in the sample. Several factors can affect the image contrast, for example, the electron density of the atoms in the sample, with high density materials interacting more with the beam.

Since the optics are governed by the use of electromagnets, the beam characteristics can be adjusted simply by varying the current in the solenoid. This allows the same configuration to focus the electrons to a narrow beam which can be scanned over a sample, and enables the possibility for other characterization techniques within the same apparatus. For example, scanning across the sample with a narrow beam allows for compositional analysis techniques, such as electron energy loss spectroscopy (EELS) and energy dispersive spectroscopy (EDS).

Microscopy was used in this work for imaging the nanoparticle size and size distribution, as well as compositional analysis using EELS and two dimensional EDS mapping. Samples were prepared by dropping a dilute solution of nanoparticles in ethanol onto a carbon coated copper grid, and dried under a halogen lamp.

5.4. Thermogravimetric Analysis

Thermogravimetric analysis (TGA) involves the measurement of the weight of a sample as a function of temperature. It consists of a sensitive scale to measure the weight loss of the sample in an oven. The ability to track the weight loss as a function of temperature provides valuable insights into reaction kinetics, such the temperatures at which phase transitions occur, as well as the temperatures at which materials thermally decompose. The heating rate may be constant, although it is also common to apply a predetermined heating scheme. For example, samples may be rapidly heated to 100 ºC and held for a significant amount of time in order to expel residual moisture before the temperature is increased linearly.

TGA was used in this work as a means to observe the precursor materials' behavior at temperatures around the reaction temperature. The precursor materials consist of three organic molecules bound to a central metal ion, and each organic group is cleaved off the central ion at different temperatures. The use of TGA to uncover the trends of precursor thermal decomposition provided insights into reaction kinetics, and allowed for optimization of experimental conditions.

5.5. Photoluminescence Spectroscopy

Photoluminescence spectroscopy is used to find the absorption and emission characteristics of luminescent samples. The sample is exposed to a light source at a wavelength sufficient to excite the luminescent ions, and the emitted light is passed through a spectrometer to obtain an emission spectrum. To measure the absorption spectrum, the peak emission wavelength is monitored while adjusting the excitation wavelength. Measurement of emission and absorption spectra, also referred to as photoluminescence (PL) and photoluminescence excitation (PLE) spectra were conducted in solution using a UV/VIS plate reader. Dilute solutions of nanoparticles in ethanol were placed in a 96 well plate and inserted into a Tecan M200 Infinite plate reader. The plate reader uses a xenon flash lamp as a broadband excitation source with a monochromator for wavelength selection. After interacting with the sample, the emitted light is then passed through a second monochromator before being absorbed by a silicon photodiode detector. Three acquisitions are taken for samples in ethanol, and again with just ethanol, in order to subtract out the ethanol as a background.

5.6. Photoluminescence Quantum Yield

As mentioned in Chapter 2, not every absorbed photon produces a fluorescent photon. Several non-radiative relaxation pathways may be present, such as defects in the crystal, surfaces, concentration quenching, etc. The photoluminescence quantum yield (PLQY), or internal quantum efficiency, of dried nanophosphors synthesized at 300 ºC and 315 ºC was calculated using:

$$PLQY = \frac{\phi_{emitted}}{\phi_{absorbed}} \quad (5.5)$$

where $\phi_{emitted}$ and $\phi_{absorbed}$ is the flux of the emitted and absorbed photons in s^{-1}, respectively. Photon fluxes were calculated using a 3.3" Spectralon coated integrating sphere (LabSphere) connected to a spectrometer with CCD detector (Ocean Optics 2000+) via a 600 µm diameter visible-NIR fibre optic cable with a numerical aperture of 0.22, and a 375 nm diode laser (Coherent OBIS LX) acting as the excitation source. The integrating sphere contained two 0.5" diameter ports for the laser and fibre optic connection, respectively. A calibrated tungsten halide light source (LS-1-CAL, Ocean Optics) was used to convert detected counts into a spectral irradiance $I(\lambda)$. An integration time of 100 ms was used.

The response of the integrating sphere, a unitless quantity which accounts for the reflectivity of the sphere coating, coupling to the fibre optic cable, and light lost through the sphere ports was calculated using:

$$R_s(\lambda) = \frac{A_{fibre} \cdot (1 - R) \cdot \Omega \cdot \rho}{\pi A_{sphere} \cdot [1 - \rho(1 - f)]}$$

(5.6)

Where $R_s(\lambda)$ is the sphere response, A_{fibre} is the cross-sectional area of the fibre, R is the reflectivity of the fibre face, Ω is the solid angle subtended by the fibre (approximated as $\pi \cdot (numerical\ aperture)^2$), ρ is the reflectivity of the sphere coating, A_{sphere} is the surface area of the sphere, and f is the port factor, or the ratio of areas of the ports to the sphere surface area. The sphere reflectivity was then fitted to a third order polynomial function.

Photon fluxes were then determined using:

$$\phi_{incident} = \int_0^{\infty} \frac{I_{laser}(\lambda) \cdot R_s(\lambda)^{-1}}{hc/\lambda} \cdot d\lambda$$

(5.7)

$$\phi_{reference} = \int_0^{\infty} \frac{I_{reference}(\lambda) \cdot R_s(\lambda)^{-1}}{hc/\lambda} \cdot d\lambda$$

(5.8)

$$\phi_{emitted} = \int_{390\ nm}^{710\ nm} \frac{I_{sample}(\lambda) \cdot R_s(\lambda)^{-1}}{hc/\lambda} \cdot d\lambda$$

(5.9)

$$\phi_{sample} = \int_{380\ nm}^{360\ nm} \frac{I_{sample}(\lambda) \cdot R_s(\lambda)^{-1}}{hc/\lambda} \cdot d\lambda$$

(5.10)

where $\phi_{incident}$, $\phi_{reference}$, $\phi_{emitted}$, and ϕ_{sample} are the fluxes of the laser with no sample in place, the sample holder (a low density polyethylene bag), sample emission, and scattering of the sample in the laser beam respectively. The flux of photons absorbed by the sample was determined as:

$$\phi_{absorbed} = \phi_{reference} - \phi_{sample} \tag{5.11}$$

PLQY was then calculated according to equation (1).

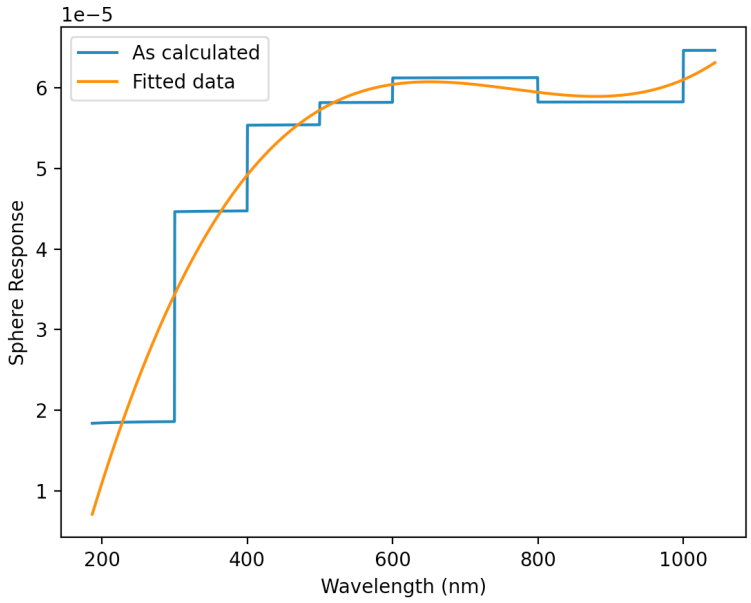

Figure 5.3:Integrating sphere spectral response.

Data fit to $f(x) = ax^3 + bx^2 + cx + d$ *with [a, b, c, d] = [3.07721257e-13, -7.06784320e-10, 5.29177847e-07, -6.90925893e-05]. Step function of sphere response was due to low resolution in sphere coating reflectivity.*

Chapter 6: Photoluminescence Enhancement of Ce:YAG Nanophosphors via Doped/intrinsic Core/Shell Nanostructures

6.1. Preface

This paper, published in the Journal of Luminescence in 2019, was the first attempt at demonstrating strategies for improving the performance of Ce:YAG nanophosphors made using the glycothermal method. The proposed strategy involved the use of a two-step, seed-mediated doped/intrinsic core/shell architecture, made in solution with no annealing step. The goal was to enhance the local crystal field of Ce ions near the particle surface with the addition of an ideal crystal field. This also had the added benefit of spatially separating the Ce ions from defects on the particle surface. The shell thickness was controlled by adding additional precursor as a ratio of the initial precursor concentration, designated as the shell-to-seed ratio, or SSR. SSRs of 0.5:1, 1:1, 1.5:1, and 2:1 were used for this study.

One aspect of note is the abnormally large average particle size and size distribution at higher SSRs. As mentioned in Chapter 3, addition of precursor after nucleation encourages growth to improve overall stability. The large particle size may also be due to the use of a Teflon liner in the reaction vessel, which reduced the working volume and would therefore increase the autogenous pressure. No signs of Teflon or other fluorocarbon species were found during sample characterization, but nonetheless the Teflon liner was not used in subsequent studies. It was found however that without the use of a liner, iron ions from the stainless steel reaction vessel would incorporate into the final product. A

glass test tube was used in subsequent studies, which eliminated the presence of iron and increased the working volume.

This article was co-authored by Aum Patel, whose contributions involved sample preparation for reproducibility and data validation, as well as performing particle size measuring and statistics as a summer student.

DOI: https://doi.org/10.1016/j.jlumin.2019.03.024

6.2. Abstract

Ce:YAG/YAG nanophosphors are synthesized using a two-step seed mediated glycothermal process. The need for the proposed process arises from the high sensitivity of Ce^{3+} to its local environment, the highly defective surfaces of nanoparticles, and increased proportion of Ce atoms near the surface due to the high ratio of surface area to volume of nanoparticles. Shell thickness was controlled by varying the molar concentration of material added during the second step of synthesis relative to the starting amount, denoted as the shell-to-seed ratio (SSR). It was found that an SSR of 1:1 yielded an average particle size of 186 ± 59 nm with a marked enhancement in photoluminescence and photostability compared to particles with no shell. EELS linescans confirm localization of the dopant to the core of the crystal.

6.3. Introduction

Since their invention, blue emitting InGaN LEDs have revolutionized the field of solid-state lighting. Highly efficient blue LEDs are combined with existing phosphors to produce low-cost, high brightness white light. $4f \rightarrow 5d$ transitions of Ce^{3+} in cerium-doped yttrium aluminum garnet (Ce:YAG) support absorption around 450 nm, and strong crystal field splitting gives rise to a broadband yellow-green emission spectrum.[6.7.1, 6.7.2] As such, Ce:YAG has become the phosphor of choice when paired with blue LEDs for solid-state white lighting. Conventionally, Ce:YAG is produced by the solid-state synthesis method involving repeated firing at elevated (>1200°C) temperatures. While wet chemical methods exist for producing Ce:YAG at lower temperatures, such as the sol-gel, co-precipitation, and spray pyrolysis methods, these techniques still require elevated

temperature heating steps to result in phase-pure YAG.[6.7.3-6.7.7] As a consequence, processing at these elevated temperatures yields an overall grain size in the 10–15 μm range. With the display community ever in pursuit of pixel size reduction, these large grain sizes become incompatible with micro-LEDs and GaN nanowire based devices due to optical crosstalk. Nanosizing Ce:YAG is an attractive solution, as it allows for smaller packaged devices with much higher packing density.

Luminescence of Ce:YAG is highly sensitive to the surrounding crystal field[6.7.8, 6.7.9]. The optically active trivalent state of Ce can be protected in the crystal's interior, but surface Ce atoms can experience quenching due to the abrupt termination of the crystal field in addition to being prone to oxidative degradation to the optically inactive Ce^{4+} state. This issue is compounded on the nanoscale due the much higher ratio of nanoparticle surface area to volume.

Heat treatments of Ce:YAG nanopowders are often necessary to induce crystallization and promote Ce diffusion into the crystal's interior to improve photoluminescence and photostability.[6.7.10-6.7.12] As mentioned above, this approach can lead to irreversible aggregation and sintering resulting in large grain sizes. The glycothermal method, in which Y, Al, and Ce alkoxide precursors undergo reaction in a glycol solvent under elevated pressure, has been shown to produce crystalline Ce:YAG nanoparticles with a high degree of uniformity and monodispersity.[6.7.13-6.7.15] A moderate improvement in photoluminescence has been seen with the addition of polyethylene glycol (PEG) to the glycol solvent due to passivation of surface Ce ions, and multiple cycles of glycothermal treatment have been examined in an effort to improve the crystal structure and thereby

photostability.[6.7.16, 6.7.17] Another technique to improve the surface quality involves the use of core/shell architectures, often employed to mitigate surface defects in nanoparticles and quantum dots.[6.7.18, 6.7.19] In the case of Ce:YAG nanophosphors, this has generally been accomplished by the deposition of yttrium and cerium precursors on spherical aluminum hydroxide or oxide template nanostructures, which, after heat treatment, yield hollow Ce:YAG nanoparticles or Al_2O_3/Ce:YAG core/shell nanostructures, respectively.[6.7.20, 6.7.21]

Although the addition of PEG for surface passivation of Ce and multiple heating cycles have improved photoluminescence and photostability respectively, the approaches mentioned above do not address the underlying issue of surface Ce ions experiencing an abrupt termination of the local crystal field. In this work, the effect of extending the crystal field by means of doped/intrinsic core/shell nanostructures is examined. A two-step glycothermal method is proposed in order to enhance photoluminescence output of Ce:YAG nanoparticles using a seed-mediated growth technique.

6.4. Experimental

6.4.1. Synthesis of Ce:YAG nanoparticles

Ce:YAG nanoparticles with 1 mol% doping were synthesized by the methods outlined by Nyman et al.[6.7.14] The reaction consists of homogenizing 1.47 mmol yttrium acetate, 2.45 mmol aluminum acetate, and 0.016 mmol cerium acetate in 10 mL of 1,4 butanediol. All products were purchased from Sigma Aldrich without further purification. The reactants were then sealed in a teflon-lined stainless steel

autoclave with a working volume of 24.7 mL and heated to 300 °C at a rate of ~ 3 °C/minute over 90 min, and held for 3 h. Stirring at 300 rpm was achieved with a magnetic stirring plate after placing a teflon-coated stir-bar into the reaction chamber. Once the reaction was completed, the Ce:YAG nanopowder was washed three times in ethanol by successive centrifugation at 15 000 rpm before drying for 12 h at 80 °C.

6.4.2. Synthesis of Ce:YAG/YAG core/shell nanoparticles

For doped/intrinsic core/shell nanostructures, the procedure outlined above was undertaken with additional yttrium acetate and aluminum isopropoxide added to the reaction chamber after the initial reaction outlined above. The material added back to the reaction chamber was taken as a molar ratio to the initial material, denoted the shell-to-seed ratio (SSR), which varied from 0.5 to 2:1 of shell material to core material. For example, adding back half of the initial material to the reaction chamber was denoted 0.5:1 SSR. The process is shown schematically in Figure 6.1.

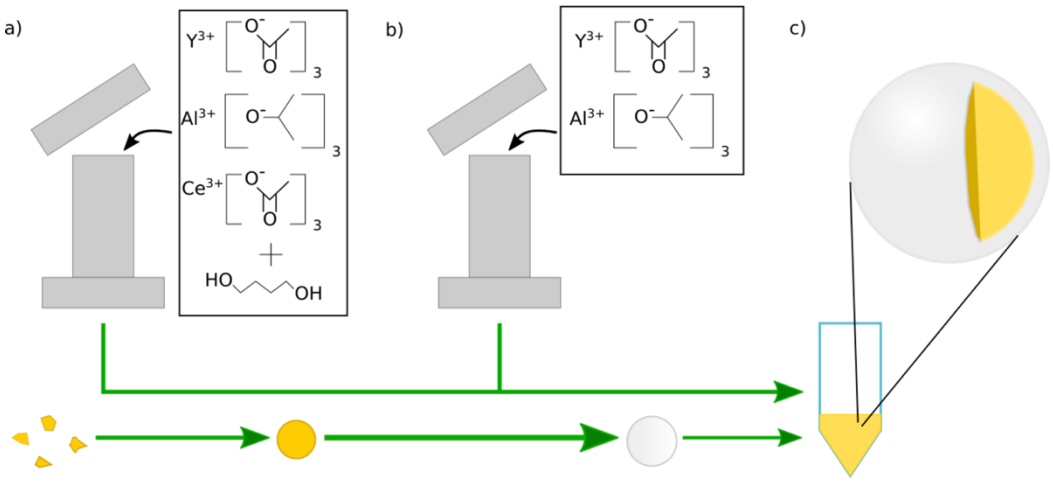

Figure 6.1: Schematic of the core/shell growth process.

a) Yttrium, aluminum, and cerium alkoxides are combined in 1,4 BD solvent. b) After reaction, Y and Al precursors are added back to the reaction chamber. c) Synthesized nanoparticles are washed by centrifugation.

6.4.3. Characterization

Core and core/shell particles were imaged using a transmission electron microscope (TEM, Phillips CM12) operating at 120 kV. Average particle size was determined from TEM images using ImageJ software. X-ray powder diffraction (XRD) measurements were carried out at room temperature with a BRUKER D8 Discover equipped with DeVinci.Design diffractometer and Co Kα source (λ_{avg} = 1.79026 Å) operated at 35 keV

and 45 mA for phase confirmation. Co-ordination of aluminum sites was measured using a BRUKER AV 500 high resolution solid-state ^{27}Al single pulse excitation nuclear magnetic resonance (SPE-NMR) spectrometer with 11.7 T static field strength. Magic angle spinning (MAS) at 20 kHz was used with a 2.5 mm zirconia rotor. $^{1}H \rightarrow {}^{27}Al$ cross polarization (CP) MAS NMR spectra were measured in the same apparatus with a contact time of 500 µs. The Al chemical shift was referenced to $Al(NO_3)_3$ dissolved in deuterium oxide. Operating frequencies were 130.3 MHz and 500.25 MHz for ^{27}Al and ^{1}H, respectively. A pulse width of 4 µs was used in all tests. Photoluminescence (PL) and photoluminescence excitation (PLE) were measured in a Tecan Infinite M200 Pro spectrometer by preparing 10 mg/mL solutions of dried nanoparticles in ethanol. These samples were then dried in order to test their photostability. The samples were exposed to 450 nm light for 10 000 s, monitoring the emission at 530 nm every 15 s in a Tecan Infinite M200 Pro spectrometer. Photostability of synthesized nanopowders was compared to commercially available bulk Ce:YAG powder (Phosphor Technology Ltd, UK). Ce dopant localization was determined using electron energy loss spectroscopy (EELS) linescans on a JEOL 2010F TEM operated at 200 kV in STEM mode with high angle annular dark field (HAADF) imaging.

6.5. Results and Discussion

6.5.1. X-Ray Diffraction

XRD results (Figure 6.2) revealed the YAG phase for all conditions, referenced to ICDD PDF # 0030-040. A minor boehmite phase is present, as is occasionally observed in

glycothermal YAG synthesis (ICDD PDF # 021-1307).[6.7.11, 6.7.14, 6.7.22] The characteristic YAG (420) peak near 38° shifts slightly towards the reference position with increasing shell thickness, as the crystals would have a higher overall proportion of intrinsic material.

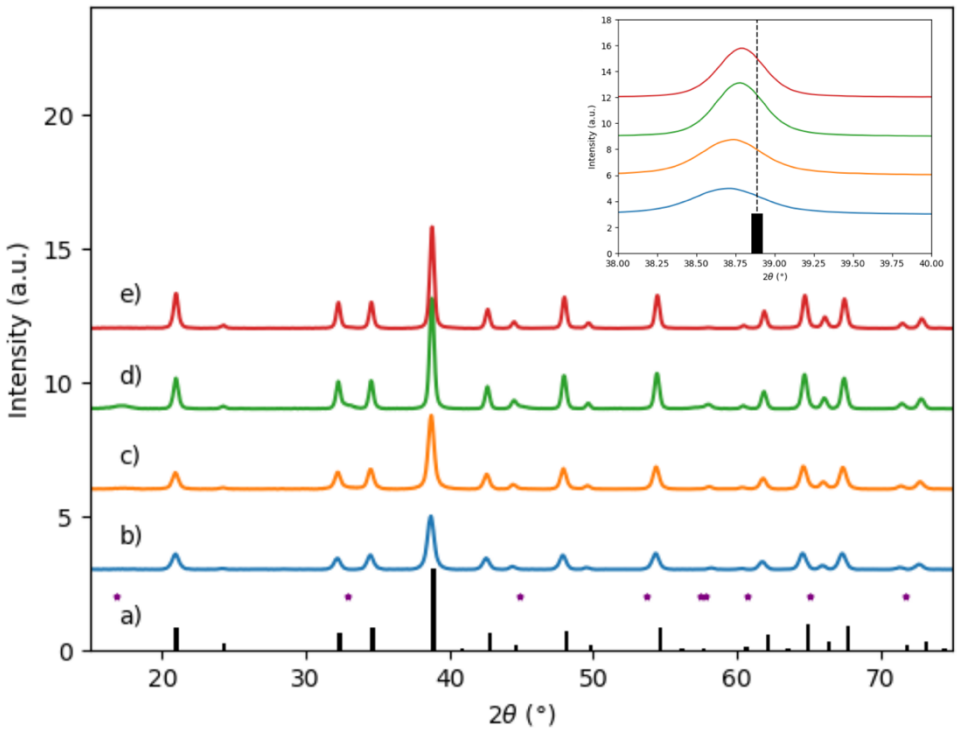

Figure 6.2: XRD of Ce:YAG nanoparticles with varying shell thickness.
a) YAG reference spectrum, ICDD PDF # 0030-040. Purple asterisks indicate the 2θ position of a boehmite phase. Shown are samples with a SSR of b) 0:1, c) 0.5:1, d) 1:1, and e) 2:1. Inset: Close-up of the (420) plane around 38°.

6.5.2. Transmission Electron Microscopy

TEM images of obtained Ce:YAG nanoparticles show an increase in average particle size proportional to the amount of shell material added back to the reaction chamber. With no shell material added, the particles consisted of primary particles 10 ±

2 nm in size, which coalesced into particles with an average size of 41 ± 7 nm (Figure 6.3a), consistent with other works.[6.7.13, 6.7.14] Upon addition of shell material, the particles grew to 53 ± 13 nm, 186 ± 59 nm, and 256 ± 100 nm for SSRs of 0.5:1, 1:1, and 2:1, respectively. It was observed that an SSR of 0.5:1 was insufficient to form uniform shell structures (Figure 6.3b). The shell material instead formed primary particles which then aggregated on the doped core particle surface. At an SSR of 1:1, uniform, conformal shells of ~10 nm thickness could be seen. Shell thickness increased to ~20 nm at an SSR of 2:1.

a)

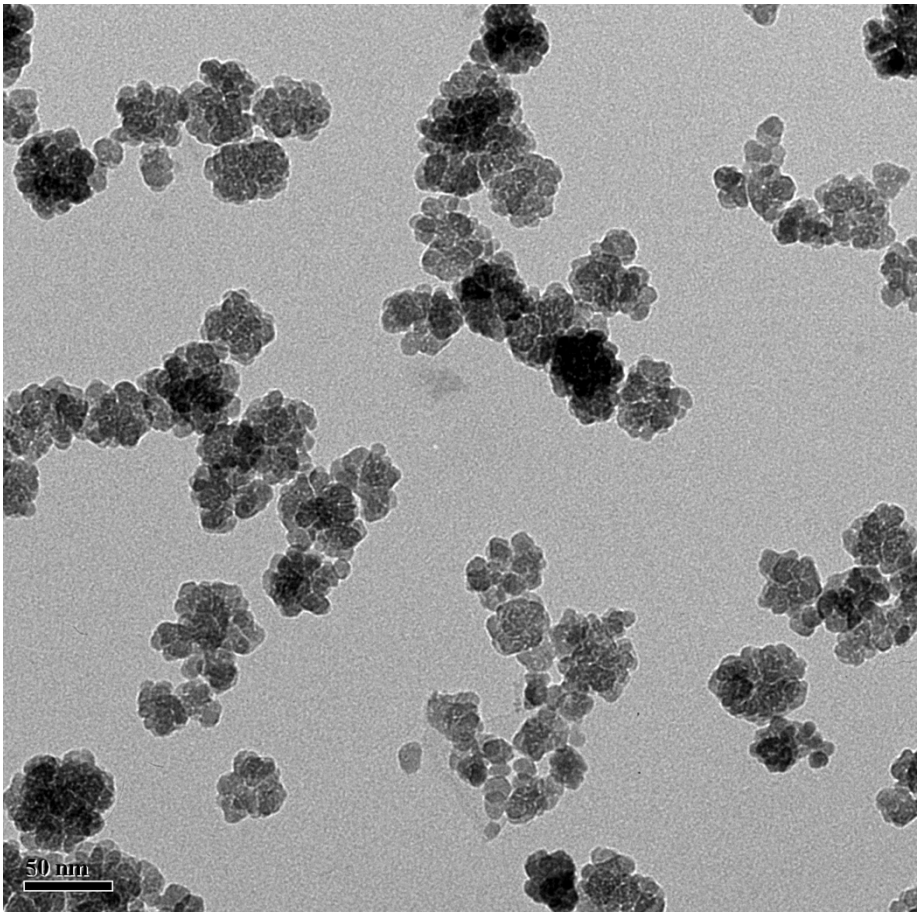

b)

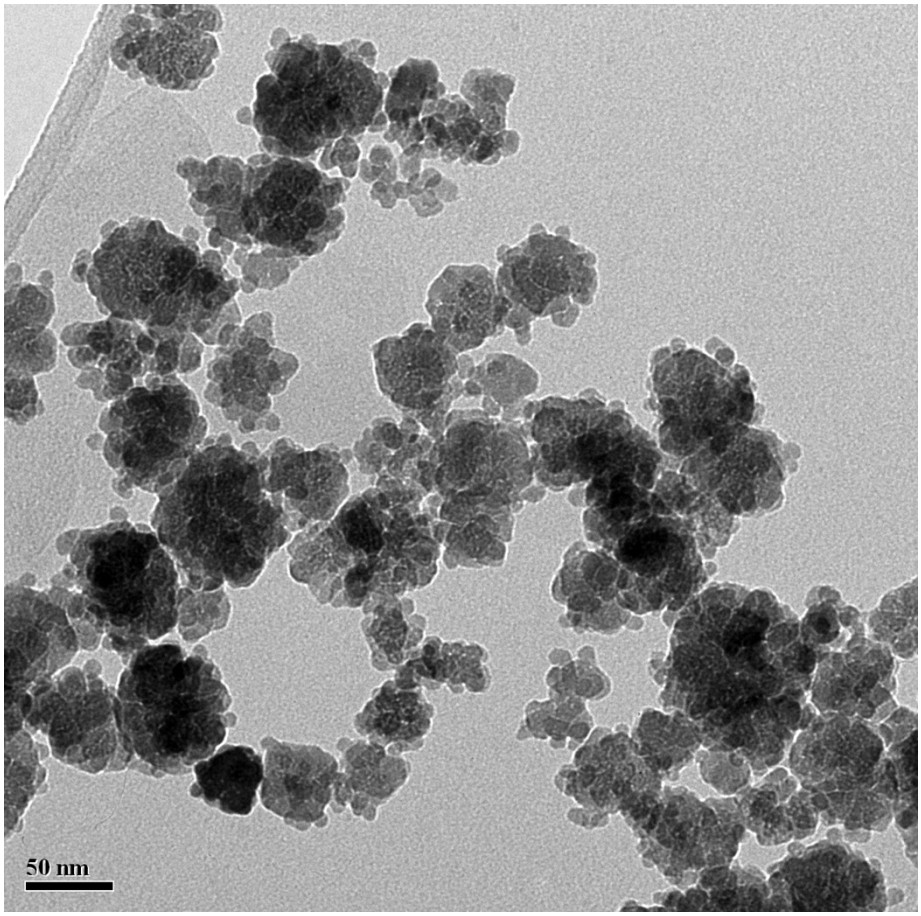

c)

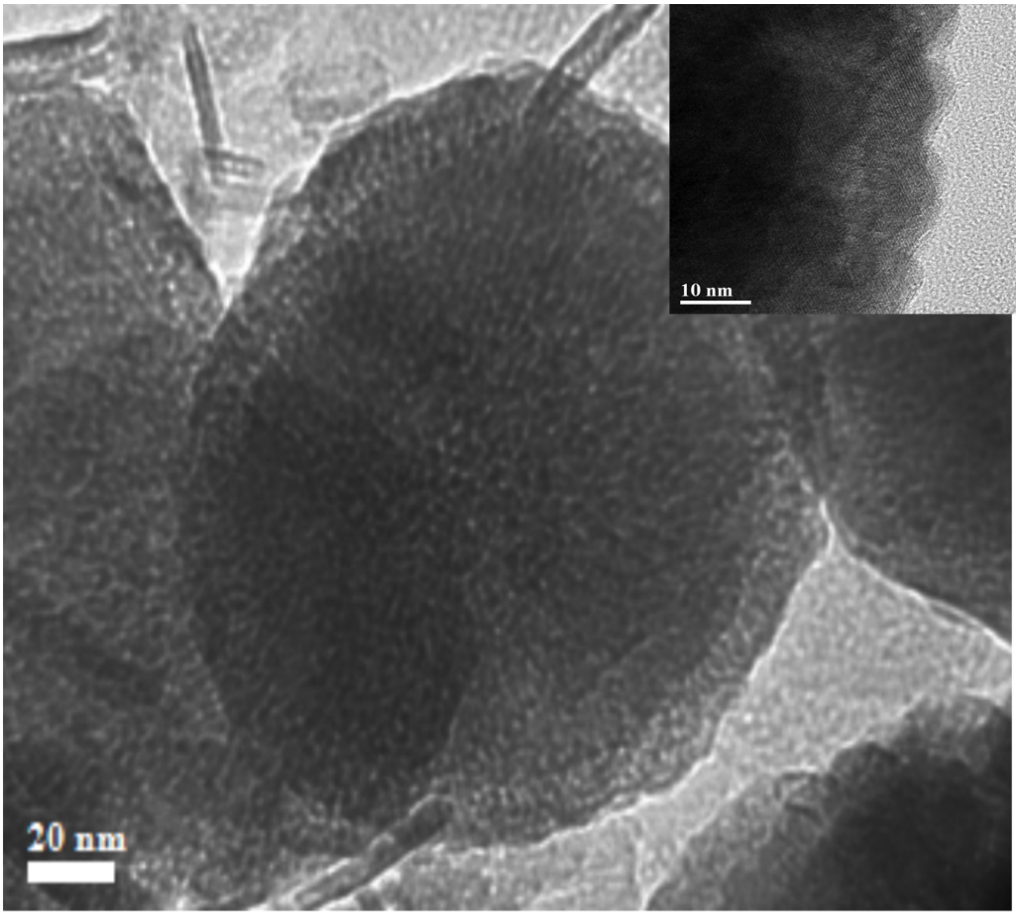

d)

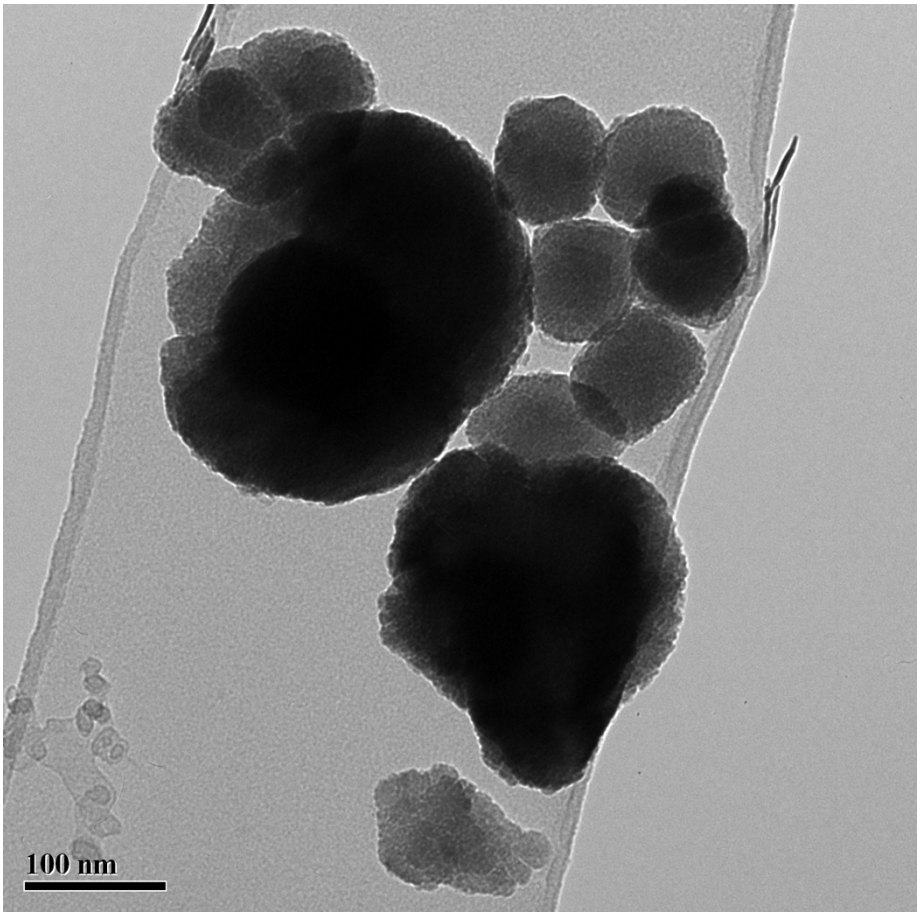

Figure 6.3: TEM images of Ce:YAG nanoparticles with varying shell-to-seed ratios. Shell-to-seed ratios: a) 0:1, 3b) 0.5:1, 3c) 1:1, and 3d) 2:1. Inset of 3c) depicts an HRTEM image of the core/shell interface.

High resolution TEM of a Ce:YAG nanoparticle with SSR of 1:1 (Figure 6.3c, inset) shows conformal, epitaxial growth of a shell structure with thickness of ~10 nm. In order to confirm a doped/intrinsic core/shell structure, EELS linescans were undertaken to verify Ce dopant localization to the interior of the crystal. A scan was performed on a

nanoparticle with an SSR of 0.5:1, and although the shell quality was found to be generally poor, it was found that particle sizes greater than ∼50 nm were large enough to induce broadening of the STEM beam, reducing linescan resolution. Onset of the Ce signal only appeared ∼5–8 nm after the onset of Y, consistent with a doped/intrinsic core/shell structure (Figure 6.4).

a)

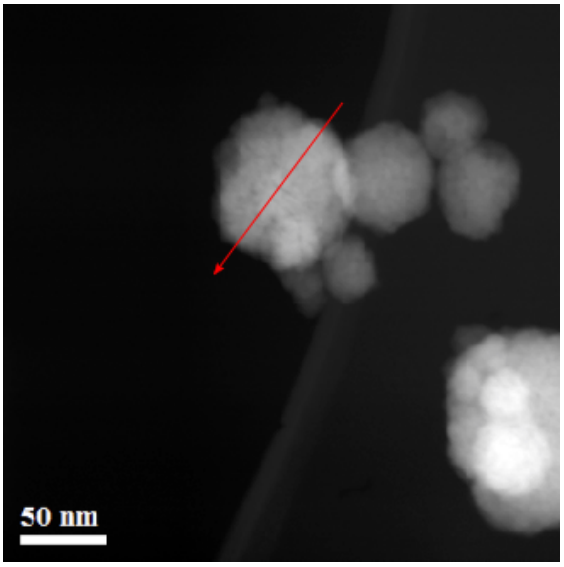

b)

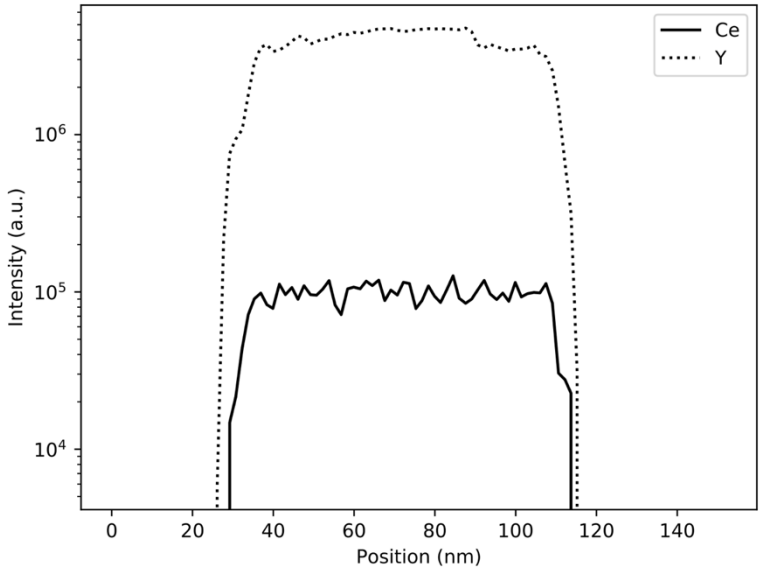

Figure 6.4: Localization of Ce dopant in core/shell YAG.

a) STEM image of a Ce:YAG nanoparticle with an SSR of 0.5:1. Red arrow depicts direction of EELS linescan. b) EELS linescan depicting the spatial distribution of Y and Ce.

6.5.3. Nuclear Magnetic Resonance

NMR was used to probe the co-ordination of aluminum atoms in the YAG crystal. In YAG, aluminum can bond to either 4 or 6 oxygen atoms resulting in tetrahedral and octahedral co-ordination, respectively.[6.7.23] The ratio of tetrahedral to octahedral sites in bulk YAG is 3:2, however the spherical morphology of nanoparticles inherently causes defects in the cubic garnet YAG structure, particularly on the surface. Figure 6.5a shows single pulse excitation (SPE) to probe the co-ordination of ^{27}Al in the crystal. Peaks close to 0 ppm are assigned to octahedral co-ordination, while peaks around 65 ppm are assigned to tetrahedral co-ordination. It was found that for SSRs of 0:1, 0.5:1, and 1:1 the ratio of ^{IV}Al/^{VI}Al was 0.154, 0.183, and 0.162, respectively. It was observed and has been reported in other works that Al in YAG exists mostly in the octahedral configuration when synthesized by the glycothermal method.[6.7.11, 6.7.13, 6.7.16] The unusually low ratio of ^{IV}Al/^{VI}Al found in this study may have been caused by extended reaction time. It has been reported elsewhere that under glycothermal reaction conditions, Al atoms are able to diffuse until maximum co-ordination is reached.[6.7.24] The reaction time was extended from the usual 2 h to 3 in this study, as the primary objective was the enhancement of photoluminescence intensity over reduced particle size. This additional hour of reaction time may have allowed Al atoms to diffuse further, maximizing their co-ordination.

a)

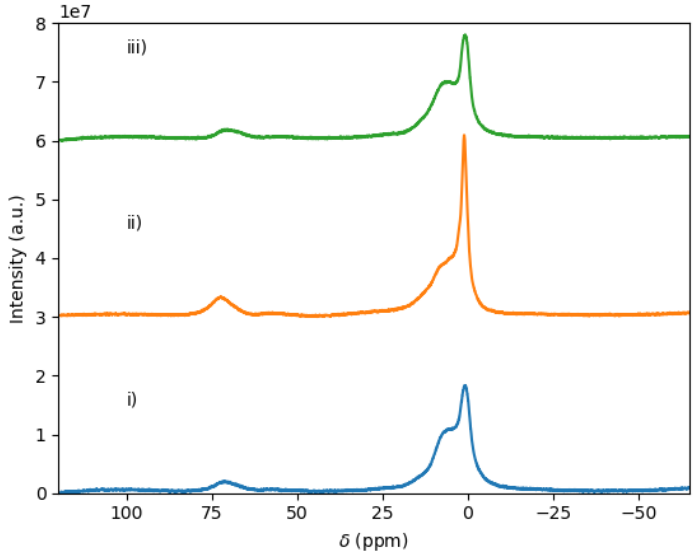

b)

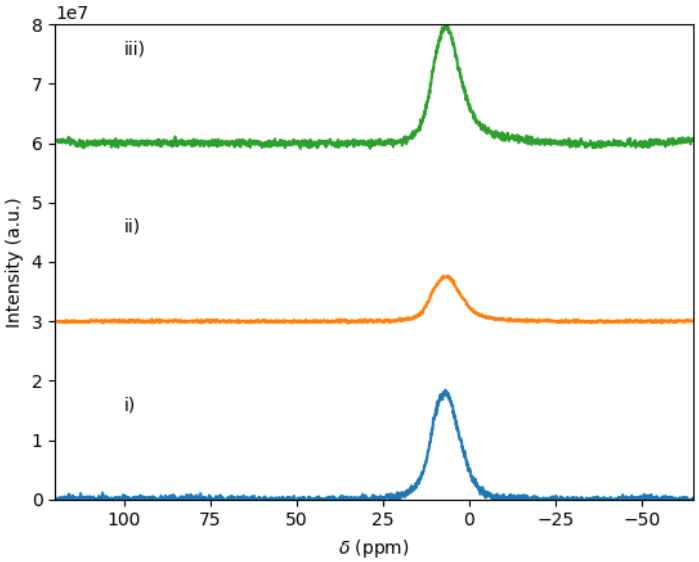

Figure 6.5: ^{27}Al MAS NMR of Ce:YAG nanoparticles.

a) SPE NMR of ^{27}Al in YAG. b) $^{1}H \rightarrow ^{27}Al$ CP NMR. i) SSR = 0:1, ii) SSR = 0.5:1, iii) SSR = 1:1.

Figure 6.5b shows samples probed with $^{1}H \rightarrow {}^{27}Al$ cross polarization (CP) NMR. In this case, the only H atoms present in the samples would be associated with organic molecules adsorbed to the particles' surface. Cross polarization with an appropriately short contact time therefore enables probing the co-ordination of Al near the surface of the crystal. In all cases, only a signal from octahedral Al co-ordination was detected, indicating that tetrahedral Al co-ordination is not present at the particle surface. The relatively low signal intensity in the case of an SSR of 0.5:1 (Figure 6.5b ii) indicates especially poor crystal quality at the particle surface, consistent with Figure 6.3b, in which there was not sufficient shell material to form uniform shells.

NMR shows a non-ideal crystal structure in all cases, particularly on the particle surface. However, if the particles are synthesized with no shell, these defects are in close proximity to surface Ce ions. Growth of a shell therefore allows for physical separation between Ce activator atoms and the highly defective particle surface.

6.5.4. Photoluminescence and Photostability

Luminescence of samples with varying shell thicknesses were tested for their optical properties. It was found that the presence of a passivating shell promoted higher photoluminescence and photoluminuminece excitation intensity, as observed in other rare earth doped core/shell nanoparticle configurations.[6.7.25, 6.7.26] Absorption and emission intensity increased with increasing shell thickness until an SSR of 1:1 was reached, shown in Figure 6.6. At an SSR of 2:1, the luminescence intensity dropped, possibly due to dilution of the Ce concentration in the overall crystal, i.e. the reduction of Ce concentration

per unit volume of nanoparticle due to the addition of undoped material. Luminescence of the Ce ion is derived from 5d ($^2D_{3/2}$) → 4f ($^2F_{5/2}$,$^2F_{7/2}$) transitions, and participation of the *d* orbital makes Ce extremely dependent on the crystal potential imposed by the surrounding lattice.[6.7.8, 6.7.9] In bulk, the luminescent trivalent state of Ce dopant ions are protected in the crystal's interior. However, since nanoparticles have a much greater surface area compared to their volume, the probability of Ce existing near the crystal's surface is high. This issue is two-fold: the Ce ions on the surface experience an abrupt termination of the crystal field, and the potential exists for oxidation to the non-radiative Ce^{4+} state, both of which can contribute to reduced luminescence.

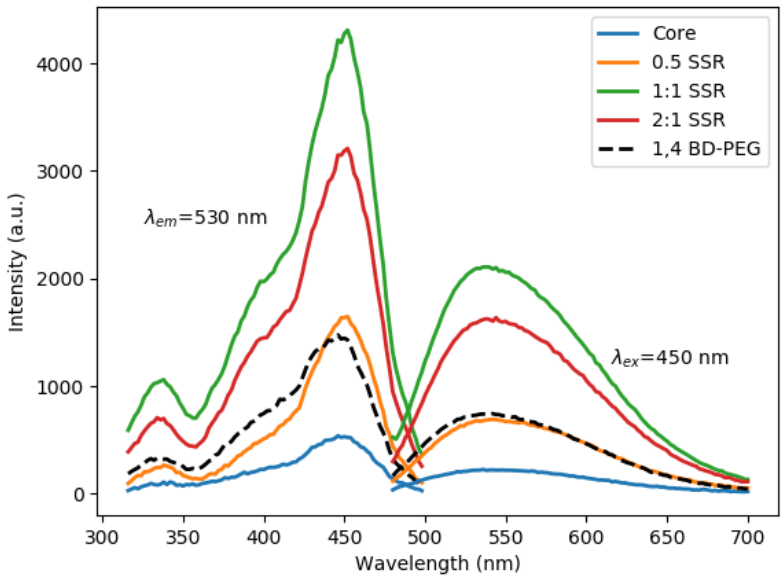

Figure 6.6: Absorption and emission properties of Ce:YAG nanoparticles with shell-to-seed ratios varying from 0:1 to 2:1.

The dashed line indicates Ce:YAG synthesized with a polyethelyne glycol (PEG) co-solvent.

Other works have used polyethylene glycol (PEG) as a co-solvent in order to tie up oxygen vacancies on the crystal surface, which was shown to passivate the surface Ce ions as well.[6.7.16] This method of stabilizing the particle surface with organic molecules was carried out in the current study in order to compare the two approaches. The procedure above was repeated with the addition of PEG (M_w = 200 g/mol) in a 1:1 vol ratio as a co-solvent, as outlined by Kasuya et al. The total volume of solvent was kept constant at 10 mL. As can be seen by the dashed line in Figure 6.6, this approach does show an improvement in luminescence over particles prepared without PEG addition, however the improvement is comparable to that of particles prepared with an SSR of 0.5:1. This approach can help reduce the density of oxygen vacancies on the surface, but does not address the underlying issue of abrupt termination of the crystal, which is critical due to Ce sensitivity to the local environment. Growth of an intrinsic shell offers the opportunity to both tie up oxygen vacancies and extend the crystal field experienced by surface Ce atoms.

Photostability of samples with an SSR of 0:1 (core only) and 1:1 are shown in Figure 6.7. It can be seen that after 10 000 s, the photoluminescence intensity of the core only particles drops to almost half of its initial value, while those with a passivating shell have stabilized at around 80%. Figure 6.7c shows the performance of bulk, micron-sized Ce:YAG, which remains highly photostable over 10 000 s. Further research into improving the performance and stability of Ce:YAG nanopowders remains active.

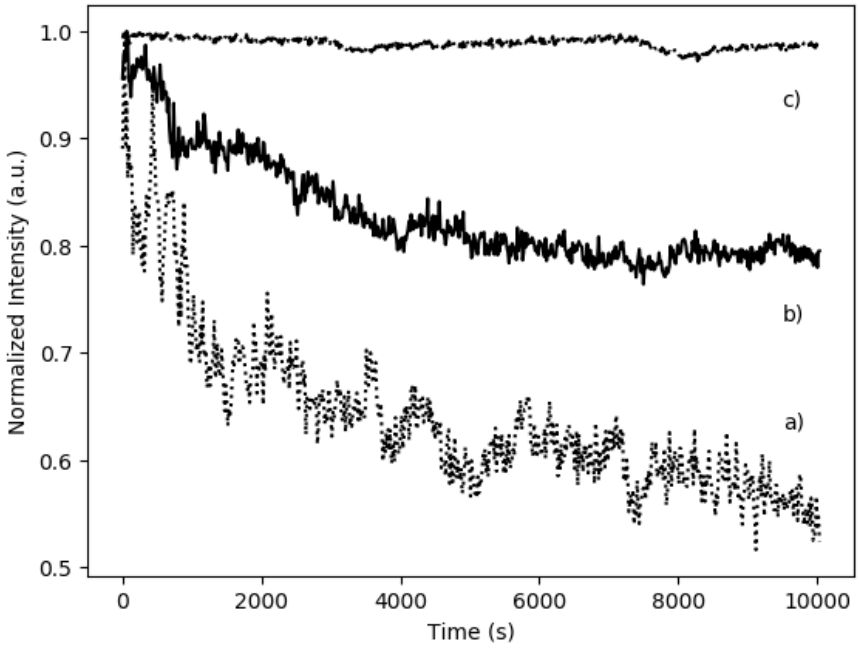

Figure 6.7: Photostability of Ce:YAG nanoparticles.

a) Core only. b) Ce:YAG nanoparticles with an SSR of 1:1. c) Commercially available bulk Ce:YAG.

6.6. Conclusion

A method of enhancing luminescence of Ce:YAG nanoparticles is proposed, involving a two-step seed mediated glycothermal process to form doped/intrinsic core/shell particles. This method aims to enhance luminescence by protecting the defect-sensitive Ce ions from the defect-rich nanoparticle surface using an intrinsic YAG crystal. This work has demonstrated the need for such an approach, as NMR data suggests a high proportion of defects, particularly on the particle surface, as well as an improvement in luminescence using various shell thicknesses, denoted as a shell-to-seed ratio (SSR). An SSR of 1:1 yielded the most enhancement, and was found to be more photostable under 450 nm

illumination compared to nanophosphors with no shell. It was also shown that Ce atoms remain localized to the core, presenting the possibility for shell doping with other luminescent lanthanides.

6.7. References

6.7.1 S. Shionoya and WM Yen. Phosphor Handbook, 1999.

6.7.2 Robert Withnall and Jack Silver. Physics of Light Emission from Rare Earth-Doped Phosphors. *Handbook of Visual Display Technology*, pages 1567–1576, 2016.

6.7.3 Michael Veith, Sanjay Mathur, Aivaras Kareiva, Mohammad Jilavi, Michael Zimmer, and Volker Huch. *Low temperature synthesis of nanocrystalline $Y_3Al_5O_{12}$ (YAG) and Ce-doped $Y_3Al_5O_{12}$ via different sol–gel methods*. Journal of Materials Chemistry, 9(12):3069–3079, 1999.

6.7.4 Xing-Huang Yan, Song-Sheng Zheng, Rui-Min Yu, Cai Jing, Zhi-Wei Xu, Chun-Jia Liu, and Xue-Tao Luo. Preparation of YAG:Ce^{3+} phosphor by sol-gel low temperature combustion method and its luminescent properties. *Transactions of Nonferrous Metals Society of China*, 18(3):648–653, 2008.

6.7.5 Xianxue Li and Wenju Wang. Preparation of uniformly dispersed YAG ultrafine powders by co-precipitation method with SDS treatment. *Powder Technology*, 196(1):26–29, 2009.

6.7.6 Guogang Xu, Xudong Zhang, Wen He, Hong Liu, Hong Li, and Robert I Boughton. Preparation of highly dispersed YAG nano-sized powder by co-precipitation method. *Materials Letters*, 60(7):962–965, 2006.

6.7.7 Yun Chan Kang, I Wuled Lenggoro, Seung Bin Park, and Kikuo Okuyama. YAG:Ce phosphor particles prepared by ultrasonic spray pyrolysis. *Materials Research Bulletin*, 35(5):789–798, 2000.

6.7.8 Xiaowu He, Xiaofang Liu, Rongfeng Li, Bai Yang, Kaili Yu, Min Zeng, and Ronghai Yu. Effects of local structure of Ce^{3+} ions on luminescent properties of $Y_3Al_5O_{12}$:Ce nanoparticles. *Scientific reports*, 6:22238, 2016.

6.7.9 Nathan C George, Andrew J Pell, Geraldine Dantelle, Katharine Page, Anna Llobet, M Balasubramanian, Guido Pintacuda, Bradley F Chmelka, and Ram Seshadri. Local environments of dilute activator ions in the solid-state lighting phosphor $Y_{3-x}Ce_xAl_5O_{12}$. *Chemistry of Materials*, 25(20):3979–3995, 2013.

6.7.10 Qiang Li, Lian Gao, and Dongsheng Yan. The crystal structure and spectra of nanoscale YAG:Ce^{3+}. *Materials chemistry and physics*, 64(1):41– 44, 2000.

6.7.11 Amelie Revaux, Geraldine Dantelle, Nathan George, Ram Seshadri, Thierry Gacoin, and Jean-Pierre Boilot. A protected annealing strategy to enhanced light emission and photostability of YAG:Ce nanoparticle-based films. *Nanoscale*, 3(5):2015–2022, 2011.

6.7.12 Samuel Peter, Paul Kuyanov, Nebile Isik Goktas, Ray LaPierre, and Adrian Kitai. Microstructure development and photoluminescence of annealed nanosized Ce:YAG/Al_2O_3 and Ce:YAG/Cr:Al_2O_3 powder composites. *Materials Research Express*, 5(3):036207, 2018.

6.7.13 R Kasuya, Tetsuhiko Isobe, and H Kuma. Glycothermal synthesis and photoluminescence of YAG: Ce^{3+} nanophosphors. *Journal of alloys and compounds*, 408:820–823, 2006.

6.7.14 May Nyman, Lauren E Shea-Rohwer, James E Martin, and Paula Provencio. Nano-YAG:Ce mechanisms of growth and epoxy-encapsulation. *Chemistry of Materials*, 21(8):1536–1542, 2009.

6.7.15 M Odziomek, F Chaput, F Lerouge, M Sitarz, and S Parola. Highly luminescent YAG:Ce ultra-small nanocrystals, from stable dispersions to thin films. *Journal of Materials Chemistry C*, 5(47):12561–12570, 2017.

6.7.16 Ryo Kasuya, Tetsuhiko Isobe, Hitoshi Kuma, and Junichi Katano. Photoluminescence enhancement of PEG-modified YAG:Ce^{3+} nanocrystal phosphor prepared by glycothermal method. *The Journal of Physical Chemistry B*, 109(47):22126–22130, 2005.

6.7.17 Yusuke Kamiyama, Takehiko Hiroshima, Tetsuhiko Isobe, Toru Koizuka, and Suguru Takashima. Photostability of YAG:Ce^{3+} nanophosphors synthesized by glycothermal method. *Journal of The Electrochemical Society*, 157(5):J149–J154, 2010.

6.7.18 Jaehoon Lim, Wan Ki Bae, Donggu Lee, Min Ki Nam, Joohyun Jung, Changhee Lee, Kookheon Char, and Seonghoon Lee. InP@ZnSeS, core@composition gradient shell quantum dots with enhanced stability. *Chemistry of Materials*, 23(20):4459–4463, 2011.

6.7.19 Andrew B Greytak, Peter M Allen, Wenhao Liu, Jing Zhao, Elizabeth R Young, Zoran Popovic, Brian J Walker, Daniel G Nocera, and Moungi G Bawendi. Alternating layer addition approach to CdSe/CdS core/shell quantum dots with near-unity quantum yield and high on-time fractions. *Chemical science*, 3(6):2028–2034, 2012.

6.7.20 Min Jeong Kim, Jong Hoon Park, Keel Yong Lee, Sangwook Lee, Gill- Sang Han, Hee Jo Song, Hyunjung Shin, Tae Kyu Ahn, and Hyun Suk Jung. Cerium-doped yttrium aluminum garnet hollow shell phosphors synthesized via the Kirkendall effect. *ACS applied materials & interfaces*, 6(2):1145–1151, 2014.

6.7.21 Guo Feng, Weihui Jiang, Jianmin Liu, Cong Li, Quan Zhang, Lifeng Miao, and Qian Wu. Synthesis and luminescence properties of Al_2O_3@YAG:Ce core–shell yellow phosphor for white LED application. *Ceramics International*, 44(7):8435–8439, 2018.

6.7.22 Masashi Inoue, Hiroyuki Otsu, Hiroshi Kominami, and Tomoyuki Inui. Synthesis of yttrium aluminum garnet by the glycothermal method. *Journal of the American Ceramic Society*, 74(6):1452–1454, 1991.

6.7.23 D Massiot, C Bessada, JP Coutures, and Francis Taulelle. A quantitative study of ^{27}Al MAS NMR in crystalline YAG. *Journal of Magnetic Resonance* (1969), 90(2):231–242, 1990.

6.7.24 Prabhu Ramanujam, Bala Vaidhyanathan, JGP Binner, Shaghayegh Ghanizadeh, and Chris Spacie. Solvothermal nanoYAG synthesis: Mechanism and particle growth kinetics. *The Journal of Supercritical Fluids*, 107:433–440, 2016.

6.7.25 Jeehae Shin, Youngsun Kim, Jiyeon Lee, Sehoon Kim, and Ho Seong Jang. Highly Bright and Photostable Li(Gd,Y)F_4:Yb,Er/$LiGdF_4$ Core/Shell Upconversion Nanophosphors for Bioimaging Applications. *Particle & Particle Systems Characterization*, 34(1):1600183, 2017.

6.7.26 Dinh Xuan Loc, Tran Thi Kim Chi, Tran Thu Huong, Nguyen Vu, Tran Kim Anh, Wieslaw Strek, et al. Synthesis and characterization of core/shell structured nanophosphors $CePO_4$:Tb@LaPO4 by solvothermal method. *Journal of Rare Earths*, 29(12):1147–1151, 2011.

Chapter 7: Glycothermal synthesis and photoluminescence of Mg-Si modified Ce:YAG nanophosphors

7.1. Preface

This study aimed to determine if the optical properties of glycothermally synthesized Ce:YAG nanophosphors could be modified by the addition of Mg-Si pairs. The real novelty of this work lies in the study of precursor kinetics via thermogravimetric analysis. The typical reaction temperature for the glycothermal method is 300 ºC, however, it was found that the precursors used in the glycothermal synthesis of Ce:YAG fully thermally decompose at temperatures above 300 ºC, and performing the glycothermal reaction at slightly higher temperatures would allow for the precursors to be more homogeneously incorporated in the final product. A post-synthesis surface functionalization route was proposed to extend the functionality of the glycothermally synthesized Ce:YAG nanoparticles.

This work, and the work in the subsequent chapter, contains a calculation of the crystallite size using refinement of the XRD data, as well as a measurement of the internal quantum efficiency. The discrepancy between the crystallite size calculation and the measured particle size from TEM images arises from the inaccuracy of fitting low angle XRD data. Additionally, the internal quantum efficiency data was collected as an acquisition of three runs that were automatically averaged. As such, it was not possible to perform an uncertainty analysis on the measurement, and in the future, it is advised to take separate measurements and calculate the average manually. In addition, scattering of the

powder sample was not considered, however ideally a non-luminescent material of similar size should be used as a baseline.

This research was published in March 2021 in the Royal Society of Chemistry's *Nanoscale Advances*. The article was co-authored with Maureen Fitzpatrick, whose contributions included the data acquisition and Rietveld refinement modelling of XRD results.

DOI: 10.1039/D1NA00060H

7.2. Abstract

The absorption spectrum of Ce in a YAG based host grown using the glycothermal method was modified using the addition of Mg-Si pairs. Photoluminescence intensity was dramatically improved by increasing the reaction temperature to 315 ºC instead of the conventionally used 300 ºC. It was found that Mg acetate and tetraethylorthosilicate (TEOS) are suitable as precursors for the glycothermal process, as EDS elemental mapping showed their homogeneous inclusion in the final product. Their addition only slightly modified the emission spectrum of Ce:YAG. It was found that increasing the reaction temperature to 315 ºC yielded nanoparticles 56 ± 16 nm in size with a 3.3x enhancement in absorption and 3.7x enhancement in emission intensities compared to samples synthesized at 300ºC, and an increase in photoluminescence quantum yield from 31.8% to 48.2%. Reaction kinetics of the precursors and a proposed route for post-synthesis surface functionalization are discussed.

7.3. Introduction

Oxidative degradation and lack of stability of OLEDs and QD materials and devices continues to be an issue for their long term use, especially in high brightness applications.[7.7.1-7.7.3] Oxide phosphor materials continue to be important fluorescent materials in more robust inorganic LED devices. This article presents an alternative material system allowing for spectral tuning in well-known cerium-doped yttrium aluminum garnet nanophosphors (Ce:YAG).

Ce:YAG has been the workhorse of the solid state light community for the past several decades, as its absorption in blue and broadband yellow-green emission pair quite well with blue emitting InGaN LEDs to produce white light.[7.7.4-7.7.6] In addition, as an oxide material, it is relatively immune to oxidative degradation, and is both thermally stable and chemically inert. YAG, or $Y_3Al_5O_{12}$, as a host material crystallizes in the Ia-3d space group, consisting of the yttrium atoms dodecahedrally coordinated to 8 oxygen atoms, and 5 aluminum atoms, 3 of which are tetrahedrally coordinated to 4 oxygen atoms, leaving the remaining 2 Al atoms octahedrally coordinated to 6 oxygen atoms.[7.7.7] The Y site can accommodate large rare earth dopants such as Ce, which act as the luminescent centers in the YAG host.[7.7.8] Luminescence of Ce originates from the allowed $5d \rightarrow 4f$ transition, and as such, is not shielded by outer shell electrons and is therefore highly dependent on the local crystal field.[7.7.9] Ce in the Y site of YAG experiences a strong ligand field imposed by 8 electron rich O atoms, which splits the degeneracy of the 5*d* excited state orbital to the point where electronic transitions are achievable with photons in the visible range.[7.7.9]

Ce:YAG has several drawbacks which limit or prevent its use in next generation lighting and display applications, mainly due to its particle size and its lack of a red component in the emission profile. The most common synthesis route involves repeated grinding and firing of Ce, Y, and Al oxides at temperatures above 1400ºC.[7.7.10-7.7.12] These temperatures inevitably promote sintering and grain growth, leading to powders in the 10 μm size range. In microLED display applications, for example, the size of the phosphor

powder is comparable to that of the subpixel, which can introduce optical crosstalk and excessive luminance variation between pixels and therefore a reduction in image sharpness and quality. A nano-sized Ce:YAG phosphor is more compatible with such microLED displays, and has the added advantage of reducing optical scattering. The optical scattering of ambient light limits the contrast ratio of the display.

Producing nano-sized Ce:YAG phosphors has been demonstrated by solution based synthesis approaches, such as the sol-gel method, co-precipitation method, ethanol-water solvothermal method, and glycothermal method.[7.7.13-7.7.21] However, the sol-gel and co-precipitation methods require calcination at elevated temperatures, whereas the solvothermal and glycothermal approaches provide crystallized YAG directly from solution with no further annealing required. Further, the hydrothermal method demands high pressures and long reaction times in order to produce phase-pure YAG. Alternatively, the glycothermal method offers comparatively more moderate reaction temperatures, pressures, and reaction times to achieve phase pure, monodispersed YAG nanophosphors. The glycothermal method entails reacting metal alkoxide precursors in a high boiling point glycol solvent at elevated temperatures in a sealed reaction chamber. As a consequence of the metal alkoxide precursors used, organic species are typically observed on the particle surface upon completion of the synthesis.[7.7.23, 7.7.24]

The lack of a red component in the emission profile of Ce:YAG has been an ongoing topic of research.[7.7.25-7.7.28] Since the absorption and emission characteristics of

Ce are directly dependent on the properties of the host, the usual approach for tuning Ce emission and absorption spectra involves modifying parameters of the local crystal field imposed by the host crystal.[7.7.29, 7.7.30] Gadolinium is often the dopant of choice, as it is larger in size than Y. Gd is optically inactive and it carries the same charge as Y.[7.7.26, 7.7.31] The larger ionic size of Gd distorts the dodecahedron outwards, which then shifts oxygen atoms closer to neighbouring Ce atoms, redshifting its emission. A similar strategy involves the use of Mg^{2+}-Si^{4+} pairs in place of Al^{3+}-Al^{3+} pairs in octahedral-tetrahedral co-ordination, respectively.[7.7.32-7.7.34] In this case, a pair substitution is necessary to maintain overall charge neutrality.

The adoption of Ce into YAG via the glycothermal method has been studied extensively in recent years.[7.7.19-7.7.24, 7.7.30] However, most of the focus has been on an absolute size reduction of the nanophosphor, as opposed to tuning the optical properties. This study aims to demonstrate the ability to adjust the spectral properties of Ce in a YAG-based host with an *in situ* adoption of Mg^{2+}-Si^{4+} pairs using the glycothermal method, not previously reported on to the best of the authors' knowledge.

7.4. Experimental

7.4.1. Synthesis of $Ce_{0.03}:Y_{2.97}Mg_xAl_{(5-2x)}Si_xO_{12}$ nanophosphors

$Ce_{0.03}:Y_{2.97}Mg_xAl_{(5-2x)}Si_xO_{12}$ nanophosphors were synthesized using the glycothermal method. Stoichiometric amounts of Y acetate hydrate (99.9%, Sigma Aldrich), Ce acetate hydrate (99.9%, Sigma Aldrich), Al isopropoxide (≥ 98%, Sigma Aldrich), Mg acetate hydrate (≥ 99%, Sigma Aldrich) were ground in an agate mortar

before being added to 20 mL of 1,4 butanediol (1,4 BD, 99%, Sigma Aldrich) solvent with stoichiometric additions of tetraethylorthosilicate (TEOS, 98%, Sigma Aldrich) for Mg and Si values of x = 0, 0.5, 1, and 1.5. The mixture was magnetically stirred for 15 minutes before being added to a test tube held within a 53 mL autoclave fabricated using Swagelok Co. components. 8 mL of 1,4 BD solvent was held between the test tube liner and autoclave wall. The autoclave was purged with N_2, sealed, and heated to 315º C at a rate of ~3.2 ºC/min over 90 minutes. The samples remained at 315 ºC for 3 hours, with stirring at 300 rpm via a magnetic stir bar on a hot plate. Once cooled to room temperature, the pale yellow nanophosphors were washed three times by centrifugation at 15 000 rpm with ethanol, and dried overnight at 90 ºC. The same procedure was repeated for samples made with x=0 at 300ºC.

7.4.2. Characterization

The crystal structure of the YAG based nanophosphors was confirmed using x-ray diffraction. A Bruker D8 DISCOVER diffractometer with Co Kα source (λ_{avg} = 1.79026 Å) was used, and diffraction peaks were referenced to $Y_3Al_5O_{12}$ (ICDD PDF #00-033-0040). Rietveld refinement was performed in the TOPAS software to determine microstructure parameters. Electron microscopy was performed on a Thermo Scientific TALOS 200X transmission electron microscope followed by diameter measurements using National Institute of Health (NIH) ImageJ software. Confirmation of Mg and Si inclusion was achieved using EDS mapping on the same TEM operating in STEM mode with a high angle annular dark field (HAADF) and four in-column SDD Super-X detectors. Thermogravimetric analysis was performed on the precursor materials under 30 mL/min

Ar flow using a Mettler Toledo TGA-DSC 3+ system in the range of 25 ºC to 600 ºC by heating 25 ºC to to 100 ºC at a rate of 20 K/min, followed by a 5 minute isothermal stage at 100 ºC to expel any residual moisture, before proceeding to the temperature range of 100 ºC to 600 ºC at a rate of 10 K/min. Photoluminescence (PL) and photoluminescence excitation (PLE) measurements of the formed nanophosphors were performed on a Tecan Infinite M200 Pro Plate Reader by making solutions of dried nanoparticles in ethanol at a concentration of 5 mg/mL with dispersion via ultrasonication for 10 minutes. PL/PLE measurements for samples synthesized at 300ºC and 315ºC were obtained at fixed concentrations of 200 µg/mL to reduce the effect of optical scattering. Photoluminescence quantum yield (PLQY) of powder samples synthesized at 300ºC and 315ºC were evaluated using an integrating sphere (LabSphere) and spectrometer equipped with a CCD detector (Ocean Optics 2000+) with a 375 nm diode laser (Coherent OBIS LX) acting as the excitation source. Full details of this measurement can be found in Chapter 5.9.

7.4.3. Surface Modification of Nanophosphors

Surface modification of the formed Ce:YAG nanophosphors was carried out by washing the nanoparticles with centrifugation in a 0.1 M HCl solution three times, followed by washing in distilled water three times before dispersing in 20 mL distilled water. Citric acid was added in a 1:2 weight ratio between citric acid and the nanopowder, and the mixture was stirred at 700 rpm at 75 ºC for 30 minutes on a hot plate. The product was then washed three times by centrifugation with distilled water and dried at 120 ºC overnight. The presence of surface organic groups was verified after nanoparticle synthesis, washing

with HCl, and after addition of citric acid using a Bruker Hyperion 3000 FTIR spectrometer operating in attenuated total reflectance (ATR) mode in a range from 4000-400 cm^{-1}.

7.5. Results and Discussion

7.5.1. Structural and Optical Characterization of $Ce_{0.03}:Y_{2.97}Mg_xAl_{(5-2x)}Si_xO_{12}$ nanophosphors

Figure 7.1 shows the structural evolution of the formed $Ce_{0.03}:Y_{2.97}Mg_xAl_{(5-2x)}Si_xO_{12}$ nanopowders using the glycothemal method, with x values of 0, 0.5, 1, 1.5. The obtained spectra are referenced to that of pure YAG (ICDD PDF# 00-033-0040). The inset of Figure 7.1 highlights the shift in the dominant 2θ peak around 38.5º, likely caused by larger Mg ion substitution at the Al octahedral site. This is thought to be the case due to the similar size of the Mg^{2+} ion (78 pm) and the Al^{3+} ion at the octahedral site (68 pm), and Si^{4+} (39 pm) substituting for Al^{3+} at the tetrahedral site (53 pm).[34] Results of the Rietveld refinement, summarized in Figure 7.1, show that the lattice spacing increases fairly linearly with increasing Mg-Si addition. In order to confirm the inclusion of Mg and Si in the final product, EDS mapping was undertaken, shown in Figure 7.2. Figure 7.2 shows a uniform distribution of Mg and Si, indicating a homogeneous inclusion during the glycothermal reaction.

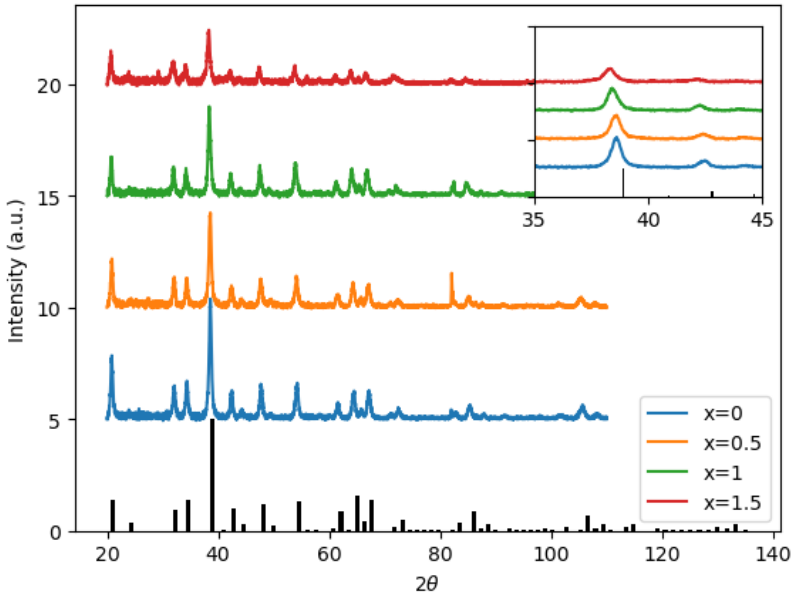

x	Lattice constant (Å)	Crystallite Size (nm)
0	12.083	42
0.5	12.113	36.2
1	12.154	41
1.5	12.176	26.6

Figure 7.1: XRD spectra of dried $Ce_{0.03}:Y_{2.97}Mg_xAl_{(5-2x)}Si_xO_{12}$ powders.

Top: Diffraction patterns of x = 0, 0.5, 1, 1.5. Referenced to ICDD PDF# 00-033-0040).

Inset: Magnified view of 38.5° 2θ peak. Bottom: Microstructure parameters obtained by Rietveld refinement.

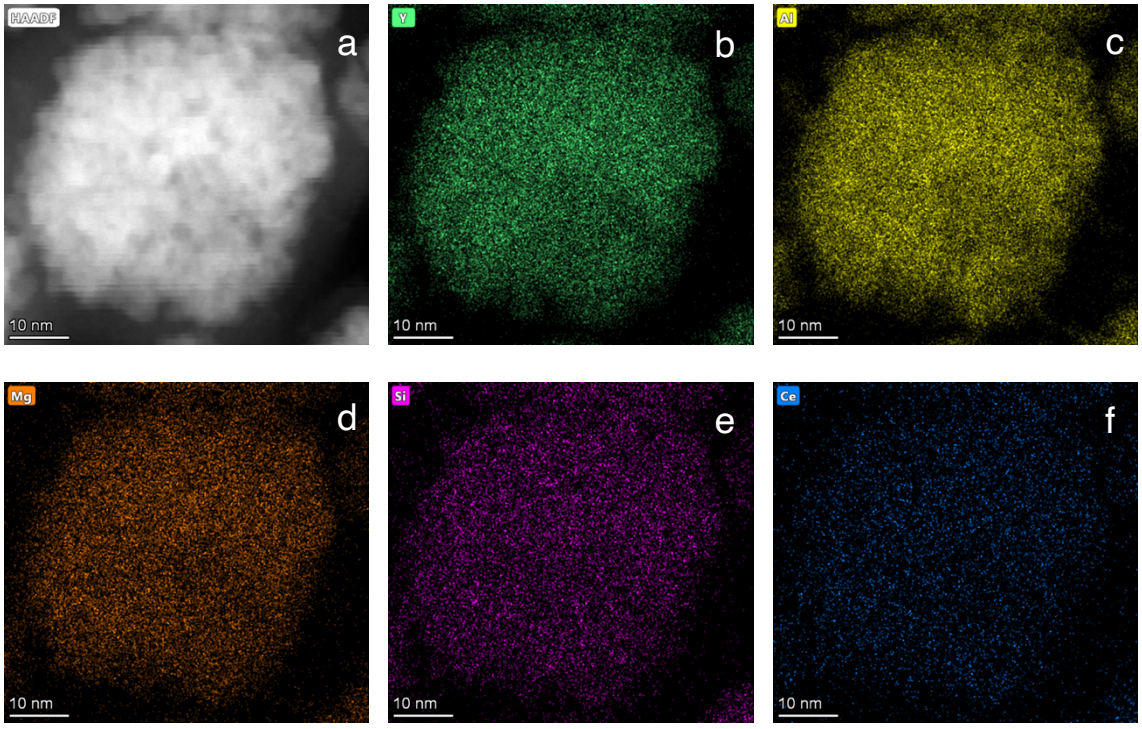

Figure 7.2:EDS mapping of $Ce_{0.03}:Y_{2.97}Mg_xAl_{(5-2x)}Si_xO_{12}$ with x = 1.
a) STEM image of area mapped. Elemental mapping of b) Y, c) Al, d) Mg, e) Si, f) Ce. Scale bar indicates 10 nm.

To evaluate the viability of Mg-Si addition to alter the optical properties of Ce:YAG, photoluminescent excitation (PLE) spectra and photoluminescent emission (PL) spectra were obtained, as shown in Figure 7.3. The general trend was that with the increased addition of Mg and Si, there was a blueshift in the absorption, and a small redshift in the emission. This is likely attributed to the Franck-Condon principle, which describes how a spatial offset between the ground and excited state, such as that induced by the Mg-Si addition, can alter the energy of the absorption and emission transitions.[7.7.35] Moreover, it describes the intensities of the observed transitions as an indication of the degree of overlap between the ground and excited state wavefunctions. The spectra presented in Figure 7.3

are normalized in order to highlight shifts in the spectra, however it was observed that the intensity of absorption and emission decreased as the Mg-Si content increased. This may also explain the discrepancy in the x = 1.5 emission profile, as the signal-to-noise ratio in this case was low. With Mg^{2+}-Si^{4+} substitution, the effect on Ce redshifting can be two-fold: the larger ionic size of Mg^{2+} compared to Al^{3+} distorts the octahedron outwards, and the oxygen atoms in the Si-O bond experience an increased degree of covalency compared to that of Al-O, which are then stabilized with an outward Coulombic repulsion.

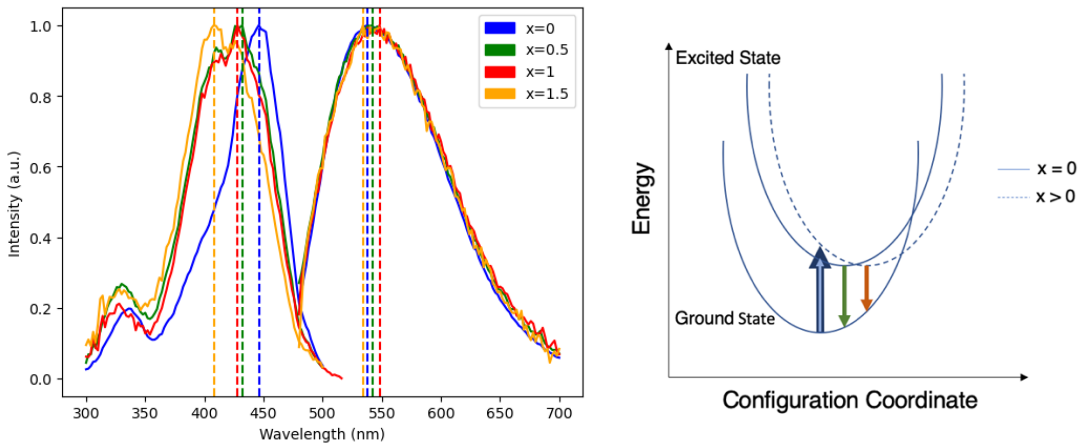

Figure 7.3: PLE and PL $Ce_{0.03}:Y_{2.97}Mg_xAl_{(5-2x)}Si_xO_{12}$ nanophosphors.
Left: Normalized PLE and PL spectra of $Ce_{0.03}:Y_{2.97}Mg_xAl_{(5-2x)}Si_xO_{12}$, with x = 0, 0.5, 1, and 1.5. Dashed vertical lines indicate spectral maxima for PLE and PL, respectively: 446 nm and 538 nm for x=0, 432 nm and 542 nm for x = 0.5, 428 nm and 548 nm for x = 1, and 408 nm and 534 nm for x = 1.5. Right: Schematic of Franck-Condon principle demonstrating the origin of absorption blueshift and emission redshift in $Ce_{0.03}:Y_{2.97}Mg_xAl_{(5-2x)}Si_xO_{12}$.

7.5.2. Effect of Increased Reaction Temperature on Ce:YAG Nanophosphors

Glycothermal synthesis of Ce:YAG was first presented in 2006 by Isobe et al. by reacting yttrium and cerium acetates with aluminum isopropoxide in 1,4 butanediol, and the reaction temperature to produce phase pure YAG was 300 ºC. Since then, it has generally been accepted that Ce:YAG nanophosphors are to be synthesized at 300 ºC.[7.7.21-7.7.23] However, there has been little study into the behavior of the precursor materials at those temperatures in the context of reaction kinetics. As such, thermogravimetric analysis (TGA) was performed on the precursor powders to get an indication of at what temperatures the C-O bond of the metal-organic precursors cleave via thermal decomposition, as shown in Figure 7.4. There is an initial significant weight loss at 100 ºC, which is attributed to vaporization of residual moisture. It was observed that the majority of weight loss for Y, Ce, and Mg precursors occurred above 300 ºC, although the initial bond cleavage for Al occurred well below this temperature.

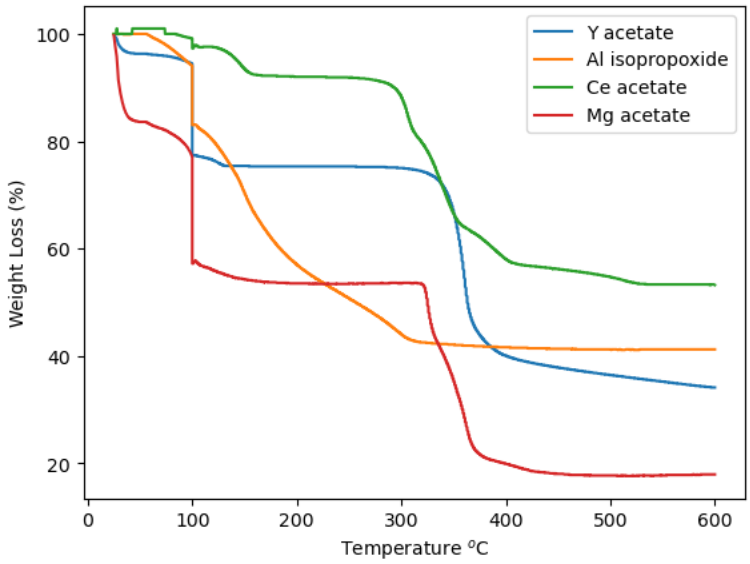

Figure 7.4: TGA of precursor alkoxide powders.

Cleavage of the C-O bond provides a site for nucleation to occur, and it is therefore critical that all precursors are available for reaction at a similar time in order to facilitate homogeneous incorporation in the final product. This approach comes at the cost of particle size and size distribution control, as an increased reaction temperature encourages higher precursor dissolution and therefore precursor availability during the growth phase.[7.7.36] This can be seen in Figure 7.5, comparing Ce:YAG synthesized at 315 ºC vs. 300 ºC. The average particle sizes measured from TEM images were 56 ± 16 nm, and 41 ± 7 nm, respectively, in reasonable agreement with the 42.0 nm and 50.1 nm for 315ºC vs. 300ºC samples calculated from Rietveld refinement. The optical performance of the nanophosphors at 315 ºC vs 300 ºC was evaluated and is presented in Figure 7.6. The higher temperature shows a marked improvement in optical performance, with a 3.3x enhancement in PLE and a 3.7x enhancement in PL. In addition, the photoluminescence

quantum yield (PLQY) increased from 31.8% for samples made at 300ºC to 48.2% for those made at 315ºC. This may be due to an improvement in the homogeneity of the dodecahedrally coordinated Ce atom sites, which reduces the potential for non-radiative transitions via dopant clustering. In addition the increase in particle size results in a smaller surface area-to-volume ratio compared to that for the smaller particles synthesized at the lower temperature. This reduces the influence of surface defects. Surface defects and surface states associated with dangling bonds are well known to quench luminescence.[7.7.24, 7.7.37]

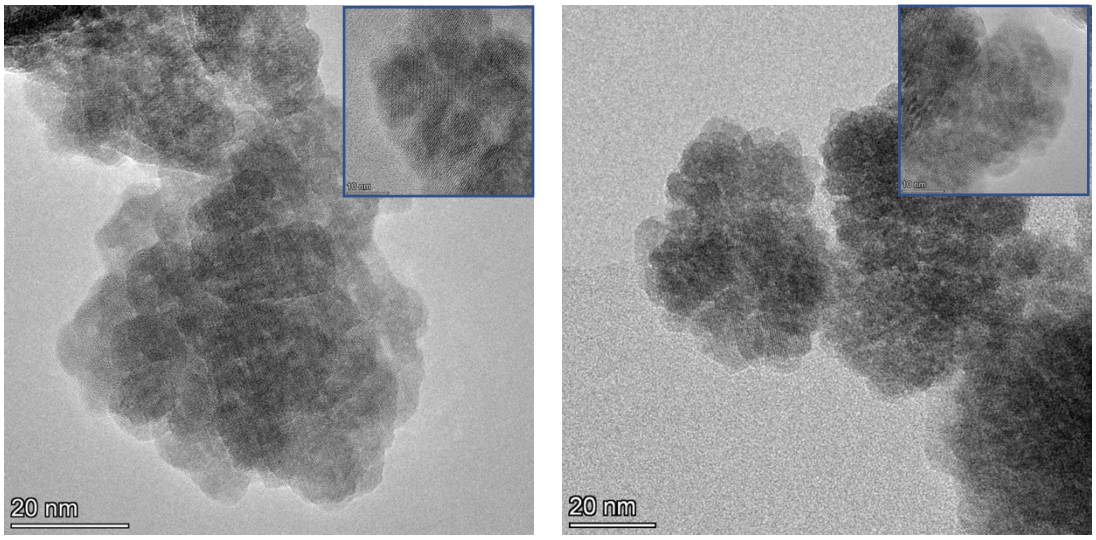

Temperature	Particle Size (nm)	Crystallite Size (nm)	Lattice Constant (Å)
300	41 ± 7	50.1	12.0803146
315	56 ± 16	42.0	12.0832839

Figure 7.5:TEM images of formed Ce:YAG at 300 ºC (left) and 315 ºC (right). Inset: HRTEM images (scale bar is 10 nm). Bottom: summary of microstructure between samples made at 300ºC and 315ºC. Particle size measured from TEM images, crystallite size and lattice constant calculated using Rietveld refinement of XRD data.

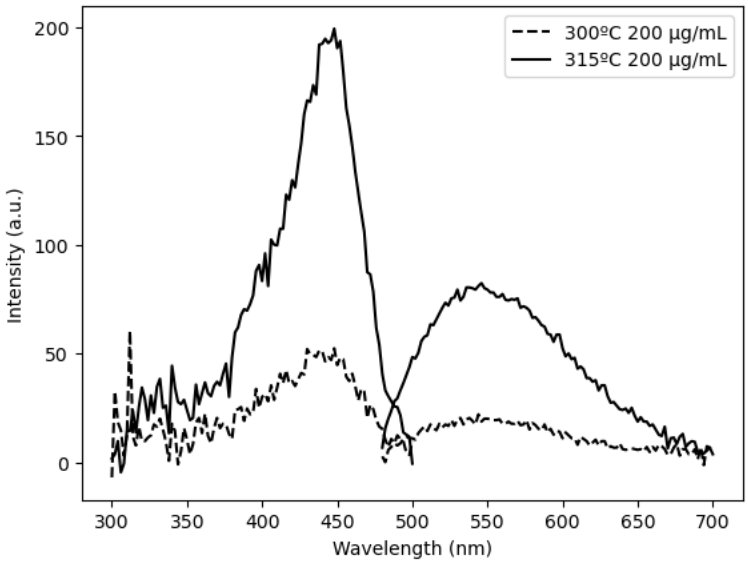

Figure 7.6: PLE and PL of Ce:YAG with for 300 ºC (dashed line) and 315 ºC (solid line). Samples dispersed in ethanol at a concentration of 200 µg/mL. PLQY values of samples made at 300ºC and 315ºC were 31.8% and 48.2%, respectively.

7.5.3. Surface modification of Ce:YAG nanoparticles

In an attempt to broaden the range of functionality of the Ce:YAG nanoparticles for integration in a wider variety of applications, the residual organic groups on the particle surface were removed and replaced with citric acid, as shown by the surface sensitive FTIR-ATR results in Figure 7.7. The peaks highlighted in red of Figure 7.7 are attributed to the symmetric and asymmetric stretching of C=O bonds at ~1600 and ~1500 cm^{-1} respectively, and originate from residual acetate groups from the Y and Ce precursors remaining on the particle surface, which are removed after washing in a mild acidic solution. Upon heating in a solution containing citric acid, the peaks appear again, indicating the re-formation of the C=O bond and therefore the grafting of citric acid on the particle surface. This relatively simple and straightforward technique can potentially

improve the compatibility of Ce:YAG nanoparticles with epoxies, polymers, or composites provided an appropriate C=O functional group anchor can be formed.

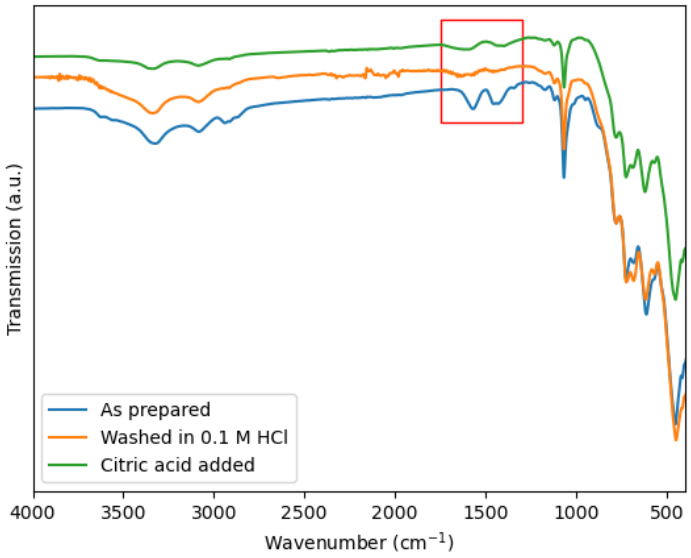

Peak position (cm^{-1})	Assignment
~3400	ν(OH)
~3100	ν_s(CH_2)
~2900	ν_{as}(CH_2)
~1600	ν_s(C=O)
~1400	ν_{as}(C=O)
~1150	δ(CH_2)

Figure 7.7: FTIR spectra of as prepared Ce:YAG samples after stripping of surface organic groups.

Surface groups were treated with a 0.1 M HCl solution, with citric acid grafted post-treatment. The region of interest, namely the symmetric and asymmetric stretching of C=O bonds at ~1600 cm^{-1} and ~1500 cm^{-1} respectively, is highlighted in red. Peak assignments are taken from [7.7.23] and [7.7.38].

7.6. Conclusion

The optical properties of Ce:YAG were modified by the addition of Mg-Si pairs to the host lattice using the glycothermal method. A moderate blueshift in absorption and slight redshift in emission was observed. Increasing the reaction temperature by 15ºC provided a significant improvement in both absorption and emission. This increases the

versatility of Ce:YAG – based nanophosphors permitting, for example, the nanophosphor absorption spectrum to be better tuned to the emission spectrum of a blue microLED source emitting between 400 and 450nm. A technique is proposed to further modify the nanoparticle surface post-synthesis which can, in future, enable the nanophosphor to be incorporated in organic binders.

7.7. References

7.7.1 Zhao, C., & Duan, L. (2020). Review on photo-and electrical aging mechanisms for neutral excitons and ions in organic light-emitting diodes. *Journal of Materials Chemistry C*, *8*(3), 803-820.

7.7.2 Scholz, S., Kondakov, D., Lussem, B., & Leo, K. (2015). Degradation mechanisms and reactions in organic light-emitting devices. *Chemical reviews*, *115*(16), 8449-8503.

7.7.3 Dong, S. C., Xu, L., & Tang, C. W. (2017). Chemical degradation mechanism of TAPC as hole transport layer in blue phosphorescent OLED. *Organic Electronics*, *42*, 379-386.

7.7.4 Liu, G. H., Zhou, Z. Z., Shi, Y., Liu, Q., Wan, J. Q., & Pan, Y. B. (2015). Ce: YAG transparent ceramics for applications of high power LEDs: Thickness effects and high temperature performance. *Materials Letters*, 139, 480-482.

7.7.5 Fujita, S., Yoshihara, S., Sakamoto, A., Yamamoto, S., & Tanabe, S. (2005, September). YAG glass-ceramic phosphor for white LED (I): background and development. In *Fifth International Conference on Solid State Lighting* (Vol. 5941, p. 594111). International Society for Optics and Photonics.

7.7.6 Shen, X., Zhang, D. F., Fan, X. W., Hu, G. S., Bian, X. B., & Yang, L. (2016). Fabrication and characterization of YAG: Ce phosphor films for white LED applications. *Journal of Materials Science: Materials in Electronics*, *27*(1), 976-981.

7.7.7 Xu, Y. N., & Ching, W. Y. (1999). Electronic structure of yttrium aluminum garnet ($Y_3Al_5O_{12}$). *Physical Review B*, *59*(16), 10530.

7.7.8 Ghigna, P., Pin, S., Ronda, C., Speghini, A., Piccinelli, F., & Bettinelli, M. (2011). Local structure of the Ce^{3+} ion in the yellow emitting phosphor YAG: Ce. *Optical Materials*, *34*(1), 19-22.

7.7.9 Shionoya, S., Yen, W. M., & Yamamoto, H. (Eds.). (2018). *Phosphor handbook*. CRC press.

7.7.10 Ikesue, A., Furusato, I., & Kamata, K. (1995). Fabrication of polycrystal line, transparent YAG ceramics by a solid-state reaction method. *Journal of the American Ceramic Society*, *78*(1), 225-228.

7.7.11 Song, Z., Liao, J., Ding, X., Liu, X., & Liu, Q. (2013). Synthesis of YAG phosphor particles with excellent morphology by solid state reaction. *Journal of crystal growth*, *365*, 24-28.

7.7.12 Ghrib, T., Al-Otaibi, A. L., Almessiere, M. A., Ashahri, A., & Masoudi, I. (2017). Structural, optical and thermal properties of the Ce doped YAG synthesized by solid state reaction method. Thermochimica Acta, 654, 35-39.

7.7.13 Veith, M., Mathur, S., Kareiva, A., Jilavi, M., Zimmer, M., & Huch, V. (1999). Low temperature synthesis of nanocrystalline $Y_3Al_5O_{12}$ (YAG) and Ce-doped

$Y_3Al_5O_{12}$ via different sol–gel methods. *Journal of Materials Chemistry*, *9*(12), 3069-3079.

7.7.14 Xia, G., Zhou, S., Zhang, J., & Xu, J. (2005). Structural and optical properties of YAG: Ce^{3+} phosphors by sol–gel combustion method. *Journal of Crystal Growth*, *279*(3-4), 357-362.

7.7.15 Yuan, F., & Ryu, H. (2004). Ce-doped YAG phosphor powders prepared by co-precipitation and heterogeneous precipitation. *Materials Science and Engineering: B*, *107*(1), 14-18.

7.7.16 Zhang, K., Liu, H. Z., Wu, Y. T., & Hu, W. B. (2008). Co-precipitation synthesis and luminescence behavior of Ce-doped yttrium aluminum garnet (YAG: Ce) phosphor: The effect of precipitant. *Journal of alloys and compounds*, *453*(1-2), 265-270.

7.7.17 Li, X., Liu, H., Wang, J., Cui, H., & Han, F. (2004). YAG: Ce nano-sized phosphor particles prepared by a solvothermal method. Materials Research Bulletin, 39(12), 1923-1930.

7.7.18 Lin, W. T., & Wu, Y. C. (2015). One-pot synthesis of submicrometer-sized Ce: YAG spherical particles by solvothermal process using alcohol solvents. *Journal of the American Ceramic Society*, *98*(9), 2754-2759.

7.7.19 Kasuya, R., Isobe, T., & Kuma, H. (2006). Glycothermal synthesis and photoluminescence of YAG: Ce^{3+} nanophosphors. *Journal of alloys and compounds*, *408*, 820-823.

7.7.20 Isobe, T. (2012). Glycothermally synthesized YAG: Ce^{3+} nanophosphors for blue LEDs. *ECS Journal of Solid State Science and Technology*, *2*(2), R3012.

7.7.21 Odziomek, M., Chaput, F., Lerouge, F., Sitarz, M., & Parola, S. (2017). Highly luminescent YAG: Ce ultra-small nanocrystals, from stable dispersions to thin films. *Journal of Materials Chemistry C*, *5*(47), 12561-12570.

7.7.22 Revaux, A., Dantelle, G., George, N., Seshadri, R., Gacoin, T., & Boilot, J. P. (2011). A protected annealing strategy to enhanced light emission and photostability of YAG: Ce nanoparticle-based films. *Nanoscale*, *3*(5), 2015-2022.

7.7.23 Ramanujam, P., Vaidhyanathan, B., Binner, J. G. P., Ghanizadeh, S., & Spacie, C. (2016). Solvothermal nanoYAG synthesis: Mechanism and particle growth kinetics. *The Journal of Supercritical Fluids*, *107*, 433-440.

7.7.24 Nyman, M., Shea-Rohwer, L. E., Martin, J. E., & Provencio, P. (2009). Nano-YAG: Ce mechanisms of growth and epoxy-encapsulation. *Chemistry of Materials*, *21*(8), 1536-1542.

7.7.25 Chawla, S., Roy, T., Majumder, K., & Yadav, A. (2014). Red enhanced YAG: Ce, Pr nanophosphor for white LEDs. *Journal of Experimental Nanoscience*, *9*(8), 776-784.

7.7.26 Chen, J., Deng, Z., Liu, Z., Lin, Y., Lan, H., Chen, D., ... & Cao, Y. (2015). Optical enhancement brought by doping Gd^{3+} ions into Ce: YAG ceramics for indoor white light-emitting diodes. *Optics express*, *23*(7), A292-A298.

7.7.27 Jang, H. S., Im, W. B., Lee, D. C., Jeon, D. Y., & Kim, S. S. (2007). Enhancement of red spectral emission intensity of Y3Al5O12: Ce3+ phosphor via Pr co-doping

and Tb substitution for the application to white LEDs. Journal of luminescence, 126(2), 371-377.

7.7.28 Chen, D., Zhou, Y., Xu, W., Zhong, J., Ji, Z., & Xiang, W. (2016). Enhanced luminescence of Mn^{4+}:$Y_3Al_5O_{12}$ red phosphor via impurity doping. *Journal of Materials Chemistry C*, *4*(8), 1704-1712.

7.7.29 Pan, Y. X., Wang, W., Liu, G. K., Skanthakumar, S., Rosenberg, R. A., Guo, X. Z., & Li, K. K. (2009). Correlation between structure variation and luminescence red shift in YAG: Ce. *Journal of Alloys and Compounds*, *488*(2), 638-642.

7.7.30 Peter, S., Patel, A., & Kitai, A. (2019). Photoluminescence enhancement of Ce: YAG nanophosphors via doped/intrinsic core/shell structures. *Journal of Luminescence*, *211*, 82-87.

7.7.31 Chen, L., Chen, X., Liu, F., Chen, H., Wang, H., Zhao, E., ... & Wang, Y. (2015). Charge deformation and orbital hybridization: intrinsic mechanisms on tunable chromaticity of $Y_3Al_5O_{12}$: Ce^{3+} luminescence by doping Gd^{3+} for warm white LEDs. *Scientific reports*, *5*, 11514.

7.7.32 Du, Q., Feng, S., Qin, H., Hua, H., Ding, H., Jia, L., ... & Jiang, H. (2018). Massive red-shifting of Ce^{3+} emission by Mg^{2+} and Si^{4+} doping of YAG: Ce transparent ceramic phosphors. *Journal of Materials Chemistry C*, *6*(45), 12200-12205.

7.7.33 Maniquiz, M. C., Jung, K. Y., & Jeong, S. M. (2010). Luminescence Characteristics of $Y_3Al_{5-2y}(Mg, Si)_yO_{12}$: Ce Phosphor Prepared by Spray Pyrolysis. *Journal of The Electrochemical Society*, *157*(12), H1135.

7.7.34 Shang, M., Fan, J., Lian, H., Zhang, Y., Geng, D., & Lin, J. (2014). A double substitution of Mg^{2+}–Si^{4+}/Ge^{4+} for $Al_{(1)}^{3+}$–$Al_{(2)}^{3+}$ in Ce^{3+}-doped garnet phosphor for white LEDs. *Inorganic Chemistry, 53*(14), 7748-7755.

7.7.35 Lax, M. (1952). The Franck-Condon principle and its application to crystals. *The Journal of chemical physics*, *20*(11), 1752-1760.

7.7.36 Dantelle, G., Testemale, D., Homeyer, E., Cantarano, A., Kodjikian, S., Dujardin, C., ... & Ibanez, A. (2018). A new solvothermal method for the synthesis of size-controlled YAG: Ce single-nanocrystals. *RSC advances*, *8*(47), 26857-26870.

7.7.37 Saladino, M. L., Zanotto, A., Chillura Martino, D., Spinella, A., Nasillo, G., & Caponetti, E. (2010). Ce: YAG nanoparticles embedded in a PMMA matrix: preparation and characterization. *Langmuir*, *26*(16), 13442-13449.

7.7.38 Asakura, R., Isobe, T., Kurokawa, K., Takagi, T., Aizawa, H., & Ohkubo, M. (2007). Effects of citric acid additive on photoluminescence properties of YAG: Ce^{3+} nanoparticles synthesized by glycothermal reaction. *Journal of luminescence*, *127*(2), 416-422.

Chapter 8: Red Enhanced Ce:YAG Nanophosphors via Ce^{3+}-Mn^{2+} Energy Transfer

8.1. Preface

The purpose of this research was to demonstrate an enhancement in the red component of Ce:YAG nanophosphors through the use of Mn^{2+} as a co-dopant. As a transition metal luminescent center, Mn^{2+} requires octahedral co-ordination to exhibit red luminescence, and as demonstrated in previous works, Ce:YAG nanophosphors synthesized via the glycothermal method have ~10x more octahedral Al sites than bulk Ce:YAG. It was found however that the Mn^{2+} precursor preferentially occupies the Y^{3+} dodecahedral site, although the Mn^{2+} which does occupy the octahedral Al sites was shown to exhibit red luminescence. Moreover, the red emission is enhanced by the addition of an intrinsic YAG shell layer. Fluorescence lifetime measurements of the Ce lifetime showed that non-radiative energy transfer between Ce and Mn luminescence centers occurs.

This article was co-authored with Morgan Richards and Dr. Qiyin Fang. Morgan was instrumental in the design of the lab-made single photon counting setup used for the measurement of fluorescent lifetimes, as well as the analysis of the data. Dr. Fang and Morgan also contributed to the editing of the manuscript. This research article has been accepted for publication in the journal *Materials Chemistry and Physics* and is currently in press.

DOI: https://doi.org/10.1016/j.matchemphys.2021.125497

8.2. Abstract

Mn^{2+} was shown to be incorporated as a co-dopant in glycothermally synthesized Ce:YAG-based nanophosphors to enhance the red component of the emission spectrum. Structural characterization showed a preferential inclusion of Mn^{2+} in the Y site. Al^{IV}/Al^{VI} ratios were found to decrease from 0.25 in Ce:YAG nanophosphors to 0.11 with the addition of Mn^{2+}, indicating a ~10x increase in octahedral Al sites over bulk Ce:YAG, particularly on the particle surface. Luminescence of Mn^{2+} at 594 nm, indicating octahedral Al site occupation was also observed, likely due to the high doping concentration of Mn^{2+}. Strategies to improve the luminescence of Mn^{2+} included adding Si^{4+} in the form of tetraethyl orthosilicate (TEOS) for charge compensation and the addition of an intrinsic shell layer to enhance the local crystal field. XPS confirmed no change of Mn^{2+} valence after reaction, indicating Mn (II) acetate to be a precursor compatible with the glycothermal method for the synthesis of Ce:YAG-based nanophosphors. 3 mol% Mn^{2+} was found to be a suitable doping concentration, with quenching observed at 5%. Addition of an intrinsic shell layer greatly improved the optical characteristics of the Mn^{2+} emission, and the photoluminescence quantum yield (PLQY) increased from 44% to 73%. Fluorescence lifetimes of nanocrystalline Ce:YAG and Mn^{2+} containing samples dropped from 101.1 ns to 90.7 ns, respectively, indicating the presence of a non-radiative energy transfer mechanism from Ce to Mn^{2+}.

8.3. Introduction

Cerium-doped yttrium aluminum garnet (Ce:YAG) phosphors paired with blue emitting InGaN based LEDs have created a semiconductor-based white lighting industry over the last 30 years.[8.7.1-8.7.5] Ce:YAG is uniquely suited for this, as its absorption in blue yields broadband yellow-green fluorescence, which when excited by a blue LED produces white light at only a few volts. Moreover, as an oxide material, it is highly stable in high temperature applications and is not sensitive to oxidative degradation. As a garnet, the YAG crystal structure comprises Y atoms surrounded by O atoms in dodecahedral symmetry, and Al atoms in both tetrahedral and octahedral symmetry at an Al^{IV}/Al^{VI} ratio of 3/2.

The pairing of Ce:YAG phosphor with blue LEDs has often been the solution for providing white lighting in LCD display technology applications, however in recent years, other digital display types using OLED and microLED technologies have seen market penetration. This is principally due to limitations of LCD display technology, including limited contrast ratios and panel sizes. Ce:YAG as a microLED phosphor is problematic: conventional synthesis yields micron sized powders, too large for microLED compatibility, and the limited red component in the emission spectrum produces a non-optimal colour gamut.[8.7.6, 8.7.7] The first of these drawbacks can be addressed by reducing the size of the phosphor. Several techniques exist for producing nanocrystalline materials from solution, including the sol-gel, co-precipitation, hydrothermal, and solvothermal methods.[8.7.8-8.7.17] While the sol-gel and co-precipitation methods are useful for producing fully dense, transparent phosphors, the temperature required for synthesis still produces a product on

the micron scale.[8.7.8-8.7.11] Hydrothermal and solvothermal approaches have been shown to produce nanosized, monodispersed crystals at temperatures much lower than that of the previous mentioned methods. Of the two, the hydrothermal method requires high pressures to produce a phase pure product, and so much of recent research has explored the solvothermal method, particularly in high boiling point glycol solvents, known more specifically as the glycothermal method. This method, in which metal alkoxide precursors react with the solvent, has been shown to produce nanoparticles with highly defective surfaces; in particular, Al^{IV}/Al^{VI} ratios significantly lower than single crystal YAG.[8.7.16, 8.7.18-8.7.20] Strategies to improve the fluorescence intensity of glycothermally synthesized Ce:YAG nanophosphors have involved a post synthesis protected annealing step, as well as growth of core/shell structures *in situ*.[8.7.19, 8.7.20]

Efforts have been made to improve the emission spectrum of Ce:YAG.[8.7.21-8.7.36] Due to the high sensitivity of Ce emission to its local crystal field, this is typically achieved by modifying the crystal structure, usually by the addition of larger rare earth ions in the Y site, although tuning the crystal field at the Al site has also been demonstrated.[8.7.21-8.7.25] The spin allowed $5d \rightarrow 4f$ transitions in Ce has also been shown to be an effective sensitizer for energy transfer to secondary dopant ions for fluorescence downconversion.[8.7.26-8.7.36] Candidate ions for energy transfer effects include rare earth dopants in the Y site, however, these materials are relatively expensive. Alternatively, transition metals such as Mn and Cr offer a cost effective alternative, and act as red emitting luminescent centers when in the presence of a crystal field of octahedral symmetry.[8.7.27-8.7.33, 8.7.36, 8.7.37] It is the aim of this study to demonstrate a red-enhanced emission of glycothermally synthesized Ce:YAG-

based nanophosphors via Ce-Mn energy transfer. The novelty of this approach stems from the use of the glycothermal method for the introduction of Mn as a dopant, as the defects present using this method of synthesis offer a more ideal crystal field for Mn^{2+} luminescence.

8.4. Experimental

8.4.1. Synthesis of $Ce_{0.03},Mn_xSi_y:Y_{2.97}Al_{(1-x-y)5}O_{12}$ nanophosphors

Synthesis of $Ce_{0.03},Mn_xSi_y:Y_{2.97}Al_{(1-x-y)5}O_{12}$ nanophosphors was carried out using the glycothermal method. Stoichiometric amounts of yttrium acetate hydrate (99.9%, Sigma Aldrich), cerium acetate hydrate (99.9%, Sigma Aldrich), aluminum isopropoxide (≥ 98%, Sigma Aldrich), and manganese acetate tetrahydrate (≥ 99%, Sigma Aldrich) were ground in an agate mortar before being added to 20 mL of 1,4 butanediol (1,4 BD, 99%, Sigma Aldrich) as the solvent, with stoichiometric additions of tetraethyl orthosilicate (TEOS, 98%, Sigma Aldrich) as a charge compensator, when necessary. Samples were prepared with Mn content of x = 0, 0.01, 0.03, and 0.05, and Si content of y = 0.03. Details of the sample preparation conditions are summarized in Table 8.1. The mixture was magnetically stirred for 15 minutes before being added to a test tube lined lab-made 53 mL autoclave made with Swagelok Co. components. 8 mL of 1,4 BD solvent was added between the test tube liner and autoclave wall. The reaction vessel was purged with N_2, sealed, and heated to 315º C at a rate of ~3.2 ºC/min over 90 minutes. The reaction vessel was held at this temperature for 3 hours with stirring at 300 rpm achieved with a magnetic

stir bar and hot plate. Once cooled, the samples were washed three times by centrifugation at 15 000 rpm in isopropyl alcohol, and dried overnight at 90 ºC.

Notation	Ce content	x	y	Chemical Formula
Ce:YAG	0.01	0	0	$Ce_{0.03}:Y_{2.97}Al_5O_{12}$
Ce, 1% Mn: YAG	0.01	0.01	0	$Ce_{0.03}$, $Mn_{0.05}:Y_{2.97}Al_{4.95}O_{12}$
Ce, 3% Mn: YAG	0.01	0.03	0	$Ce_{0.03}$, $Mn_{0.15}:Y_{2.97}Al_{4.85}O_{12}$
Ce, 5% Mn:YAG	0.01	0.05	0	$Ce_{0.03}$, $Mn_{0.25}:Y_{2.97}Al_{4.75}O_{12}$
Ce, 3% Mn, Si:YAG	0.01	0.03	0.03	$Ce_{0.03}$, $Mn_{0.15}$, $Si_{0.15}:Y_{2.97}Al_{4.70}O_{12}$
3% Mn, Si:YAG	0	0.03	0.03	$Mn_{0.15}$, $Si_{0.15}:Y_3Al_{4.70}O_{12}$
Ce, 3% Mn, Si:YAG / YAG	0.01	0.03	0.03	$Ce_{0.03}$, $Mn_{0.15}$, $Si_{0.15}:Y_{2.97}Al_{4.70}O_{12}$ / $Y_3Al_5O_{12}$

Table 8.1:Summary of $Ce_{0.03},Mn_xSi_y:Y_{2.97}Al_{(1-x-y)5}O_{12}$ sample conditions used in this study.

8.4.2. Characterization

The crystal structure of the nanophosphors was examined using a Bruker D8 DISCOVER diffractometer with Co Kα source (λ_{avg} = 1.79026 Å) referenced to $Y_3Al_5O_{12}$ (ICCD PDF# 00-033-0040). The nanocrystal microstructure was evaluated using Rietveld refinement with Le Bail fitting in TOPAS software with calibration of instrument broadening carried out using a LaB6 single crystal. Crystallite size broadening and strain calculations were performed using a double-Voigt approach. Co-ordination of aluminum sites was measured using a BRUKER AV 500 high resolution solid-state nuclear magnetic resonance (NMR) spectrometer operating in an 11.7 T static magnetic field and 4 μs pulse width. Single pulse excitation (SPE) was used to probe the overall ^{27}Al co-ordination, and $^{1}H \rightarrow {}^{27}Al$ cross polarization with a contact time of 500 μs was used to probe the ^{27}Al co-

ordination near the particle surface. 130.3 MHz and 500.25 MHz pulses were used for ^{27}Al and ^{1}H signals, respectively. The chemical shift of ^{27}Al was referenced to $Al(NO_3)_3$ dissolved in deuterium oxide. Electron microscopy was performed using a Thermo Scientific TALOS 200X transmission electron microscope, followed by nanoparticle size measurements performed using ImageJ. Elemental mapping was conducted using EDS mapping on the same TEM operating in STEM mode with a high angle annular dark field (HAADF) and four in-column SDD Super-X detectors. Analysis of the dopant oxidation state was performed via x-ray photoelectron spectroscopy (XPS), with a PHI Quantera II Scanning XPS Microprobe. The beam was operated at 15 kV with 0.8 eV step size for survey scans, and 0.1 eV for elemental scans. The presence of organic groups on the particle surface was confirmed using a Bruker Hyperion 3000 FTIR spectrometer operating in attenuated total reflectance (ATR) mode in a range from 4000-400 cm^{-1}. Photoluminescence and photoluminescence excitation (PL/PLE) of samples was conducted with a Tecan Infinite M200 Pro Plate Reader by making solutions of dried nanoparticles in ethanol at a concentration of 200 μg/mL with dispersion via ultrasonication for 10 minutes. An integration time of 2000 μs was used, and a lag time of 100 μs was introduced to observe Mn^{2+} emission characteristics. Fluorescence Lifetime was measured using direct pulse sampling, with a 440 nm PicoQuant LDH-P-C-440M pulsed diode laser (500 ps pulse) as an excitation source and Hamamatsu S8664-10K Si avalanche photodiode (APD) operated at 530 MHz and 460 V in reverse bias as a detector. Data was collected on a Tektronix DPO 7254 2.5 GHz oscilloscope at 40 GS/s with 1000 scans averaged. Fluorescence lifetimes were compared to a commercial Ce:YAG phosphor as a reference

(Phosphor Technology Ltd., UK). Photoluminescence quantum yield (PLQY) of powder samples was evaluated using an integrating sphere (LabSphere) and spectrometer equipped with a CCD detector (Ocean Optics 2000+) and with a 375 nm diode laser (Coherent OBIS LX) acting as the excitation source. Full details of this measurement can be found in previous reporting.[8.7.25]

8.5. Results and Discussion

8.5.1. Microstructure development of $Ce_{0.03},Mn_xSi_y:Y_{2.97}Al_{(1-x-y)5}O_{12}$ nanophosphors

X-ray diffraction (XRD) was performed to examine the microstructure evolution with increasing Mn^{2+} content, as well as with the growth of an intrinsic shell layer, shown in Figure 1. Mn content was tested at x = 0.01, 0.03, and 0.05, with Ce and Si fixed at 0.01 and 0.03, respectively. All cases were well defined by the YAG crystal structure (ICCD PDF# 00-033-0040), which takes the Ia-3d space group. Mn^{2+} addition in YAG (ionic radii of 0.67 Å and 0.96 Å for octahedral and dodecahedral coordination, respectively) has been reported to occupy both the octahedral Al site (r = 0.535 Å), as well as the dodecahedral Y site (r = 1.019 Å).[8.7.29-8.7.31] In this study, it was found that the dominant peak around 38.5º shifts to higher 2θ positions with increasing Mn^{2+} content (inset of Figure 8.1), which indicates a contracting lattice constant, confirmed by Rietveld refinement modelling summarized in Table 8.2. This suggests that Mn^{2+} preferentially occupies the dodecahedral Y site when used in glycothermal synthesis. This is likely due to the similarity of Y and Mn precursors used in this study, namely Y acetate and Mn^{2+} acetate. All dopants appeared

to be homogeneously distributed throughout the nanocrystal as shown by EDS elemental mapping in Figure 8.2, although a higher density of Mn ions can be seen in the core of Ce, 3% Mn, Si:YAG / YAG core/shell samples, shown in Appendix Figure 12.1a. The results of elemental compositional analysis obtained from EDS is summarized in Table 8.3. The elemental composition approached theoretical values with the addition of an intrinsic shell layer, further indicating an improvement in precursor inclusion. The presence of significant amounts of carbon is likely due to the carbon-coated copper TEM grid.

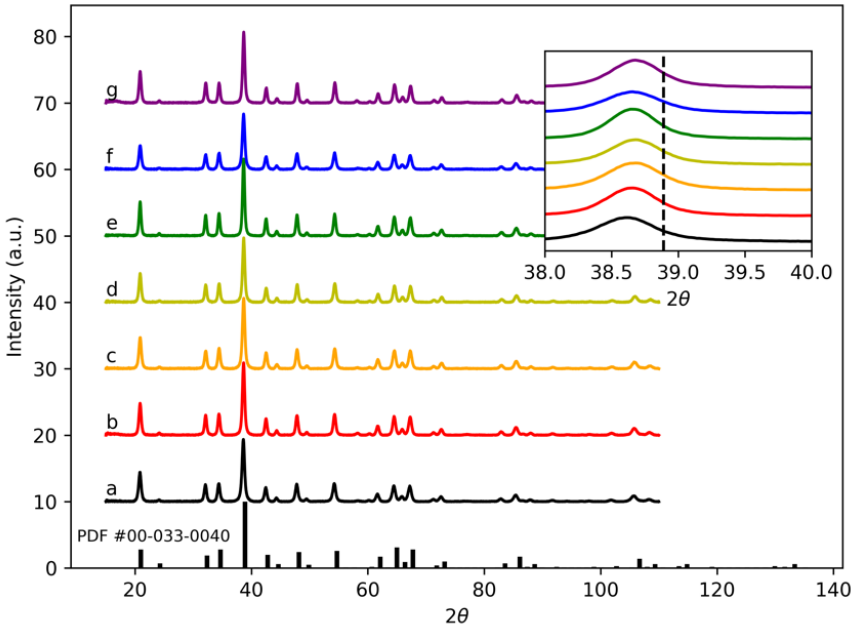

Figure 8.1: XRD spectra of dried $Ce_{0.03},Mn_xSi_y:Y_{2.97}Al_{(1-x-y)5}O_{12}$ *powders.*

a) *Ce:YAG b) Ce, 1% Mn:YAG, c) Ce, 3% Mn:YAG d) Ce, 5% Mn:YAG, e) Ce, 3% Mn, Si:YAG, f) 3% Mn, Si:YAG, g) Ce, 3% Mn, Si:YAG / YAG. Inset: Magnified view of 38.5° 2θ peak.*

	Ce:YAG	Ce, 1% Mn	Ce, 3% Mn	Ce, 5% Mn	Ce, 3% Mn, Si	3% Mn, Si	Ce, 3% Mn, Si / YAG
Lattice Constant (Å)	12.091	12.089	12.081	12.079	12.084	12.089	12.075
Crystallite Size (nm)	39.9	51.3	31.7	48.8	80.6	43.4	51.1

Table 8.2: Microstructure parameters obtained from Rietveld refinement with Le Bail fitting.

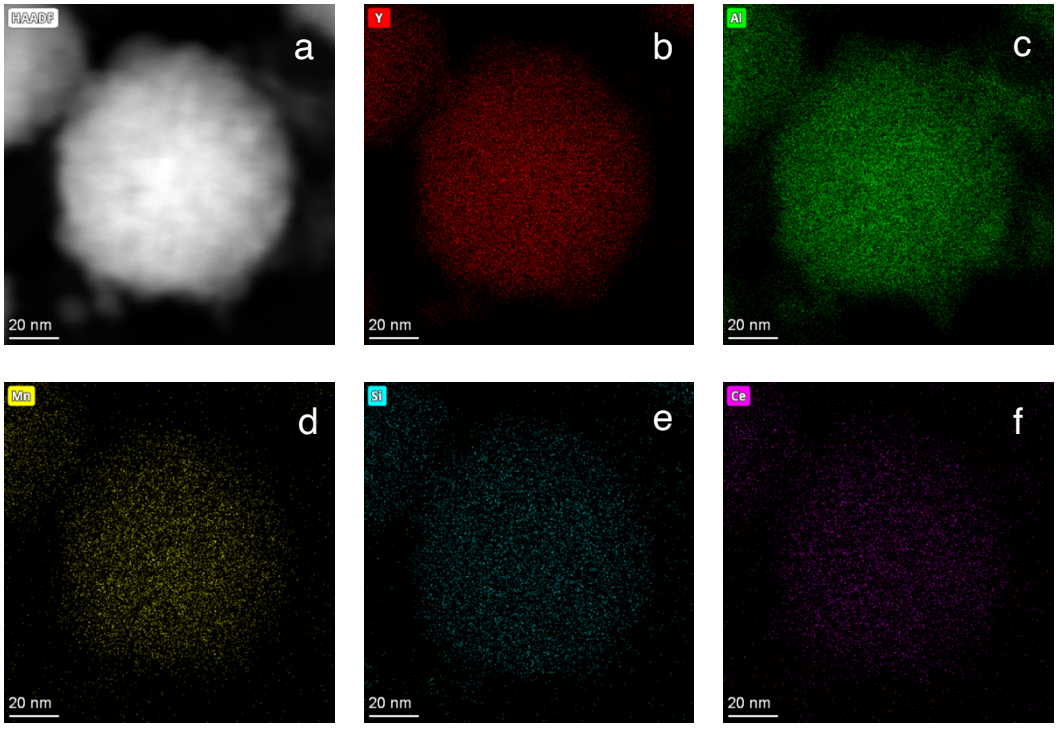

Figure 8.2: EDS mapping of Ce, 3% Mn, Si:YAG / YAG.

a) STEM image of area mapped. Elemental mapping of b) Y, c) Al, d) Mn, e) Si, f) Ce.

			Ce, 3% Mn, Si:YAG		Ce, 3% Mn, Si:YAG / YAG		Theoretical
Atomic Number	Element	Family	Atomic Fraction (%)	Atomic Error (%)	Atomic Fraction (%)	Atomic Error (%)	Atomic Fraction (%)
6	C	K	17.56	1.93	8.86	1.01	-
8	O	K	51.21	5.35	52.95	5.48	60
13	Al	K	16.67	3.25	17.57	3.44	24.25
25	Mn	K	0.66	0.13	0.93	0.18	0.75
39	Y	K	13.83	2.13	19.55	2.97	14.85
58	Ce	L	0.06	0.01	0.13	0.02	0.15

Table 8.3:EDS analysis of Ce, 3% Mn, Si:YAG and Ce, 3% Mn, Si:YAG / YAG nanophosphors.

Average particle size and size distribution was measured using TEM images of Ce, 3% Mn, Si:YAG and Ce, 3% Mn, Si:YAG / YAG nanoparticles shown in Figure 8.3 and Appendix Figure 12.2. It has been suggested that the glycothermal method produces platelets ~6-10 nm in size which then agglomerate into larger particles, which can be seen in the insets of Figure 8.3.[14-16,18] Particle size was found to be 56 ± 16 nm, 82 ± 14 nm, and 93 ± 26 nm for Ce:YAG (n = 262), Ce, 3% Mn, Si:YAG and Ce, 3% Mn, Si:YAG / YAG_samples (n = 137), respectively. The particles are stabilized by residual organic groups of the alkoxide precursors which remain on the particle surface after synthesis as evidenced by FTIR, shown in Appendix Figure 12.3.

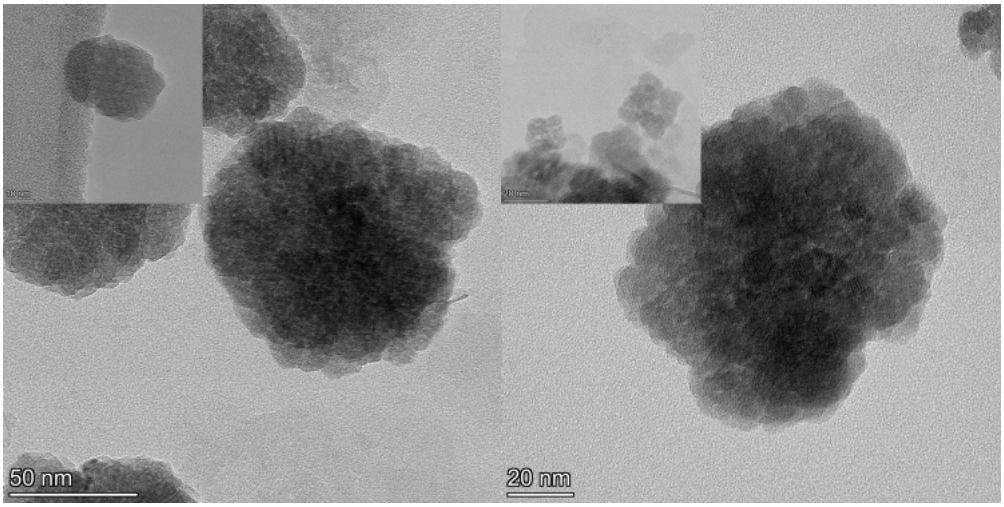

Figure 8.3:TEM images of left: Ce, 3% Mn, Si:YAG, right: Ce, 3% Mn, Si:YAG / YAG. Insets: high resolution TEM images depicting platelet formation (left inset scale bar 10 nm, right inset scale bar 20 nm).

NMR was used to determine the coordination of Al in the crystal, summarized in Figure 8.4. In the YAG lattice, Al takes both tetrahedral and octahedral symmetry, in a ratio of 3/2, respectively. SPE NMR was used to determine the Al^{IV}/Al^{VI} ratio in the whole crystal, while $^{1}H \rightarrow {}^{27}Al$ CP NMR was used to probe the crystal surface, as the only source of hydrogen would be due to hydrocarbons stabilizing the particle surface. Peaks around 0 ppm indicate octahedral symmetry, and those around ~35-80 ppm indicate tetrahedral symmetry. It was found that the Al^{IV}/Al^{VI} ratios of the samples containing Ce:YAG, Ce, 3% Mn, Si:YAG, and Ce, 3% Mn, Si:YAG / YAG were 0.25, 0.11, and 0.12, respectively, almost 10x less than the bulk value of 1.5. There was no evidence of tetrahedral coordination present on the particle surface.

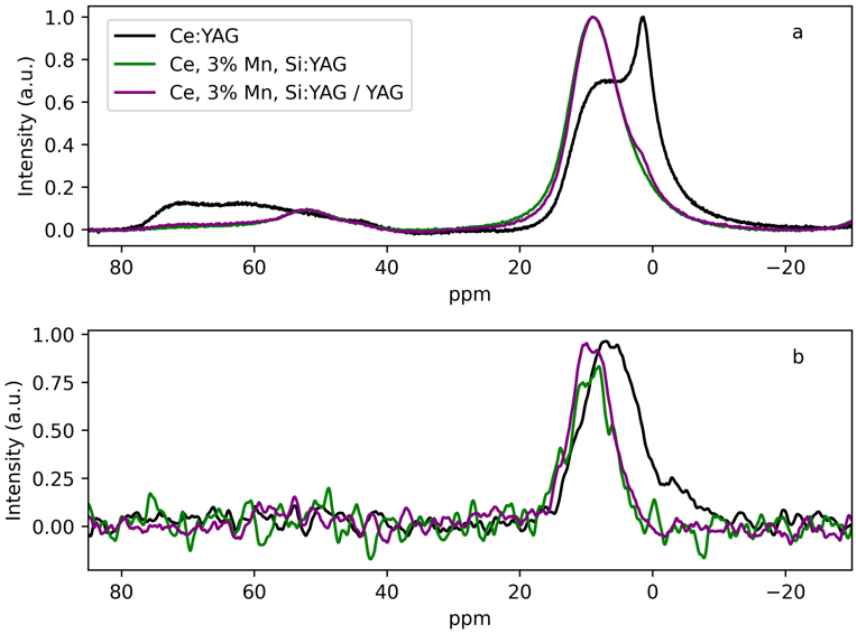

Figure 8.4: NMR spectra of Ce:YAG, Ce, 3% Mn, Si:YAG, and Ce, 3% Mn, Si:YAG / YAG samples.

a) Single pulse excitation scan. b) $^{1}H \rightarrow {}^{27}Al$ cross polarized scan. A Savitzky-Golay filter was applied to b).

Finally, the oxidation state of Mn and Ce dopants were verified after glycothermal synthesis using XPS, shown in Figure 8.5. A sample with the highest Mn content was chosen to increase the signal-to-noise ratio. The peak Mn $2p_{3/2}$ peak at 641 eV with a satellite feature suggests Mn exists in the MnO configuration and did not experience a change in oxidation state during the reaction. Moreover, the lack of a peak at 917 eV suggests that Ce (IV) oxide is not present, and thus Ce remained in the luminescent 3+ state. Glycol solvents have been shown to act as reducing agents during the glycothermal synthesis, however Mn^{2+} is particularly stable with its half-filled *d* orbital.[8.7.38-8.7.41]

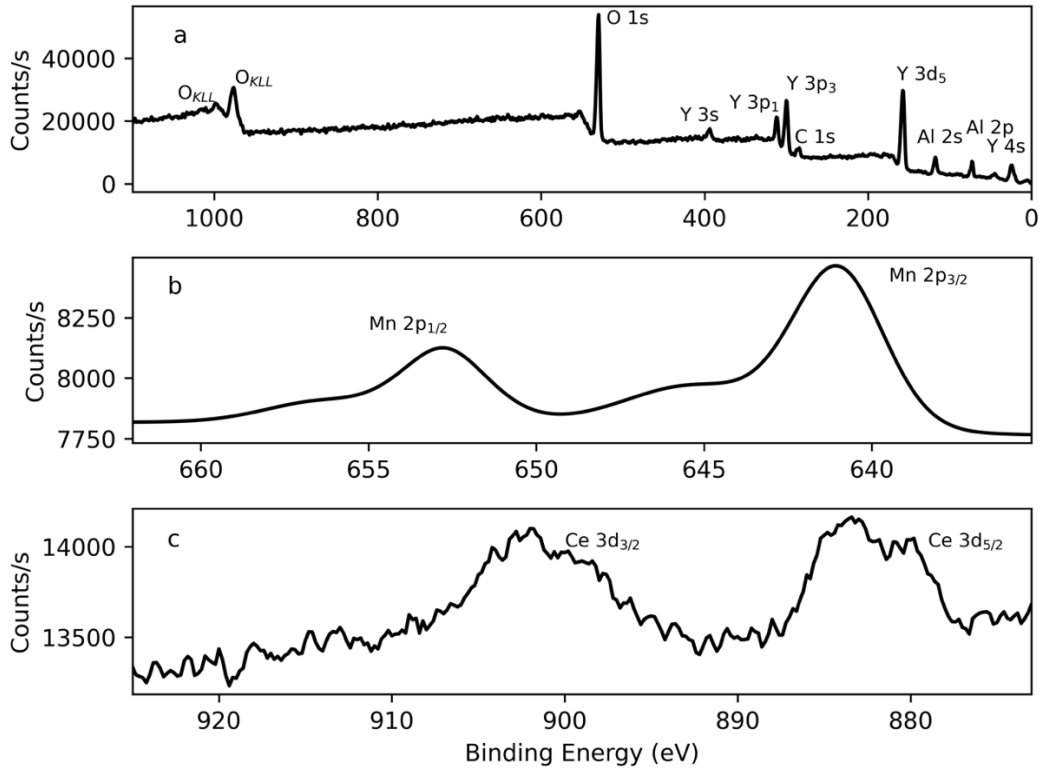

Figure 8.5: XPS spectra of Ce, 5% Mn:YAG.

a) Survey spectrum. b) Analysis of Mn. c) Analysis of Ce.

8.5.2. Luminescence of Mn^{2+} samples

Mn^{2+} has been shown to exhibit red luminescence, however, as the transition involves *d-d* energy states, the process is spin forbidden.[8.7.27-8.7.31, 8.7.36, 8.7.37, 8.7.42] Transitions can become possible when a crystal field is imposed on Mn^{2+} ions, particularly in octahedral symmetry, which are summarized in Figure 2.3 d) and shown in Appendix Figure 12.4. Figure 8.6a shows the results of luminescence testing of samples containing both Ce and Mn^{2+}. Mn^{2+} emission was seen at 594 nm, corresponding to the $^4T_1(^4G) \rightarrow {}^6A_1(^6S)$ transition. It was found that emission intensity increased from 1% to 3% before

quenching at 5% Mn. An equivalent amount of Si^{4+}, 3%, was added as a charge compensator, further improving the emission intensity. The linear relationship of the $^4T_1$ energy state on Δ/B as seen in Figure 2.3d indicates that the optical properties of Mn^{2+} are also dependent on the local crystal field strength. The results of comparing Ce, 3% Mn, Si:YAG with those grown with doped/intrinsic core/shell Ce, 3% Mn, Si:YAG / YAG samples are shown in Figure 8.6b. Extension of the YAG lattice by addition of a shell layer increased the overall emission intensity of Mn^{2+}, and photoluminescence quantum yield (PLQY) increased from 44% to 73% (PLQY of Ce:YAG nanophosphors as a control sample was 48%, as previously reported).[8.7.25] These findings are consistent with Mn^{2+} optical properties in octahedral coordination, however the results from structural analysis suggest that Mn^{2+} preferentially occupies the Y dodecahedral site. It is therefore concluded that while Mn^{2+} preferentially occupies the Y dodecahedral site, the atoms which do occupy Al sites likely reside in luminescent octahedral sites due to the ~10x increase in total number of octahedral sites available. Moreover, Mn^{2+} emission can be enhanced by use of an intrinsic YAG shell layer.

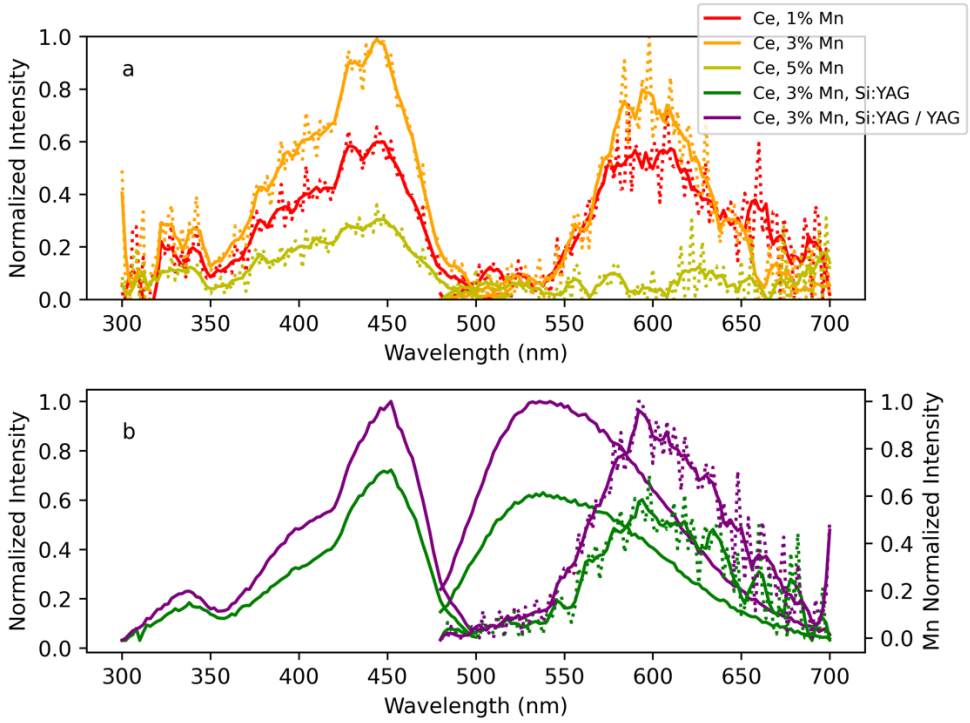

Figure 8.6: Luminescence of Ce and Mn^{2+} containing samples.

Excitation was 450 nm in all cases. a) PLE / PL characteristics of samples containing 1%, 3%, and 5% Mn^{2+} to find optimal Mn concentration. b) PLE / PL characteristics showing comparison of Ce, 3% Mn, Si:YAG and Ce, 3% Mn, Si:YAG / YAG doped/intrinsic core/shell sample. A lag time of 100 µs was introduced to collect Mn^{2+}emission data, shown by the dotted lines. Excitation spectra were monitored at 530 nm and 590 nm. A Savitzky-Golay filter was applied to Mn^{2+} emission spectra.

8.5.3. *Energy transfer of Ce to Mn^{2+}*

In order to investigate the energy transfer of Ce to Mn^{2+} in YAG, the fluorescence lifetime was measured, shown in Figure 8.7. The measured lifetimes were obtained by

fitting the decay curves using a non-linear least squares regression algorithm to the equation:

$$I(t) = \sum_{i=1}^{n} A_i \left(e^{-t/\tau_i} \right)$$

The commercial bulk phosphor was well fitted with a mono-exponential, showing a fluorescence lifetime of 68.9 ns, which is close to reported literature values. [8.7.43, 8.7.44] The nanocrystalline Ce:YAG lifetimes were fit to bi-exponentials due to the increase in nonradiative processes that produced strong quenching of the nanocrystal lifetime.[8.7.45, 8.7.46] The resulting measurements gave lifetimes of 101.1 ns (τ_1) and 21.8ns (τ_2), corresponding to nanocrystal radiative and non-radiative process, respectively. The increased lifetime of nanocrystal Ce:YAG matches literature of the local field effects on nanocrystal radiative lifetime due to Fermi's golden rule.[8.7.16, 8.7.47-8.7.49] Meanwhile the intrinsic presence and increased proportion of surface defects provides an explanation for the quenching of the nanocrystal lifetime observed.[8.7.14] For this discussion, the lifetime of the nanocrystalline samples will refer only to the first component of lifetime decay (τ_1).

Samples containing both Ce and Mn show a further reduction in lifetime, 92.7 ns for Ce, 3% Mn, Si:YAG, and 90.7 ns for Ce, 3% Mn, Si:YAG / YAG, while the weight of (τ_2) nearly doubles for both powders. This is indicative of the presence of non-radiative energy transfer from Ce to Mn^{2+}.[8.7.29, 8.7.50] It is unlikely that this is due to metal-metal charge transfer, as no change in oxidation state was observed for either ion as evidenced by XPS in Figure 8.5. Rather, the energy of the spin allowed 5*d* → 4*f* transition of Ce can

be transferred to Mn^{2+} non-radiatively via dipole-quadrupole interactions as demonstrated in previous reporting.[8.7.29, 8.7.30, 8.7.50]

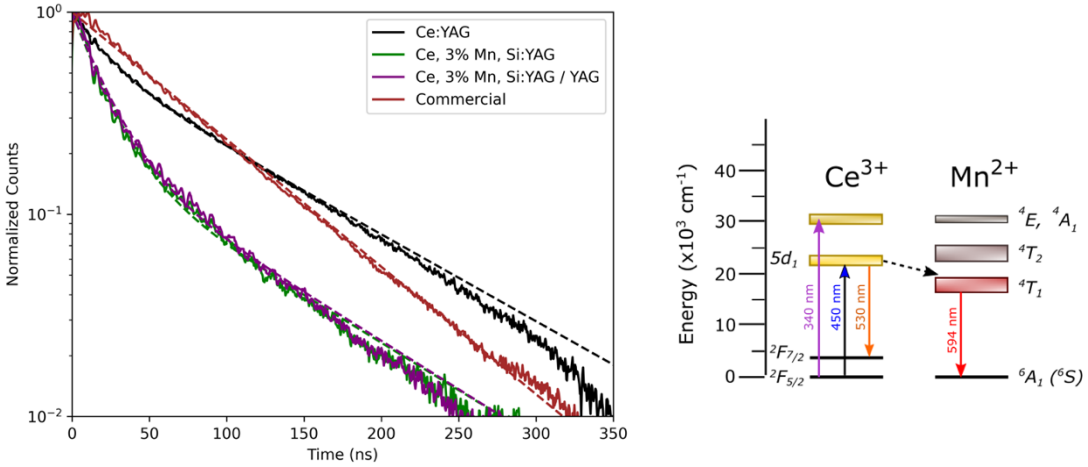

Figure 8.7: Fluorescence lifetime measurements of Ce:YAG; Ce, 3% Mn, Si:YAG;, and Ce, 3% Mn, Si:YAG / YAG samples.

Left: Measured fluorescence decay. Bulk commercial Ce:YAG is fitted with a mono-exponential fit, and nanocrystalline samples are fitted with a bi-exponential fit. Right: Schematic depicting the energy transfer of Ce to Mn^{2+}.

Sample	**τ_1 (ns)**	A_1	**τ_2 (ns)**	A_2
Ce:YAG	**101.1**	0.574	**21.8**	0.426
Ce, 3% Mn, Si:YAG	**92.7**	0.200	**18.2**	0.800
Ce, 3% Mn, Si:YAG / YAG	**90.7**	0.215	**19.0**	0.785
Commercial	**68.9**	-	**-**	-

Table 8.4: Summary of fluorescence lifetimes and fit parameters.

8.6. Conclusion

Mn (II) acetate was shown to be a suitable precursor for Mn^{2+} doping of YAG using the glycothermal method. The use of Mn (II) acetate yielded preferential occupation of Mn in the Y site. However, optical transitions of Mn^{2+} in octahedrally coordinated Al sites were observed due to a relatively high doping level and an abundance of octahedral Al sites formed during glycothermal synthesis. The intensity of these transitions improved with the addition of Si^{4+} as a charge compensator and growth of an intrinsic YAG shell layer. It was shown that Mn (II) acetate does not undergo a change of valence state during the glycothermal reaction. It was also shown that the spin-allowed transitions of Ce act as an effective sensitizer for Mn^{2+}, and non-radiative energy transfer was demonstrated.

8.7. References

8.7.1 Liu, G. H., Zhou, Z. Z., Shi, Y., Liu, Q., Wan, J. Q., & Pan, Y. B. (2015). Ce: YAG transparent ceramics for applications of high power LEDs: Thickness effects and high temperature performance. *Materials Letters*, *139*, 480-482.

8.7.2 Fujita, S., Yoshihara, S., Sakamoto, A., Yamamoto, S., & Tanabe, S. (2005, September). YAG glass-ceramic phosphor for white LED (I): background and development. In *Fifth International Conference on Solid State Lighting* (Vol. 5941, p. 594111). International Society for Optics and Photonics.

8.7.3 Shen, X., Zhang, D. F., Fan, X. W., Hu, G. S., Bian, X. B., & Yang, L. (2016). Fabrication and characterization of YAG: Ce phosphor films for white LED

applications. *Journal of Materials Science: Materials in Electronics*, *27*(1), 976-981.

8.7.4 Schlotter, P., Baur, J., Hielscher, C., Kunzer, M., Obloh, H., Schmidt, R., & Schneider, J. (1999). Fabrication and characterization of GaN/InGaN/AlGaN double heterostructure LEDs and their application in luminescence conversion LEDs. *Materials Science and Engineering: B*, *59*(1-3), 390-394.

8.7.5 Uchida, Y., Setomoto, T., Taguchi, T., Nakagawa, Y., & Miyazaki, K. (2000). Characteristics of high-efficiency InGaN-based white LED lighting. In *Display Technologies III* (Vol. 4079, pp. 120-126). International Society for Optics and Photonics.

8.7.6 Hu, S., Lu, C., Zhou, G., Liu, X., Qin, X., Wang, S., & Xu, Z. (2016). Transparent YAG: Ce ceramics for WLEDs with high CRI: Ce^{3+} concentration and sample thickness effects. *Ceramics international*, *42*(6), 6935-6941.

8.7.7 Ma, C., Cao, Y., Shen, X., Wen, Z., Ma, R., Long, J., & Yuan, X. (2017). High reliable and chromaticity-tunable flip-chip w-LEDs with Ce: YAG glass-ceramics phosphor for long-lifetime automotive headlights applications. *Optical Materials*, *69*, 105-114.

8.7.8 Veith, M., Mathur, S., Kareiva, A., Jilavi, M., Zimmer, M., & Huch, V. (1999). Low temperature synthesis of nanocrystalline $Y_3Al_5O_{12}$ (YAG) and Ce-doped $Y_3Al_5O_{12}$ via different sol–gel methods. *Journal of Materials Chemistry*, *9*(12), 3069-3079.

8.7.9 Xia, G., Zhou, S., Zhang, J., & Xu, J. (2005). Structural and optical properties of YAG: Ce^{3+} phosphors by sol–gel combustion method. *Journal of Crystal Growth*, *279*(3-4), 357-362.

8.7.10 Yuan, F., & Ryu, H. (2004). Ce-doped YAG phosphor powders prepared by co-precipitation and heterogeneous precipitation. *Materials Science and Engineering: B*, *107*(1), 14-18.

8.7.11 Zhang, K., Liu, H. Z., Wu, Y. T., & Hu, W. B. (2008). Co-precipitation synthesis and luminescence behavior of Ce-doped yttrium aluminum garnet (YAG: Ce) phosphor: The effect of precipitant. *Journal of alloys and compounds*, *453*(1-2), 265-270.

8.7.12 Li, X., Liu, H., Wang, J., Cui, H., & Han, F. (2004). YAG: Ce nano-sized phosphor particles prepared by a solvothermal method. *Materials Research Bulletin*, *39*(12), 1923-1930.

8.7.13 Lin, W. T., & Wu, Y. C. (2015). One-pot synthesis of submicrometer-sized Ce: YAG spherical particles by solvothermal process using alcohol solvents. *Journal of the American Ceramic Society*, *98*(9), 2754-2759.

8.7.14 Kasuya, R., Isobe, T., & Kuma, H. (2006). Glycothermal synthesis and photoluminescence of YAG: Ce^{3+} nanophosphors. *Journal of alloys and compounds*, *408*, 820-823.

8.7.15 Isobe, T. (2012). Glycothermally synthesized YAG: Ce^{3+} nanophosphors for blue LEDs. *ECS Journal of Solid State Science and Technology*, *2*(2), R3012.

8.7.16 Odziomek, M., Chaput, F., Lerouge, F., Sitarz, M., & Parola, S. (2017). Highly luminescent YAG: Ce ultra-small nanocrystals, from stable dispersions to thin films. *Journal of Materials Chemistry C*, *5*(47), 12561-12570.

8.7.17 Ganguly, S., Das, P., Banerjee, S., & Das, N. C. (2019). Advancement in science and technology of carbon dot-polymer hybrid composites: a review. *Functional Composites and Structures*, *1*(2), 022001.

8.7.18 Kasuya, R., Isobe, T., Kuma, H., & Katano, J. (2005). Photoluminescence enhancement of PEG-modified YAG: Ce^{3+} nanocrystal phosphor prepared by glycothermal method. *The Journal of Physical Chemistry B*, *109*(47), 22126-22130.

8.7.19 Revaux, A., Dantelle, G., George, N., Seshadri, R., Gacoin, T., & Boilot, J. P. (2011). A protected annealing strategy to enhanced light emission and photostability of YAG: Ce nanoparticle-based films. *Nanoscale*, *3*(5), 2015-2022.

8.7.20 Peter, S., Patel, A., & Kitai, A. (2019). Photoluminescence enhancement of Ce: YAG nanophosphors via doped/intrinsic core/shell structures. *Journal of Luminescence*, *211*, 82-87.

8.7.21 Pan, Y. X., Wang, W., Liu, G. K., Skanthakumar, S., Rosenberg, R. A., Guo, X. Z., & Li, K. K. (2009). Correlation between structure variation and luminescence red shift in YAG: Ce. *Journal of Alloys and Compounds*, *488*(2), 638-642.

8.7.22 Chen, J., Deng, Z., Liu, Z., Lin, Y., Lan, H., Chen, D., ... & Cao, Y. (2015). Optical enhancement brought by doping Gd^{3+} ions into Ce: YAG ceramics for indoor white light-emitting diodes. *Optics express*, *23*(7), A292-A298.

8.7.23 Chawla, S., Roy, T., Majumder, K., & Yadav, A. (2014). Red enhanced YAG: Ce, Pr nanophosphor for white LEDs. *Journal of Experimental Nanoscience*, *9*(8), 776-784.

8.7.24 Du, Q., Feng, S., Qin, H., Hua, H., Ding, H., Jia, L., ... & Jiang, H. (2018). Massive red-shifting of Ce^{3+} emission by Mg^{2+} and Si^{4+} doping of YAG: Ce transparent ceramic phosphors. *Journal of Materials Chemistry C*, *6*(45), 12200-12205.

8.7.25 Peter, S., Fitzpatrick, M., & Kitai, A. (2021). Glycothermal synthesis and photoluminescence of Mg–Si modified Ce: YAG nanophosphors. *Nanoscale Advances*, *3*(10), 2911-2917.

8.7.26 Pan, Y., Wu, M., & Su, Q. (2004). Tailored photoluminescence of YAG: Ce phosphor through various methods. *Journal of Physics and Chemistry of Solids*, *65*(5), 845-850.

8.7.27 Ling, J., Zhou, Y., Xu, W., Lin, H., Lu, S., Wang, B., & Wang, K. (2020). Red-emitting YAG: Ce, Mn transparent ceramics for warm WLEDs application. *Journal of Advanced Ceramics*, *9*(1), 45-54.

8.7.28 Ma, Y., Zhang, L., Zhou, T., Sun, B., Wang, Y., Kang, J., ... & Chen, H. (2020). High recorded color rendering index in single Ce,(Pr, Mn): YAG transparent ceramics for high-power white LEDs/LDs. *Journal of Materials Chemistry C*, *8*(13), 4329-4337.

8.7.29 Jia, Y., Huang, Y., Zheng, Y., Guo, N., Qiao, H., Zhao, Q., ... & You, H. (2012). Color point tuning of $Y_3Al_5O_{12}$: Ce^{3+} phosphor via Mn^{2+}–Si^{4+} incorporation for white light generation. *Journal of Materials Chemistry*, *22*(30), 15146-15152.

8.7.30 Gu, G., Xiang, W., Yang, C., & Liang, X. (2015). Synthesis and luminescence properties of a H_2 annealed Mn-doped $Y_3Al_5O_{12}$: Ce^{3+} single crystal for WLEDs. *CrystEngComm*, *17*(24), 4554-4561.

8.7.31 Wang, B., Ling, J., Zhou, Y., Xu, W., Lin, H., Lu, S., ... & Hong, M. (2019). YAG: Ce^{3+}, Mn^{2+} transparent ceramics prepared by gel-casting for warm white LEDs. *Journal of Luminescence*, *213*, 421-426.

8.7.32 Wang, W., Tang, J., Hsu, S. T. V., Wang, J., & Sullivan, B. P. (2008). Energy transfer and enriched emission spectrum in Cr and Ce co-doped $Y_3Al_5O_{12}$ yellow phosphors. *Chemical Physics Letters*, *457*(1-3), 103-105.

8.7.33 Yi, X., Zhou, S., Chen, C., Lin, H., Feng, Y., Wang, K., & Ni, Y. (2014). Fabrication of Ce: YAG, Ce, Cr: YAG and Ce: YAG/Ce, Cr: YAG dual-layered composite phosphor ceramics for the application of white LEDs. *Ceramics International*, *40*(5), 7043-7047.

8.7.34 Yang, H., & Kim, Y. S. (2008). Energy transfer-based spectral properties of Tb-, Pr-, or Sm-codoped YAG: Ce nanocrystalline phosphors. *Journal of Luminescence*, *128*(10), 1570-1576.

8.7.35 Ali, H., & Khedr, M. A. (2019). Energy transfer between Ce and Sm co-doped YAG nanocrystals for white light emitting devices. *Results in Physics*, *12*, 1777-1782.

8.7.36 Li, Y., Qi, S., Li, P., & Wang, Z. (2017). Research progress of Mn doped phosphors. *RSC advances*, *7*(61), 38318-38334.

8.7.37 Kumari, P., & Dwivedi, Y. (2017). Investigation of bright red emitting Mn doped aluminum silicate nanophosphor. *Materials Research Bulletin*, *88*, 266-271.

8.7.38 Beshkar, F., Khojasteh, H., & Salavati-Niasari, M. (2017). Flower-like CuO/ZnO hybrid hierarchical nanostructures grown on copper substrate: glycothermal synthesis, characterization, hydrophobic and anticorrosion properties. *Materials*, *10*(7), 697.

8.7.39 Fu, H., Jiang, X., Yang, X., Yu, A., Su, D., & Wang, G. (2012). Glycothermal synthesis of assembled vanadium oxide nanostructures for gas sensing. *Journal of nanoparticle Research*, *14*(6), 1-14.

8.7.40 Zhu, H., Zhang, Z., & Jiang, X. (2020). Glycothermal synthesis of VO2 (B) nanoparticles for gas sensing application. *Journal of nanoscience and nanotechnology*, *20*(3), 1946-1954.

8.7.41 Cho, S. B., Noh, J. S., Park, S. J., Lim, D. Y., & Choi, S. H. (2007). Morphological control of Fe_3O_4 particles via glycothermal process. *Journal of materials science*, *42*(13), 4877-4886.

8.7.42 Shionoya, S., Yen, W. M., & Yamamoto, H. (Eds.). (2018). *Phosphor handbook*. CRC press.

8.7.43 Lyu, L. J., & Hamilton, D. S. (1991). Radiative and nonradiative relaxation measurements in Ce^{3+} doped crystals. *Journal of luminescence*, *48*, 251-254.

8.7.44 Arjoca, S., Víllora, E. G., Inomata, D., Aoki, K., Sugahara, Y., & Shimamura, K. (2015). Temperature dependence of Ce: YAG single-crystal phosphors for high-brightness white LEDs/LDs. *Materials Research Express*, *2*(5), 055503.

8.7.45 Yang, L., Li, L., Zhao, M., & Li, G. (2012). Size-induced variations in bulk/surface structures and their impact on photoluminescence properties of $GdVO_4$: Eu^{3+} nanoparticles. *Physical Chemistry Chemical Physics*, *14*(28), 9956-9965.

8.7.46 Li, H., Luo, N., Luo, D., Xiong, L., Yang, L., & Zhao, M. (2021). Effect of calcination temperature on the microstructure and optical properties of monodispersed self-assembled yttrium orthovanadate microspheres. *Journal of Luminescence*, *234*, 117990.

8.7.47 Meltzer, R. S., Feofilov, S. P., Tissue, B., & Yuan, H. B. (1999). Dependence of fluorescence lifetimes of Y_2O_3: Eu^{3+} nanoparticles on the surrounding medium. Physical Review B, 60(20), R14012.

8.7.48 Toptygin, D. (2003). Effects of the solvent refractive index and its dispersion on the radiative decay rate and extinction coefficient of a fluorescent solute. *Journal of Fluorescence*, *13*(3), 201-219.

8.7.49 Senden, T., Rabouw, F. T., & Meijerink, A. (2015). Photonic effects on the radiative decay rate and luminescence quantum yield of doped nanocrystals. ACS nano, 9(2), 1801-1808.

8.7.50 Sontakke, A. D., van Bunningen, A. J., Rabouw, F. T., Meijers, S., & Meijerink, A. (2020). Unraveling the $Eu^{2+} \rightarrow Mn^{2+}$ energy transfer mechanism in w-LED phosphors. *The Journal of Physical Chemistry C*, *124*(25), 13902-13911.

Chapter 9: Conclusions

Strategies for improving the optical properties of Ce:YAG nanophosphors synthesized using the glycothermal method have been presented. The local crystal environment of Ce directly influences its optical properties, and as such, the tuning of this local environment forms the basis of this thesis. Enhancement of important features such as overall luminescence output, absorption and emission spectra, and photoluminescence quantum yield have been demonstrated through techniques such as the growth of an intrinsic shell layer, as well as the addition of various transition metals to adjust the luminescence properties. It has been shown experimentally that the glycothermal method is an effective means of the achieving these desired characteristics, as a solution-based approach increases the homogeneous distribution of dopant atoms without the need for an annealing step. In addition, the growth of Ce:YAG in solution facilitates the separation of particle growth into a two-step process for a core/shell architecture, with Ce localized to the core. Shell thickness was controlled by the addition of additional precursor material to the reaction chamber in an amount relative to the initial precursor concentration, denoted as the shell-to-seed ratio (SSR). Sub-200 nm particles were formed with a shell-to-seed ratio of 1:1. It was also shown that Ce:YAG grown using the glycothermal method exhibits a high density of defects in the form of Al in octahedral coordination, particularly on the particle surface. The concentration of octahedral Al was found to be ~10x higher than bulk Ce:YAG.

The local crystal field was then modified using Mg-Si pair addition, which was capable of exhibiting a 40 nm blueshift in Ce:YAG absorption. A study of the glycothermal

precursor behavior at elevated temperature showed that a more uniform cleavage of organic ligands can be achieved at temperatures slightly higher than the standard reaction temperature (315 ºC vs 300 ºC), which led to increased photoluminescence quantum yield (PLQY). This increase was attributed to a higher degree of precursor dispersion in the crystal, as the glycothermal reaction kinetics increases upon precursor ligand cleavage.

Finally, the red component of Ce:YAG emission was improved with the addition of Mn^{2+} as a co-dopant. Transition metal luminescence can be observed when the luminescent ion takes octahedral coordination, although it was found that Mn^{2+} preferentially occupies the dodecahedral Y site, which was attributed to the chemical similarity of the Mn^{2+} and Y precursors. However, octahedral Mn^{2+} emission was still observed, suggesting that the Mn which does occupy an Al site is well supported for luminescence due to the high concentration of octahedral Al sites from glycothermal defects. A 3% concentration of Mn^{2+} was found to perform better than 1%, with quenching observed at 5%. The Mn^{2+} luminescence was found to improve with the addition of Si^{4+} as a charge compensator, and improved further with the use of a doped/intrinsic core/shell architecture. The fluorescence lifetime of Ce and Mn^{2+} co-doped nanophosphors was measured using a purpose built single photon counting setup. A reduction in fluorescence lifetime was observed for Mn^{2+} containing samples, providing evidence of faster, non-radiative energy transfer pathways from Ce to Mn^{2+}. Moreover, the intensity of Mn^{2+} emission increased significantly when co-doped with Ce, which demonstrates that the allowed $4f \rightarrow 5d$ transition of Ce acts as an effective sensitizer for Mn^{2+}. The PLQY of Ce and Mn^{2+} samples containing an intrinsic shell layer increased to 73%, higher than the

increase from increasing the reaction temperature from 300 ºC to 315 ºC. This indicates that the defects on the particle surface are the most detrimental to Ce:YAG based nanophosphor luminescence, and the physical separation of the dopant ions from the defective surface should be the highest priority.

Chapter 10: Future Work

Much of the focus of this research was on developing strategies to adjust the material properties of Ce:YAG based nanophosphors with the end goal of improving factors such as overall light emission intensity and photometric quality. Regretfully, the prioritization of the chemistry of synthesis left little time for device fabrication. However, the study on post-synthesis surface modification discussed in Chapter 7.5 opens the door to a wide range of applications for the optimized Ce:YAG nanophosphors developed in this body of work. A significant advantage of bottom-up nanoparticle synthesis is that the crystal mostly consists of the surface, which can be functionalized to tailor any number of applications. For example, the same Ce:YAG nanophosphor could potentially be encapsulated in a gel-like polymer for flexible transparent displays, or dispersed in water for use as a bio-compatible fluorescent material simply by adjusting the surface capping material.

Additionally, the high concentration of octahedral sites present when using glycothermal synthesis can be leveraged by many more luminescent transition metal ions than just the Mn^{2+} explored in this work. Chromium is a promising candidate, as well as other valences of Mn, such as Mn^{4+}. Significant effort was made to incorporate Mn^{4+} as a co-dopant, however control over the Mn oxidation state proved to be difficult. This may be an interesting challenge with high impact for a more experienced chemist.

Chapter 11: References

The references listed in this chapter pertain to the citations cited in chapters 1-5, as the works cited in chapters 6-8 are contained in those chapters.

1. Chen, J., Yan, H., Kuwabara, A., Smith, M. D., Iwasa, Y., Ogino, H., ... & Zur Loye, H. C. (2020). Flux Crystal Growth, Crystal Structure, and Optical Properties of New Germanate Garnet $Ce_2CaMg_2Ge_3O_{12}$. *Frontiers in chemistry*, *8*, 91.
2. Vosegaard, T., Byriel, I. P., Pawlak, D. A., Wozniak, K., & Jakobsen, H. J. (1998). Crystal structure studies on the garnet $Y_3Al_5O_{12}$ by ^{27}Al single-crystal NMR spectroscopy. *Journal of the American Chemical Society*, *120*(31), 7900-7904.
3. Massiot, D., Bessada, C., Coutures, J. P., & Taulelle, F. (1990). A quantitative study of ^{27}Al MAS NMR in crystalline YAG. *Journal of Magnetic Resonance (1969)*, *90*(2), 231-242.
4. Alahraché, S., Deschamps, M., Lambert, J., Suchomel, M. R., De Sousa Meneses, D., Matzen, G., ... & Allix, M. (2011). Crystallization of Y_2O_3–Al_2O_3 rich glasses: synthesis of YAG glass-ceramics. *The Journal of Physical Chemistry C*, *115*(42), 20499-20506.
5. Xu, Y. N., & Ching, W. Y. (1999). Electronic structure of yttrium aluminum garnet ($Y_3Al_5O_{12}$). *Physical Review B*, *59*(16), 10530.
6. Ikesue, A. (2002). Polycrystalline Nd: YAG ceramics lasers. *Optical materials*, *19*(1), 183-187.

7. Ikesue, A., Yoshida, K., Yamamoto, T., & Yamaga, I. (1997). Optical scattering centers in polycrystalline Nd: YAG laser. *Journal of the American Ceramic Society*, *80*(6), 1517-1522.
8. Ge, L., Li, J., Zhou, Z., Qu, H., Dong, M., Zhu, Y., ... & Guo, J. (2014). Fabrication of composite YAG/Nd: YAG/YAG transparent ceramics for planar waveguide laser. *Optical Materials Express*, *4*(5), 1042-1049.
9. Österberg, U., & Margulis, W. (1986). Dye laser pumped by Nd: YAG laser pulses frequency doubled in a glass optical fiber. *Optics letters*, *11*(8), 516-518.
10. Yang, P., Deng, P., & Yin, Z. (2002). Concentration quenching in Yb: YAG. *Journal of luminescence*, *97*(1), 51-54.
11. Fan, T. Y. (1993). Heat generation in Nd: YAG and Yb: YAG. *IEEE Journal of Quantum Electronics*, *29*(6), 1457-1459.
12. Kinsman, K. M., McKittrick, J., Sluzky, E., & Hesse, K. (1994). Phase development and luminescence in chromium-doped yttrium aluminum garnet (YAG: Cr) phosphors. *Journal of the American Ceramic Society*, *77*(11), 2866-2872.
13. Okhrimchuk, A. G., & Shestakov, A. V. (1994). Performance of YAG: Cr^{4+} laser crystal. *Optical materials*, *3*(1), 1-13.
14. Chen, D., Zhou, Y., Xu, W., Zhong, J., Ji, Z., & Xiang, W. (2016). Enhanced luminescence of Mn^{4+}: $Y_3Al_5O_{12}$ red phosphor via impurity doping. *Journal of Materials Chemistry C*, *4*(8), 1704-1712.

15. Jia, Y., Huang, Y., Zheng, Y., Guo, N., Qiao, H., Zhao, Q., ... & You, H. (2012). Color point tuning of $Y_3Al_5O_{12}$: Ce^{3+} phosphor via Mn^{2+}–Si^{4+} incorporation for white light generation. *Journal of Materials Chemistry*, *22*(30), 15146-15152.
16. Trejgis, K., & Marciniak, L. (2018). The influence of manganese concentration on the sensitivity of bandshape and lifetime luminescent thermometers based on $Y_3Al_5O_{12}$:Mn^{3+}, Mn^{4+}, Nd^{3+} nanocrystals. *Physical Chemistry Chemical Physics*, *20*(14), 9574-9581.
17. Robertson, J. M., & Van Tol, M. W. (1980). Epitaxially grown monocrystalline garnet cathode-ray tube phosphor screens. *Applied Physics Letters*, *37*(5), 471-472.
18. Kvapil, J., Kvapil, J., Blažek, K., Zikmund, J., Autrata, R., & Schauer, P. (1980). The luminescence efficiency of YAG: Ce phosphors. *Czechoslovak Journal of Physics B*, *30*(2), 185-192.
19. Kvapil, J., Kvapil, J., Manek, B., Perner, B., Autrata, R., & Schauer, P. (1981). Czochralski growth of YAG: Ce in a reducing protective atmosphere. *Journal of Crystal Growth*, *52*, 542-545.
20. Hoffman, M. V. (1977). Improved color rendition in high pressure mercury vapor lamps. *Journal of the Illuminating Engineering Society*, *6*(2), 89-91.
21. Wyner, E. F., & Daigneault, A. J. (1980). Improved mercury lamp for low color temperature applications. *Journal of the Illuminating Engineering Society*, *9*(2), 109-114.
22. Nishiura, S., Tanabe, S., Fujioka, K., Fujimoto, Y., & Nakatsuka, M. (2009). Preparation and optical properties of transparent Ce: YAG ceramics for high power

white LED. In *IOP Conference Series: Materials Science and Engineering* (Vol. 1, No. 1, p. 012031). IOP Publishing.

23. Nishiura, S., Tanabe, S., Fujioka, K., & Fujimoto, Y. (2011). Properties of transparent Ce: YAG ceramic phosphors for white LED. *Optical Materials*, *33*(5), 688-691.
24. Zhang, R., Lin, H., Yu, Y., Chen, D., Xu, J., & Wang, Y. (2014). A new-generation color converter for high-power white LED: transparent Ce^{3+}: YAG phosphor-in-glass. *Laser & Photonics Reviews*, *8*(1), 158-164.
25. Laaperi, A. (2008). OLED lifetime issues from a mobile-phone-industry point of view. *Journal of the Society for Information Display*, *16*(11), 1125-1130.
26. Kwon, S. K., Baek, J. H., Choi, H. C., Kim, S. K., Lampande, R., Pode, R., & Kwon, J. H. (2019). Degradation of OLED performance by exposure to UV irradiation. *RSC Advances*, *9*(72), 42561-42568.
27. Choi, H. W., Jeon, C. W., Dawson, M. D., Edwards, P. R., & Martin, R. W. (2003). Fabrication and performance of parallel-addressed InGaN micro-LED arrays. *IEEE Photonics Technology Letters*, *15*(4), 510-512.
28. Song, Z., Liao, J., Ding, X., Liu, X., & Liu, Q. (2013). Synthesis of YAG phosphor particles with excellent morphology by solid state reaction. *Journal of crystal growth*, *365*, 24-28.
29. Ghrib, T., Al-Otaibi, A. L., Almessiere, M. A., Ashahri, A., & Masoudi, I. (2017). Structural, optical and thermal properties of the Ce doped YAG synthesized by solid state reaction method. *Thermochimica Acta*, *654*, 35-39.

30. Adschiri, T., Hakuta, Y., & Arai, K. (2000). Hydrothermal synthesis of metal oxide fine particles at supercritical conditions. *Industrial & engineering chemistry research*, *39*(12), 4901-4907.
31. Yang, H., Yuan, L., Zhu, G., Yu, A., & Xu, H. (2009). Luminescent properties of YAG: Ce^{3+} phosphor powders prepared by hydrothermal-homogeneous precipitation method. *Materials Letters*, *63*(27), 2271-2273.
32. McMillen, C. D., Mann, M., Fan, J., Zhu, L., & Kolis, J. W. (2012). Revisiting the Hydrothermal growth of YAG. *Journal of crystal growth*, *356*, 58-64.
33. Zhang, X., Liu, H., He, W., Wang, J., Li, X., & Boughton, R. I. (2005). Novel synthesis of YAG by solvothermal method. *Journal of Crystal growth*, *275*(1-2), e1913-e1917.
34. Li, X., Liu, H., Wang, J., Cui, H., Han, F., & Boughton, R. I. (2004). Production of nanosized YAG powders with spherical morphology and nonaggregation via a solvothermal method. *Journal of the American Ceramic Society*, *87*(12), 2288-2290.
35. Dantelle, G., Testemale, D., Homeyer, E., Cantarano, A., Kodjikian, S., Dujardin, C., ... & Ibanez, A. (2018). A new solvothermal method for the synthesis of size-controlled YAG: Ce single-nanocrystals. *RSC advances*, *8*(47), 26857-26870.
36. Ramanujam, P., Vaidhyanathan, B., Binner, J., Ghanizadeh, S., Zhou, Z., & Spacie, C. (2018). Rapid synthesis of nanocrystalline YAG via microwave-assisted solvothermal process. *Journal of the American Ceramic Society*, *101*(11), 4864-4869.

37. Odziomek, M., Chaput, F., Lerouge, F., Sitarz, M., & Parola, S. (2017). Highly luminescent YAG: Ce ultra-small nanocrystals, from stable dispersions to thin films. *Journal of Materials Chemistry C*, *5*(47), 12561-12570.
38. Beshkar, F., Khojasteh, H., & Salavati-Niasari, M. (2017). Flower-like CuO/ZnO hybrid hierarchical nanostructures grown on copper substrate: glycothermal synthesis, characterization, hydrophobic and anticorrosion properties. *Materials*, *10*(7), 697.
39. Kasuya, R., Isobe, T., Kuma, H., & Katano, J. (2005). Photoluminescence enhancement of PEG-modified YAG:Ce^{3+} nanocrystal phosphor prepared by glycothermal method. *The Journal of Physical Chemistry B*, *109*(47), 22126-22130.
40. Kasuya, R., Isobe, T., & Kuma, H. (2006). Glycothermal synthesis and photoluminescence of YAG: Ce^{3+} nanophosphors. *Journal of alloys and compounds*, *408*, 820-823.
41. Kamiyama, Y., Hiroshima, T., Isobe, T., Koizuka, T., & Takashima, S. (2010). Photostability of YAG:Ce^{3+} nanophosphors synthesized by glycothermal method. *Journal of The Electrochemical Society*, *157*(5), J149.
42. Peter, S., Patel, A., & Kitai, A. (2019). Photoluminescence enhancement of Ce:YAG nanophosphors via doped/intrinsic core/shell structures. *Journal of Luminescence*, *211*, 82-87.

43. Chen, J., Deng, Z., Liu, Z., Lin, Y., Lan, H., Chen, D., ... & Cao, Y. (2015). Optical enhancement brought by doping Gd^{3+} ions into Ce: YAG ceramics for indoor white light-emitting diodes. *Optics express*, *23*(7), A292-A298.
44. Shi, H., Zhu, C., Huang, J., Chen, J., Chen, D., Wang, W., ... & Yuan, X. (2014). Luminescence properties of YAG: Ce, Gd phosphors synthesized under vacuum condition and their white LED performances. *Optical materials express*, *4*(4), 649-655.
45. Du, Q., Feng, S., Qin, H., Hua, H., Ding, H., Jia, L., ... & Jiang, H. (2018). Massive red-shifting of Ce^{3+} emission by Mg^{2+} and Si^{4+} doping of YAG: Ce transparent ceramic phosphors. *Journal of Materials Chemistry C*, *6*(45), 12200-12205.
46. Peter, S., Fitzpatrick, M., & Kitai, A. (2021). Glycothermal synthesis and photoluminescence of Mg–Si modified Ce: YAG nanophosphors. *Nanoscale Advances*, *3*(10), 2911-2917.
47. Shionoya, S., Yen, W. M., & Yamamoto, H. (Eds.). (2018). *Phosphor handbook*. CRC press.
48. Crystal Field Theory. (2021, June 19). https://chem.libretexts.org/@go/page/25608
49. Tanabe, Y., & Sugano, S. (1954). On the absorption spectra of complex ions II. *Journal of the Physical Society of Japan*, *9*(5), 766-779.
50. Tanabe-Sugano Diagrams. (2020, August 15). https://chem.libretexts.org/@go/page/533

51. Ling, J., Zhou, Y., Xu, W., Lin, H., Lu, S., Wang, B., & Wang, K. (2020). Red-emitting YAG: Ce, Mn transparent ceramics for warm WLEDs application. *Journal of Advanced Ceramics*, *9*(1), 45-54.
52. Shi, Y., Wang, Y., Wen, Y., Zhao, Z., Liu, B., & Yang, Z. (2012). Tunable luminescence $Y_3Al_5O_{12}$: 0.06 Ce^{3+}, xMn^{2+} phosphors with different charge compensators for warm white light emitting diodes. *Optics express*, *20*(19), 21656-21664.
53. Wang, B., Ling, J., Zhou, Y., Xu, W., Lin, H., Lu, S., ... & Hong, M. (2019). YAG: Ce^{3+}, Mn^{2+} transparent ceramics prepared by gel-casting for warm white LEDs. *Journal of Luminescence*, *213*, 421-426.
54. Dieke, G. H., & Crosswhite, H. M. (1963). The spectra of the doubly and triply ionized rare earths. *Applied optics*, *2*(7), 675-686.
55. Yang, H., & Kim, Y. S. (2008). Energy transfer-based spectral properties of Tb-, Pr-, or Sm-codoped YAG: Ce nanocrystalline phosphors. *Journal of Luminescence*, *128*(10), 1570-1576.
56. Yu, D. C., Rabouw, F. T., Boon, W. Q., Kieboom, T., Ye, S., Zhang, Q. Y., & Meijerink, A. (2014). Insights into the energy transfer mechanism in Ce^{3+}– Yb^{3+} codoped YAG phosphors. *Physical Review B*, *90*(16), 165126.
57. Li, Y., Zhou, S., Lin, H., Hou, X., & Li, W. (2010). Intense 1064 nm emission by the efficient energy transfer from Ce^{3+} to Nd^{3+} in Ce/Nd co-doped YAG transparent ceramics. *Optical Materials*, *32*(9), 1223-1226.

58. Ma, Y., Zhang, L., Zhou, T., Sun, B., Wang, Y., Kang, J., ... & Chen, H. (2020). High recorded color rendering index in single Ce,(Pr, Mn): YAG transparent ceramics for high-power white LEDs/LDs. *Journal of Materials Chemistry C*, *8*(13), 4329-4337.
59. The Franck-Condon Principle. (2020, December 2). https://chem.libretexts.org/@go/page/286996
60. Sugimoto, T. (1987). Preparation of monodispersed colloidal particles. *Advances in Colloid and Interface Science*, *28*, 65-108.
61. Nanoparticle. (2022, January 20). https://en.wikipedia.org/wiki/Nanoparticle
62. Sugimoto, T. (2007). Underlying mechanisms in size control of uniform nanoparticles. *Journal of colloid and interface science*, *309*(1), 106-118.
63. Inoue, M. (2004). Glycothermal synthesis of metal oxides. *Journal of Physics: Condensed Matter*, *16*(14), S1291.
64. Bragg's Law. (2021, December 2). https://en.wikipedia.org/wiki/Bragg%27s_law
65. Magic Angle. (2021, December 2). https://en.wikipedia.org/wiki/Magic_angle

Chapter 12: Appendix

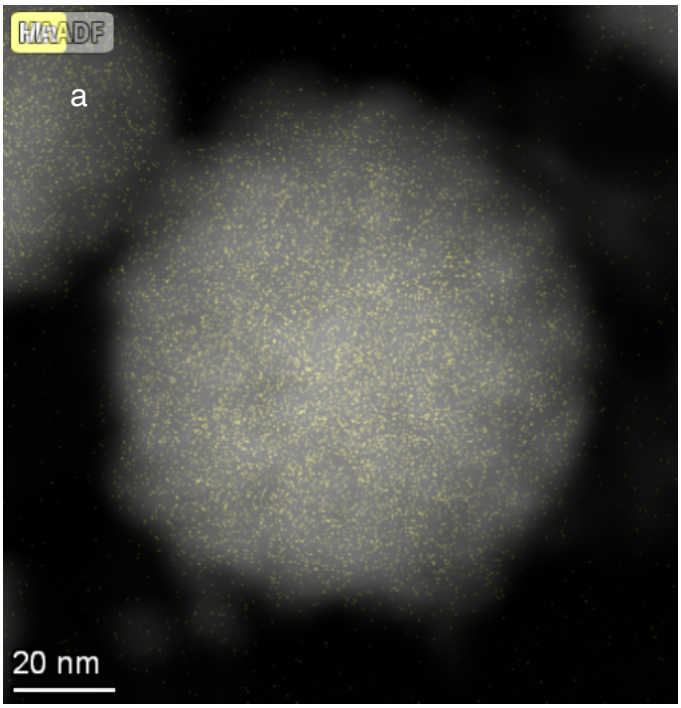

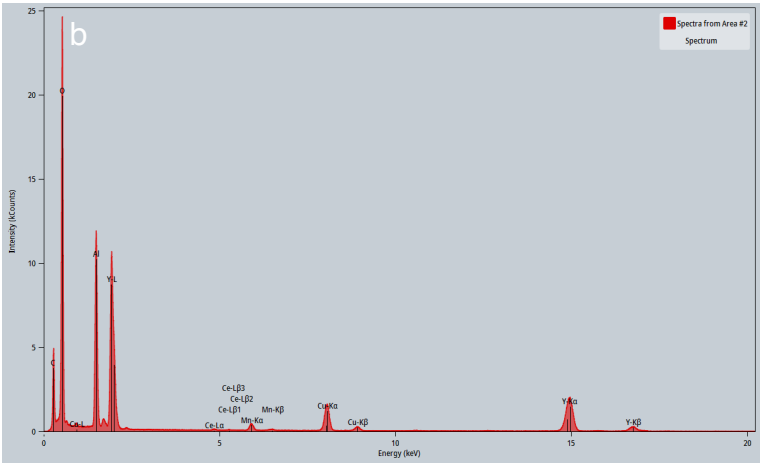

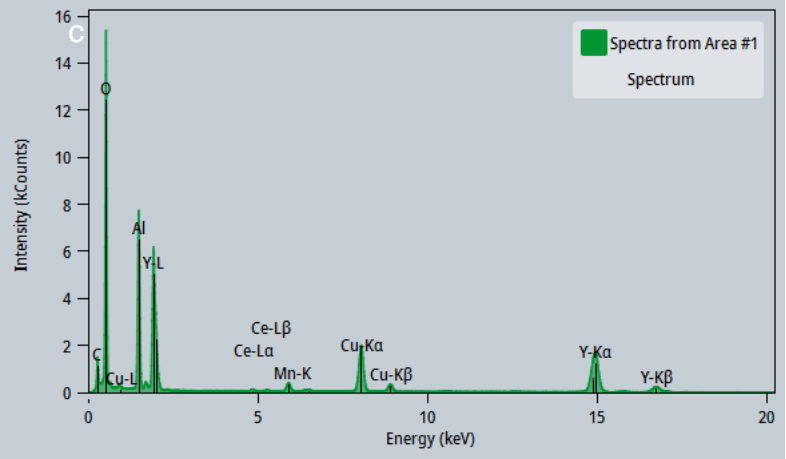

Figure 12.1:EDS chemical analysis.

a) Overlay of Mn EDS mapping with HAADF image of Mn, Si:YAG / YAG. b) EDS spectrum of Ce, 3% Mn, Si:YAG, c) EDS spectrum of Ce, 3% Mn, Si:YAG / YAG.

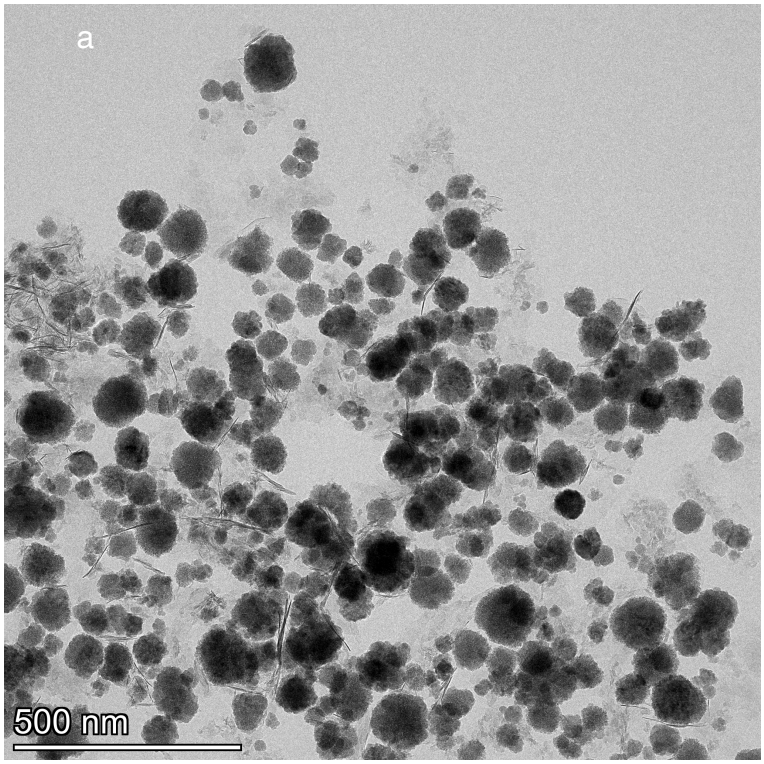

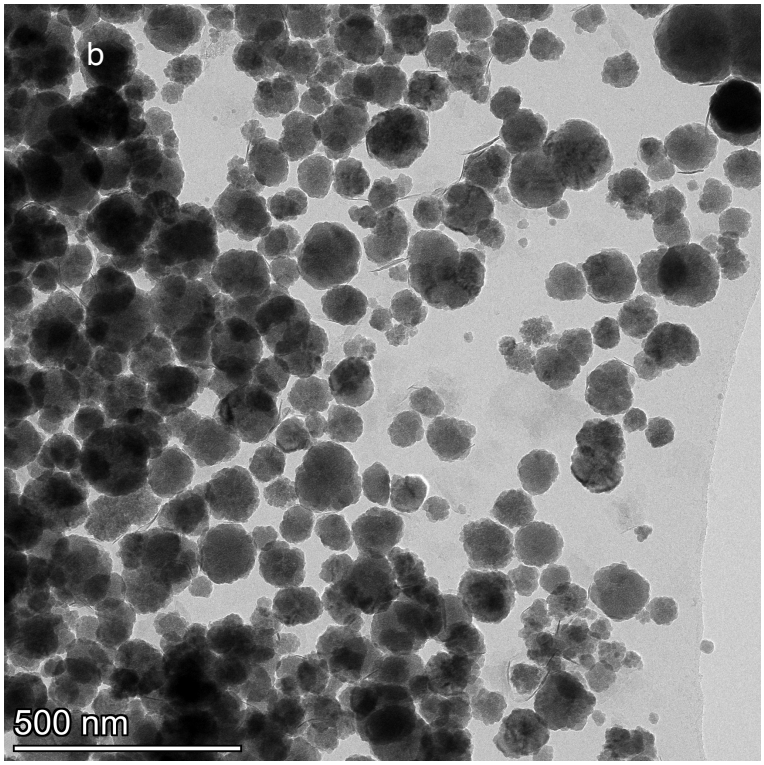
b
500 nm

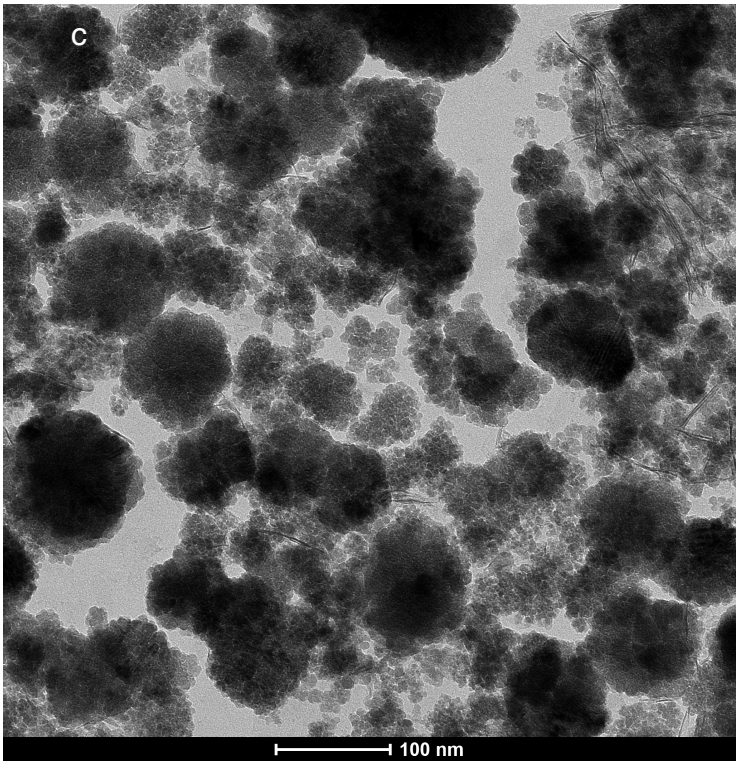

Figure 12.2: TEM images presenting particle size distribution.

a) Ce:YAG, b) Ce, 3% Mn, Si:YAG, c) Ce, 3% Mn, Si:YAG / YAG.

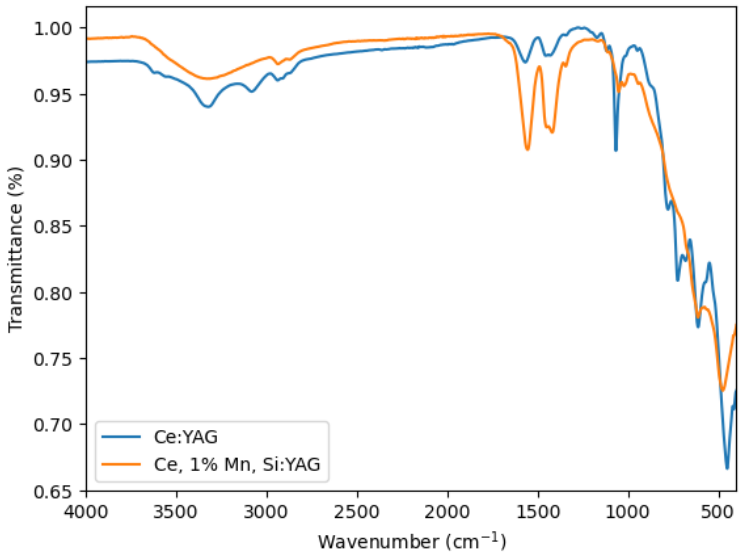

Peak position (cm^{-1})	Assignment
~3400	ν(OH)
~3100	ν_s(CH_2)
~2900	ν_{as}(CH_2)
~1600	ν_s(C=O)
~1400	ν_{as}(C=O)
~1150	δ(CH_2)

Figure 12.3: FTIR of Ce:YAG based nanophosphors.

Table indicates absorption bands of organic groups stabilizing the particle surface.

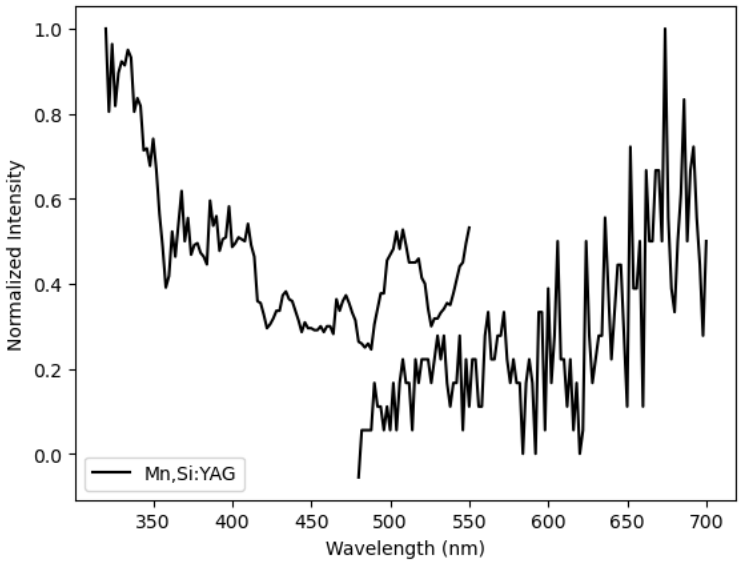

Figure 12.4: PL/PLE spectra of 3% Mn, Si:YAG. PL excitation at 400 nm. PLE monitored at 590 nm. Noise in the spectra is attributed to a low signal-to-noise ratio due to the partially forbidden transition of Mn^{2+}.